

# Measurement of the $v_2$ of $\pi^0$ Mesons Produced in $\sqrt{S_{NN}}$ 2.76 TeV PbPb Collisions at the Large Hadron Collider

By

Benjamin A Snook

Dissertation

Submitted to the Faculty of the  
Graduate School of Vanderbilt University  
in partial fulfillment of the requirements

for the degree of

DOCTOR OF PHILOSOPHY

in

Physics

May, 2014

Nashville, Tennessee

Approved:

Professor Charles F. Maguire

Professor Julia Velkovska

Professor Paul D. Sheldon

Professor Alan Tackett

Professor Thomas J. Weiler

This dissertation is dedicated to my nephew, Owen George Skoog, who was born while I was in the final stages of preparing this work. It is my hope that the light of human knowledge will guide his future for the best.

## Acknowledgements

I would like to sincerely thank my graduate advisor Dr. Charles Maguire for the guidance he has given me over the course of my graduate career. His mentorship has proven invaluable in accomplishing my work as a physicist and collaborator in the CMS experiment. I would also like to thank Dr. Julia Velkovska and Dr. Victoria Greene who have been extraordinarily helpful throughout my studies. Additionally I extend my gratitude to the other members of my thesis committee, Dr. Paul Sheldon, Dr. Alan Tackett, and Dr. Thomas Weiler for their guidance and support.

My thanks go out to my fellow colleagues in the heavy ion physics program at Vanderbilt University, Eric Appelt, Shengquan Tuo, Dr. Monika Sharma, Dillon Roach, and Dr. Ron Belmont, whose friendship and support have allowed me to persevere in times of stress and whose assistance has helped me through the course of my education and research. I would also like to thank my good friend Dr. Kieth Warnick for his companionship during the course of my studies.

Finally I would like to give my deepest appreciation to my father Randall Snook, my mother Patricia Toth, and my sister Erin Skoog, without whose love and support I would never have been able to accomplish my goals and reach this point in my studies.

# TABLE OF CONTENTS

	Page
DEDICATION . . . . .	ii
ACKNOWLEDGEMENTS . . . . .	iii
LIST OF TABLES . . . . .	vi
LIST OF FIGURES . . . . .	vii
ABBREVIATIONS AND SYMBOLS . . . . .	viii
<b>Chapter</b>	
<b>1 Introduction . . . . .</b>	<b>1</b>
<b>2 Theory and Motivation . . . . .</b>	<b>3</b>
2.1 Relativistic Heavy Ion Physics . . . . .	3
2.2 Azimuthal Anisotropy . . . . .	10
2.3 Baryon-Meson Anomaly . . . . .	14
<b>3 The CMS Detector . . . . .</b>	<b>18</b>
3.1 The Large Hadron Collider . . . . .	18
3.2 Detector Overview . . . . .	19
3.3 Electromagnetic Calorimeter (ECAL) . . . . .	25
3.4 Forward Hadron Calorimeter . . . . .	26
<b>4 Dataset and Event Selection . . . . .</b>	<b>28</b>
4.1 Minimum Bias Trigger . . . . .	28
4.2 Event Selection . . . . .	29
4.3 Centrality Determination . . . . .	29
<b>5 Analysis Methodology . . . . .</b>	<b>31</b>
5.1 $\pi^0$ Reconstruction . . . . .	31
5.2 Event Mixing Technique . . . . .	36
5.3 Yield Extraction and Efficiency Corrections . . . . .	41
5.4 Event Plane Method . . . . .	50
<b>6 Systematic Uncertainties . . . . .</b>	<b>52</b>
6.1 S4/S9 Ratio . . . . .	52
6.2 Symmetric and Asymmetric Mass Integration Window . . . . .	52
6.3 $\pi^0$ Reconstruction Efficiency . . . . .	53
6.4 Event Plane Method . . . . .	54
6.5 Other Sources of Systematic Uncertainty . . . . .	55

6.6 Total Systematic Uncertainties . . . . .	57
<b>7 Results . . . . .</b>	<b>60</b>
<b>8 Summary and Outlook . . . . .</b>	<b>67</b>
<b>Appendix</b>	
<b>A Conversion Correlations . . . . .</b>	<b>69</b>
<b>B CMS Computing . . . . .</b>	<b>75</b>
<b>BIBLIOGRAPHY . . . . .</b>	<b>77</b>

## List of Tables

Table	Page
5.1 Event-plane resolution correction values. . . . .	51
6.1 Systematic uncertainties for $v_2$ of $\pi^0$ mesons at 20 – 30% centrality. . . . .	57
6.2 Systematic uncertainties for $v_2$ of $\pi^0$ mesons at 30 – 40% centrality. . . . .	57
6.3 Systematic uncertainties for $v_2$ of $\pi^0$ mesons at 40 – 50% centrality. . . . .	58
6.4 Systematic uncertainties for $v_2$ of $\pi^0$ mesons at 50 – 60% centrality. . . . .	58
6.5 Systematic uncertainties for $v_2$ of $\pi^0$ mesons at 60 – 70% centrality. . . . .	59
6.6 Systematic uncertainties for $v_2$ of $\pi^0$ mesons at 70 – 80% centrality. . . . .	59
7.1 Final $v_2$ results for identified $\pi^0$ at 20 – 30% centrality. . . . .	60
7.2 Final $v_2$ results for identified $\pi^0$ at 30 – 40% centrality. . . . .	61
7.3 Final $v_2$ results for identified $\pi^0$ at 50 – 50% centrality. . . . .	61
7.4 Final $v_2$ results for identified $\pi^0$ at 50 – 60% centrality. . . . .	62
7.5 Final $v_2$ results for identified $\pi^0$ at 60 – 70% centrality. . . . .	62
7.6 Final $v_2$ results for identified $\pi^0$ at 70 – 80% centrality. . . . .	63

## List of Figures

Figure	Page
1.1 CMS event display. . . . .	1
2.1 QCD Phase Diagram . . . . .	4
2.2 A cartoon illustrating overlap in heavy ion collisions. . . . .	5
2.3 $v_2$ from the PHENIX experiment. . . . .	6
2.4 $R_{AA}$ from the PHENIX experiment. . . . .	7
2.5 $v_2$ from CMS and ALICE. . . . .	8
2.6 Dijet imbalance at CMS. . . . .	9
2.7 Diagram of the event plane. . . . .	11
2.8 Hydrodynamic calculation of elliptic flow. . . . .	11
2.9 Diagram of the participant plane. . . . .	13
2.10 Ratio of protons and pions from the PHENIX experiment. . . . .	14
2.11 $v_2$ of identified particles from the PHENIX experiment. . . . .	15
2.12 Quark-number scaling of $v_2$ measured by the PHENIX experiment. . . . .	16
2.13 Comparison of the $v_2$ of protons and pions from a recombination model compared with data from PHENIX . . . . .	16
2.14 A diagram illustrating hadronization by quark coalescence. . . . .	17
3.1 CMS detector overview. . . . .	18
3.2 LHC site. . . . .	19
3.3 CMS pixel detector. . . . .	20
3.4 CMS tracker geometry. . . . .	21
3.5 CMS electromagnetic calorimeter. . . . .	22
3.6 CMS hadron calorimeter geometry. . . . .	22
3.7 CMS muon detectors, transverse view. . . . .	23
3.8 CMS muon detectors, side view. . . . .	24
3.9 CMS electromagnetic calorimeter geometry. . . . .	25
3.10 One wedge of the forward hadron calorimeter. . . . .	26
4.1 Z-vertex distribution in minimum-bias PbPb events. . . . .	29
4.2 Binning of HF into centrality. . . . .	30
5.1 Diagram of $3 \times 3$ cluster. . . . .	31
5.2 Comparison of energy captured in $3 \times 3$ and $5 \times 5$ clusters. . . . .	32
5.3 Distribution of S4/S9 ratio for reconstructed photons. . . . .	33
5.4 Probability for conversion of photons in the CMS detector as a function of $\eta$ . . . . .	34
5.5 Distribution of opening angle between decay photons of reconstructed $\pi^0$ mesons. . . . .	35
5.6 Separation between photon clusters for reconstructed $\pi^0$ mesons. . . . .	35
5.7 $\pi^0$ mass peak with pair selection cuts. . . . .	37
5.8 $\pi^0$ mass peak without pair selection cuts. . . . .	38
5.9 Components same-event foreground correlation structure. . . . .	39

5.10	Comparison of $\pi^0$ mass peak in data and MC showing conversion correlation effect. . .	40
5.11	Gaussian fit to $\pi^0$ mass peak. . . . .	43
5.12	Photon matching residuals in 20 – 30% centrality. . . . .	44
5.13	Photon matching residuals in 70 – 80% centrality. . . . .	45
5.14	$\pi^0$ reconstruction efficiency as a function of $\eta$ and angle with respect to the event plane. . . . .	46
5.15	$\pi^0$ reconstruction efficiency as a function of $p_T$ . . . . .	46
5.16	$\pi^0$ reconstruction efficiency as a function of angle with respect to the event plane in 20 – 30% centrality, constant fit. . . . .	47
5.17	$\pi^0$ reconstruction efficiency as a function of angle with respect to the event plane in 20 – 30% centrality, linear fit. . . . .	47
5.18	$\pi^0$ reconstruction efficiency as a function of angle with respect to the event plane in 70 – 80% centrality, constant fit. . . . .	48
5.19	$\pi^0$ reconstruction efficiency as a function of angle with respect to the event plane in 70 – 80% centrality, linear fit. . . . .	48
5.20	Effect of efficiency corrections on measured $v_2$ in 20 – 30% centrality. . . . .	49
5.21	Cosine fit to $\pi^0$ yields to extract $v_2$ parameter. . . . .	51
6.1	$\pi^0$ mass peak with $\pm 2\sigma$ integration window. . . . .	53
6.2	$\pi^0$ mass peak with $\pm 3\sigma$ integration window. . . . .	54
6.3	$\pi^0$ mass peak with loosened pair selection cuts. . . . .	55
6.4	Effect of minimum-bias trigger efficiency on measured $v_2$ . . . . .	56
7.1	Comparison of the $v_2$ of $\pi^0$ mesons measured by CMS and PHENIX. . . . .	64
7.2	[Comparison of the $v_2$ of $\pi^0$ mesons with inclusive charged particles measured by CMS. . . . .	65
7.3	$v_2$ of identified particles measured by the ALICE experiment. . . . .	66
8.1	Preliminary $\gamma\gamma$ invariant mass spectrum with $\eta^0$ meson mass peak. . . . .	67
A.1	Pair production in CMS tracker. . . . .	69
A.2	Photon conversion diagram. . . . .	70
A.3	Background-subtraction from particle gun MC without photon conversions. . . . .	71
A.4	Background-subtraction from particle gun MC with photon conversions. . . . .	73
A.5	$v_2$ from particle gun MC without photon conversions. . . . .	74
A.6	$v_2$ from particle gun MC with photon conversions. . . . .	74

## Abbreviations and Symbols

$\eta$	Pseudorapidity
$E_T$	Transverse energy
$KE_T$	Transverse kinetic energy
$\sqrt{S_{NN}}$	Center-of-mass energy per nucleon
$p_T$	Transverse momentum
$R_{AA}$	Nuclear modification factor
$v_2$	Magnitude of the second Fourier component of the azimuthal anisotropy of particles in heavy-ion collisions.
AGS	Alternating Gradient Synchrotron
ALICE	A Large Ion Collider Experiment
ATLAS	A Toroidal LHC Apparatus
AuAu	Collisions system consisting of gold on gold
BPTX	Beam Presence Detector
BRAHMS	Broad RAnge Hadron Magnetic Spectrometers
BSC	Beam Scintillator Counter
CASTOR	Centauro And Strange Object Research
CERN	European Center for Nuclear Research
CMS	Compact Muon Solenoid
EB	Electromagnetic Calorimeter Barrel
ECAL	Electromagnetic Calorimeter
EE	Electromagnetic Calorimeter Endcap
ES	Electromagnetic Calorimeter preShower
GeV	Giga electron volt
HCAL	Hadronic Calorimeter
HF	Hadron Forward Calorimeter
HLT	High Level Trigger
HYDJET	An event generator for relativistic heavy ion collisions
IP	Interaction Point

LHC Large Hadron Collider  
LINAC LINear ACcelerator  
PbPb Collision system consisting of lead on lead  
PHENIX Pioneering High Energy Nuclear Interaction eXperiment  
pp Collisions system consisting of proton on proton  
pPb Collision system consisting of proton on lead  
PS Proton Synchrotron  
PYTHIA An event generator for high energy particle collisions  
QCD Quantum Chromo-Dynamics  
QGP Quark-gluon plasma  
RHIC Relativistic Heavy Ion Collider  
S4 Energy of the highest-energy  $2 \times 2$  cluster inside a  $3 \times 3$  cluster of ECAL crystals  
S9 Total energy of a  $3 \times 3$  cluster of ECAL crystals  
SPS Super Proton Synchrotron  
STAR A detector at RHIC, PHOBOS is not an acronym  
STAR Solenoidal Tracker at RHIC  
TeV Tera electron-volts  
ZDC Zero Degree Calorimeter

# Chapter 1

## Introduction

The field of relativistic heavy ion physics is rich and varied. There is a strong experimental background stretching from the middle of the 20<sup>th</sup> century with prolific work into the modern day. The theory that describes the interactions of the subatomic particles that make up the nucleons in the nucleus is quantum chromo-dynamics, or QCD. Due to the mathematically complex nature of QCD it has remained a difficult field to understand theoretically, so measurements from heavy-ion collisions can provide a valuable insight.

This dissertation describes the measurement of the second Fourier component  $v_2$  of the azimuthal anisotropy of neutral pions produced in lead-lead collisions at the Large Hadron Collider with a center of mass energy per nucleon  $\sqrt{s_{NN}} = 2.76$  TeV. This measurement was performed with the Compact Muon Solenoid (CMS) detector as part of the CMS collaboration. The dataset used in this analysis consisted of approximately  $3 \times 10^6$  minimum-bias lead-lead events recorded in December of 2010 by the CMS experiment. An event display from a heavy ion collision in CMS is shown in Figure 1.1.

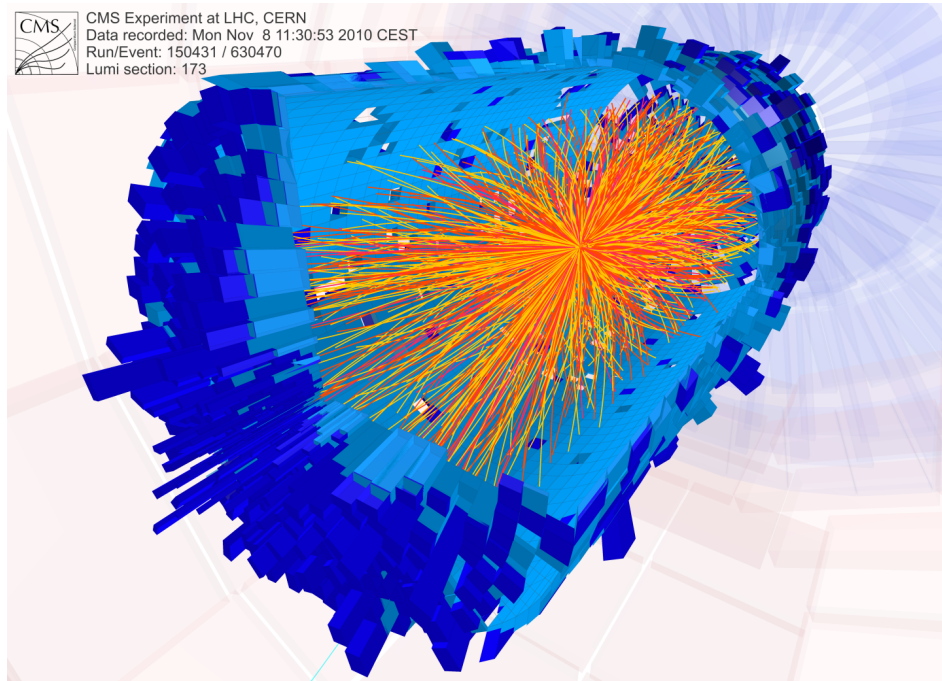


**Figure 1.1:** Event display of a heavy-ion collision recorded by the CMS detector at the LHC. The orange and yellow curved lines in the center represent charged tracks reconstructed in the silicon tracker. The blue bricks represent energy deposits from produced particles measured in the electromagnetic and hadronic calorimeters.

Chapter 2 provides a basic overview of the field of heavy ion physics. A brief history of the field is presented, with examples of measurements made by experiments at the Relativistic Heavy Ion Collider (RHIC) at Brookhaven National Labs, and more recent results from experiments at the Large Hadron Collider (LHC) at CERN. A mathematical description of azimuthal anisotropy of particles in heavy ion collisions is presented, and the sources of this anisotropy in different regimes of transverse momentum of the produced particles is discussed. A description of the anomalous abundance of baryons over mesons in the intermediate transverse momentum ( $p_T$ ) region is given along with the observation of the scaling of  $v_2$  with the number of constituent quarks in identified hadrons. An explanation of these phenomenon is discussed in the terms of a quark coalescence model.

Chapter 3 provides a detailed overview of the CMS detector and its constituent subsystems. The electromagnetic calorimeter is discussed in some detail, as is the forward hadronic calorimeter. Chapter 4 describes the dataset used for this analysis, including the triggering system used by the CMS detector to select minimum-bias events for recording. A description of the event selection cuts used in this analysis is presented. The method for determining event centrality for heavy-ion collisions in the CMS detector is described as well.

Chapter 5 provides a detailed description of the methodology of this analysis. The reconstruction of neutral pions from photon candidates identified in the electromagnetic calorimeter is described along with selection cuts on the photon candidates and the pairs. A mixed-event background subtraction technique is described for extracting the yield of produced  $\pi^0$  mesons. The effects of spurious correlations from the production of  $e^+e^-$  pairs by  $\pi^0$  decay photons on the background subtraction is discussed, along with techniques used to mitigate the effect on the final results. A study of the relative efficiency for reconstructing  $\pi^0$  mesons is presented along with a method for correcting the results for efficiency effects. A description for measuring the  $v_2$  of neutral pions by correlations with an event plane is provided along with the method used for reconstructing the event plane in the CMS experiment.

Chapter 6 presents a study of the sources of systematic uncertainty in the measurement of the  $v_2$  of neutral pions. Each source of systematic uncertainty is assessed individually, and other possible contributors to the final systematic uncertainty are discussed. Finally, chapter 7 presents the final results of this analysis. A comparison is presented with the  $v_2$  of neutral pions in gold-gold collisions measured by the PHENIX experiment at RHIC, as well as with the  $v_2$  of inclusive charged particles in lead-lead collisions at CMS. The results of the comparisons are discussed in terms of the recombination model presented in chapter 2. Appendices A and B present a detailed discussion of correlations due to photon conversions and a description of the CMS computing model, respectively.

## Chapter 2

### Theory and Motivation

Relativistic heavy ion collisions are an important experimental tool for exploring the nature of hadronic matter. In this chapter we will present a brief overview of the history of heavy ion physics, as well as some of the most important observations from past and current heavy ion experiments. We will examine the source of azimuthal anisotropy of produced particles in heavy ion collisions and a mathematical description that will allow us to measure this anisotropy. The baryon-meson anomaly will be discussed along with the significance of measurements of identified particles at intermediate transverse momentum ( $p_T$ ).

#### 2.1 Relativistic Heavy Ion Physics

The field of relativistic heavy ion physics is relatively young in comparison to many other established fields of physics. It can trace its roots back to the development of the quark model of hadronic matter, as pioneered by Gell-Man [1] and Nishijima [2], with important contributions from Ne’eman and Zweig, and experimental verification at scattering experiments at the Stanford Linear Accelerator [3]. Continuing from early scattering experiments such as the one that confirmed the existence of quarks, hadron colliders for both fixed targets and colliding beams have been a central experimental focus for probing QCD. Among these efforts were experiments with heavy ion beams and nuclear targets, from which modern heavy ion collision experiments have grown. In particular, as early as 1973 it was theorized by Chapline et al [4] that collisions between heavy ions could produce excited hot and dense states of nuclear matter.

As the nascent theory of quantum chromo-dynamics emerged, it was shown that the strong nuclear force exhibited some unique behaviors [5]. *Confinement* was the name given to describe the fact that *partons* (a general term for the quarks and gluons that compose hadronic matter) were never observed free, but always bound into hadronic states. This was explained by the magnitude of the strong coupling constant. The energy necessary to ‘pull apart’ bound quarks is enough energy to create new quarks from the vacuum, so that instead of free quarks more hadrons would be created. At high energies however it was shown that the strong coupling constant would decrease, creating a condition called *asymptotic freedom* where quarks and gluons would behave more like free particles [6]. In this asymptotic freedom regime perturbative methods can be used, but at low energies the coupling constant grows too large for perturbative calculations as the terms of the expansion diverge. This led to a situation where high energy properties were easily calculable, but low energy properties such as the mass of protons and neutrons and the interactions between nucleons in the nucleus have proved intractable. A non-perturbative method [7] known as lattice quantum chromodynamics has provided a way of calculating some low energy properties, but the huge amounts of computing power necessary and the limitations of using a lattice of points instead of a true Minkowski space have put limitations on its reach.

Through the seventies and eighties heavy ion experiments occurred at fixed-target facilities such as the Bevalac at Lawrence Berkeley National Laboratory, the Alternating Gradient Synchrotron (AGS) at Brookhaven National Laboratory, and the Super Proton Synchrotron (SPS) at CERN. The Relativistic Heavy Ion Collider at Brookhaven that came online in 2000 was the first ion collider facility. RHIC was created in order to probe even higher energies, up to a center of mass energy per nucleon ( $\sqrt{S_{NN}}$ ) of 200 GeV. The goal of the RHIC collider was to create a state of matter known as the quark gluon plasma [8], where quarks and gluons would be freed from hadronic bound states as the strong force is screened by the numerous color charges in the system. This screening is analogous to electromagnetic plasmas created where high temperatures strip the electrons from nuclei and interact freely.

Figure 2.1 shows a diagram of the phases of QCD matter, that is matter composed of quarks and gluons. Normal nuclear matter corresponds to a low temperature and a moderate baryon chemical potential. As we increase the baryon chemical potential we encounter other exotic types of matter, such as neutron matter and degenerate quark matter that is thought to exist in neutron stars, and is of great interest to astrophysics. The area that we can probe with relativistic heavy ion collisions goes in the opposite direction, towards higher temperatures and decreasing baryon chemical potential. The baryon chemical potential decreases because the initial state baryon number becomes a small contribution to the end state due to the enormous number of produced particles which contribute zero net baryon number, aside from any small CP-violating terms arising from weak interactions.

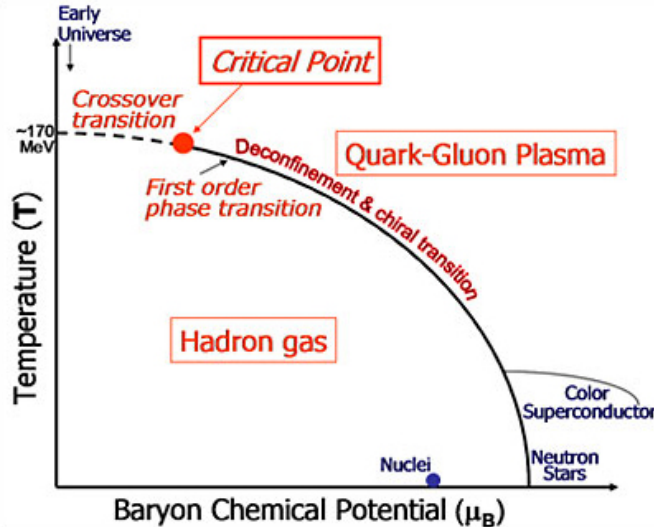


**Figure 2.1:** A map of the theorized QCD phase space [9], with baryon chemical potential on the x-axis and temperature on the y-axis. Heavy ion collisions at colliders like RHIC and the LHC probe the high temperature, low baryon chemical potential region of the phase space, where the transition between hadrons and the quark-gluon plasma is predicted.

As the temperature increases, there is strong evidence that a phase transition occurs between a hadron gas and the true quark-gluon plasma (QGP) phase [10]. The nature of this transition as either first or second order can be calculated, but the calculation depends strongly on factors such as the number of light quark flavors and the masses of these quarks. In particular the mass of the

strange quark can affect the particular details of the phase space.

A first order phase transition is one which involves a latent heat, such as the transition between water and ice. In this kind of phase transition additional energy added to the system will not increase the temperature, but instead form a mixed state with regions of both phases coexisting at different ratios depending on the input of energy. More energy in the system converts the lower-energy phase into the higher-energy phase, until only the high-energy phase exists and the transition has been completed. A second order phase transition is also known as a continuous phase transition, and in these transitions there is a more seamless blend between the two phases. They are characterized by a divergent correlation length in the system, leading to large fluctuations in the thermodynamic properties of the material near a critical point.

Calculations from lattice QCD indicate that the phase transition is a first order transition [11], with a second order critical point in the phase diagram as the baryon chemical potential approaches zero, beyond which is a crossover transition. The exact position of this critical point is not well known, and one of the primary goals of the beam energy scan program of experiments at RHIC is to attempt to determine this crossover location.

One of the most important characterizing variables of heavy ion collisions is the centrality of the event. In heavy ion collisions, due to the finite size of the nucleus, every inelastic hadronic collision will have some varying degree of overlap between the two nuclei [12]. Nucleons within the two nuclei that lie in the overlap region and participate in the interaction are known as the participants, and nucleons outside of this region are known as spectators. Figure 2.2 shows a cartoon illustrating the finite overlap of colliding nuclei. It is impossible to directly measure the impact parameter between the two nuclei however, so we must measure other variables to characterize the overlap of the two colliding nuclei. Considering only collisions that result in hadronic interactions between the two nuclei, we can characterize events with a variable that will change as a function of the degree of overlap. We can then divide the measured distribution into proportional bins of the nuclear hadronic cross-section. These bins define the centrality of an event. Section 4.3 discusses the centrality definition used by the CMS experiment. It is in the most central events with the highest energy density where we expect the quark-gluon plasma to form, while peripheral events are not expected to show characteristics of the formation of this medium.

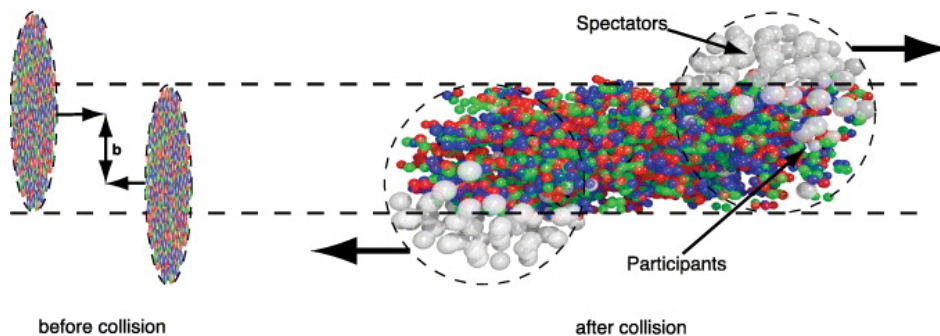


**Figure 2.2:** A cartoon illustrating the overlap in heavy ion collisions that gives rise to event centrality. The impact parameter  $b$  is the distance between the center of the two colliding nuclei. The colored particles indicate the participating nucleons in the interaction, known as participants, and the grey particles indicate the non-participating spectator nucleons.

Early predictions from lattice QCD were that the medium of the quark-gluon plasma would only be weakly interacting [13]. However experimental observations at the PHENIX [14], STAR [15], PHOBOS [16], and BRAHMS [17] experiments provided compelling evidence that the QCD medium produced in collisions at RHIC energies is in fact very strongly coupled. One of the most powerful observations was the measurement of collective flow in the medium at low transverse momentum ( $p_T$ ) [18]. Figure 2.3 shows an example of the second Fourier component  $v_2$  of the azimuthal anisotropy of unidentified charged hadrons as measured by the PHENIX experiment [19]. For a detailed discussion of the Fourier decomposition of azimuthal anisotropy, see section 2.2. In a weakly interacting system it would not be expected to see strong collective flow results, as there would not be the strong interactions that allow the particles produced in the expanding medium to thermalize. However experiments at RHIC observed that heavy ion collisions at this energy produced very strong collective flow, behaving as a nearly perfect liquid with a shear viscosity over entropy density approaching the quantum mechanical lower limit of  $\hbar/4\pi k_B$  [20].

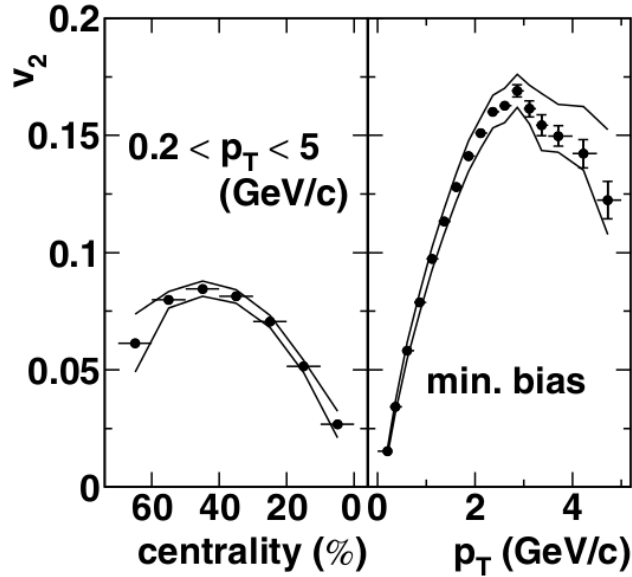


**Figure 2.3:** Unidentified charged hadron  $v_2$  versus centrality and  $p_T$  at  $\sqrt{S_{NN}} = 200$  GeV as measured by the PHENIX experiment [19]. See section 2.2 for a detailed definition of the  $v_2$  parameter.

Another indicator of the strongly-interacting medium was evidence of a strong energy loss mechanism as high  $p_T$  partons traverse the medium [21]. One of the most prominent signals is the nuclear modification factor  $R_{AA}$  of produced particles [22], as defined in equation 2.1:

$$R_{AA}(p_T) = \frac{(1/N_{AA}) d^2 N_{AA} / dp_T dy}{(\langle N_{coll} \rangle / \sigma_{pp}^{inel}) d^2 \sigma_{pp} / dp_T dy} \quad (2.1)$$

Here  $N_{AA}$  is the particle multiplicity in a heavy ion collision,  $\langle N_{binary} \rangle / \sigma_{pp}^{inel}$  is scaled number of binary collisions for a given event,  $\sigma_{pp}$  is the particle production in proton-proton collisions, and  $p_T$  and  $y$  are the transverse momentum and rapidity of the particle, respectively.

$R_{AA}$  essentially quantifies how many particles are produced in a  $p_T$  region compared to the number produced in the same  $p_T$  region from an equivalent number of nucleon-nucleon collisions in a heavy ion collision. However this accounts not only for modification due to the presence of hot nuclear matter, but also the effects of the initial state cold nuclear material. This makes it necessary to also examine the effect of cold nuclear matter independently. At RHIC, this is done by colliding deuterons with gold atoms, which does not create the energy density necessary for quark-gluon plasma to form [23]. It has been observed in these collisions that there is an enhancement at low  $p_T$  [24]. This effect is known as Cronin enhancement, and it arises due to multiple hard scatters smearing the momentum spectrum from higher to lower  $p_T$ . Starting in January of 2013, the LHC collided protons with lead nuclei at a center of mass energy per nucleon  $\sqrt{S_{NN}} = 5.02$  TeV. There have been some tantalizing pieces of evidence that in this collision system and energy regime there may be effects of the formation of a quark-gluon plasma phase [25–27], but discussion of these results are beyond the scope of this dissertation.

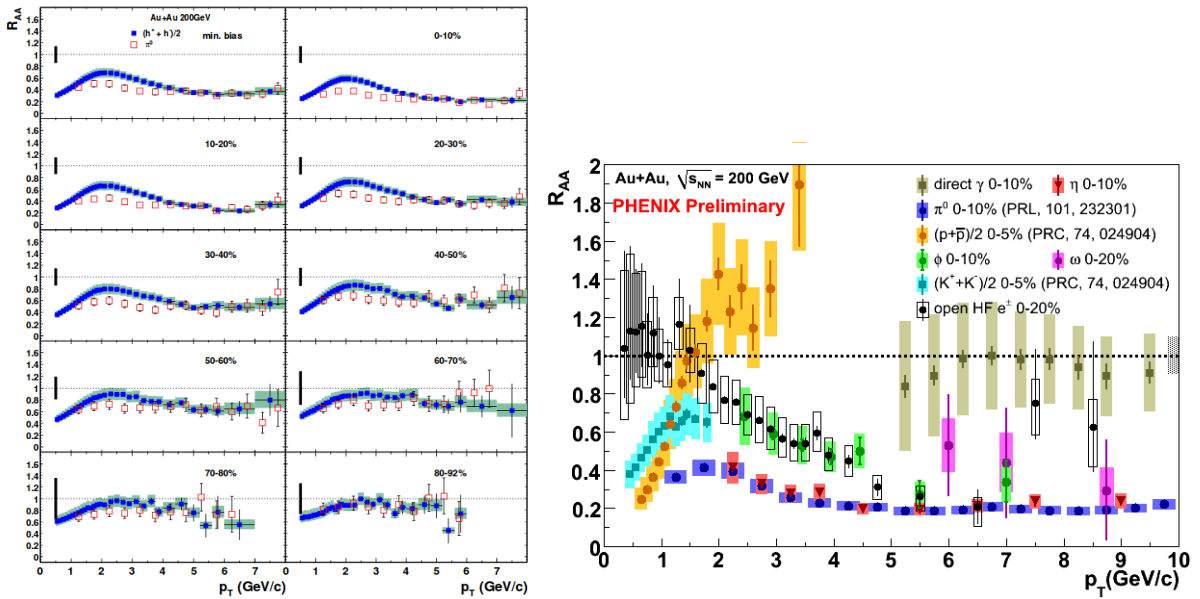


**Figure 2.4:** Left: The  $R_{AA}$  for unidentified charged hadrons and identified  $\pi^0$  mesons as a function of  $p_T$  at  $\sqrt{S_{NN}} = 200$  GeV for several centrality bins, showing the rise in  $R_{AA}$  from central to peripheral events [14]. Right: The  $R_{AA}$  for different particle species as measured at the PHENIX experiment at RHIC.

In the analysis of high  $p_T$   $\pi^0$  mesons, the PHENIX experiment observed that a prominent suppression occurs for produced hadrons in central events [28]. It was also shown that this effect disappears for more peripheral events, indicating that only the more central events produce that hot and dense medium resulting in this energy loss, as seen in the left plot of Figure 2.4. Furthermore, direct photon measurements determined that their  $R_{AA}$  has a value of 1, as shown in the right plot of Figure 2.4. Since photons interact electromagnetically instead of through the QCD force, this strongly indicates the energy loss is a QCD effect. One remarkable finding was the  $R_{AA}$  of identified baryons at intermediate  $p_T$  rose above unity [29]. This and other effects became known as the baryon-meson anomaly, which will be discussed further in section 2.3.

Beginning in November of 2010, the LHC collided beams of  $^{208}_{82}\text{Pb}$  ions at an energy of  $\sqrt{s_{NN}} = 2.76$  TeV, more than an order of magnitude higher in energy than the data analyzed by the RHIC experiments. Data were collected by the ALICE, CMS, and ATLAS experiments. ALICE was designed specifically as a heavy ion experiment, while CMS and ATLAS were designed as general-purpose particle detectors that have proven to be very well equipped for heavy-ion measurements in addition to pp measurements. In particular, both CMS and ATLAS are capable of making direct measurements of high  $p_T$  jets and other hard probes of the hot and dense medium, as well as providing excellent tracking with full azimuthal coverage and high pseudorapidity range.

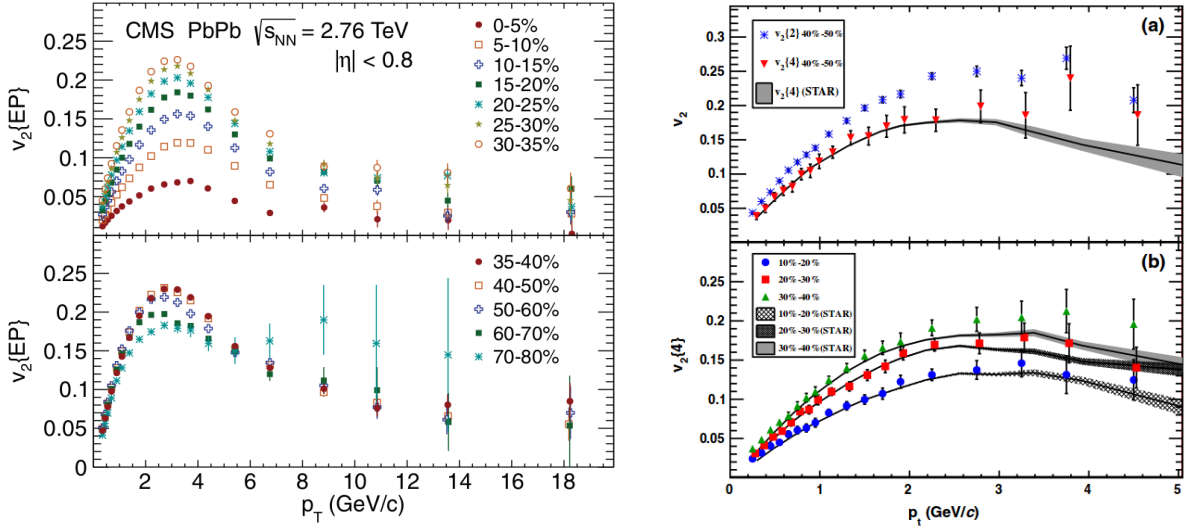


**Figure 2.5:** Left: The  $v_2$  of unidentified hadrons using the event plane as measured by the CMS experiment in lead-lead at  $\sqrt{s_{NN}} = 2.76$  TeV [30]. Right: The  $v_2$  of unidentified hadrons using second and fourth order cumulants as measured by the ALICE experiment, compared with results from the STAR experiment at  $\sqrt{s_{NN}} = 200$  GeV [31].

The first measurements of the azimuthal anisotropy of inclusive charged particles at the LHC were observed to be similar in magnitude to that observed at RHIC energies [30–32], as seen in Figure 2.5. In addition to the flow results, ATLAS [33] and CMS [34] have both observed a marked imbalance in dijet samples produced in heavy ion collisions, in addition to ‘monojet’ events where the away-side jet seems to have been completely swallowed by the medium. An example of an imbalanced dijet event observed in the CMS detector is illustrated in Figure 2.6.

It had been unknown whether the strong coupling observed at RHIC would continue at LHC energies [35], or whether a weakly coupled quark gluon plasma as was predicted earlier would manifest. The measurements of azimuthal anisotropy, jet suppression, and  $R_{AA}$  by experiments at the LHC provide good evidence that the medium created at these energies is still strongly coupled. The measurements presented in this dissertation will provide further understanding of the evolution of the medium at these energies.

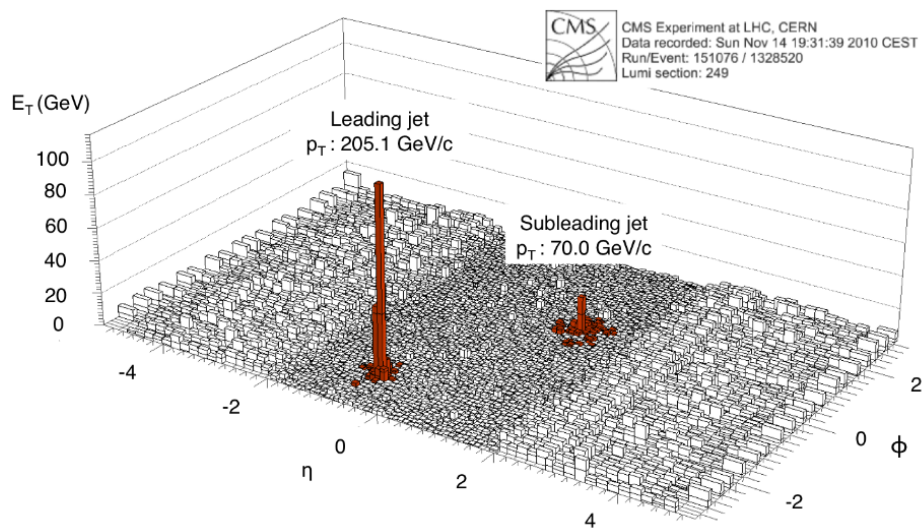


**Figure 2.6:** An event display from the CMS experiment showing the direct measurement of reconstructed dijets and the prominent momentum imbalance in a central heavy ion collision at  $\sqrt{s_{NN}} = 2.76$  TeV. [34]

## 2.2 Azimuthal Anisotropy

In heavy ion collisions, one of the most prominent experimental signatures is the azimuthal anisotropy of produced particles. This anisotropy can have multiple sources, and the dominant source is dependent on the momentum range of the particles being measured. In any momentum range though the anisotropy can be characterized by a Fourier decomposition of the particle multiplicity [36].

$$\frac{d^3 N}{d^3 p} = \frac{1}{2\pi} \frac{d^2 N}{p_T dp_T dy} \left( 1 + \sum_{n=1}^{\infty} 2v_n \cos [n (\phi - \Psi_r)] \right) \quad (2.2)$$

In equation 2.2, the azimuthal component of the particle multiplicity has been expanded in Fourier components, with a normalization factor of  $\frac{1}{2\pi}$ . The variable  $\Psi_r$  is the angle made between the reaction plane of the event and the x-z plane of the detector (though the coordinate system chosen is arbitrary). The reaction plane itself is defined by the plane formed by the vector pointing along the beam line and the vector connecting the centers of the two colliding nuclei. Figure 2.7 shows a diagram of two overlapping nuclei and the corresponding reaction plane of the event, which is oriented at the angle  $\Psi_r$  with respect to the CMS coordinate system. If we examine the azimuthal component independently, we have the result presented in equation 2.3:

$$\frac{dN}{d\phi} = \frac{1}{2\pi} \left( 1 + \sum_{n=1}^{\infty} 2v_n \cos [n (\phi - \Psi_r)] \right) \quad (2.3)$$

The  $v_n$  components characterize the magnitude of the anisotropy of a given order. This is analogous to the multipole expansion used to characterize radiation fields in electromagnetism and other physical phenomena with a potentially asymmetric distribution.

In a relativistic heavy ion collision, the impacting nuclei create an excited region known as the fireball. This region acts as the hot and dense medium through which particles created by hard scatterings traverse [21]. This medium itself though is also subject to forces from the high temperature and pressure created by the collision [37]. The degree of asymmetry created by the overlap of the two nuclei is the primary driver of the mechanisms which lead to an azimuthal anisotropy in the resulting event. In very central collisions where the nuclei are nearly overlapping there is little geometric asymmetry, which leads to a small measured anisotropy. This asymmetry grows as centrality decreases, until eventually in very peripheral collisions the energy density in the collision region is too low to form the strongly-coupled medium and the asymmetry of the overlap region no longer drives the characteristics of the event.

The independent components  $v_n$  of the azimuthal anisotropy can be studied individually, and together contribute to an understanding of the event characteristics. At low  $p_T$ , below  $1 - 2$  GeV/c, the dominant source of azimuthal anisotropy is the hydrodynamic flow of the hot and dense medium produced in heavy-ion collisions [38]. The first component is the by-definition symmetric  $v_0$  term, known as radial flow, which is the outward expansion of the medium from the collision point. The  $v_1$  component is known as directed flow, caused by the transparency of the colliding nuclei as particles pass through each other. This quantity is zero at mid-rapidity by symmetry of the identical collid-

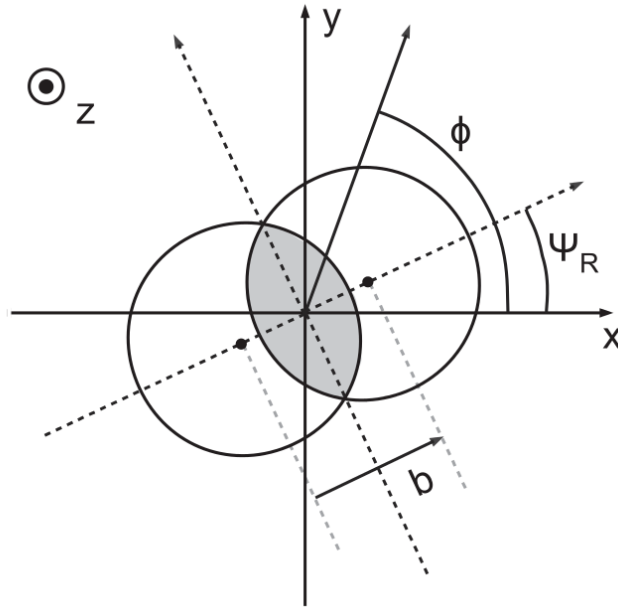


**Figure 2.7:** A diagram of two colliding heavy nuclei emphasizing the ellipsoidal excited region created by mid-central collisions and defining the reaction plane of the collision [30].

ing ions. One of the most important examples of collective behavior is elliptic flow, characterized by the Fourier component  $v_2$  [39]. Pressure gradients in the almond-shaped overlap region create a momentum-space anisotropy in the medium, which gives rise to a position-space anisotropy of produced particles at a particular  $p_T$  that can be measured in the detector. Figure 2.8 shows a calculation of the pressure gradients within the overlap region and the expansion of the medium from relativistic hydrodynamics. Higher order components such as  $v_3$  and  $v_4$  arise from initial-state fluctuations in the distribution of nucleons within the overlap region, and contain information about the equation of state of the medium.

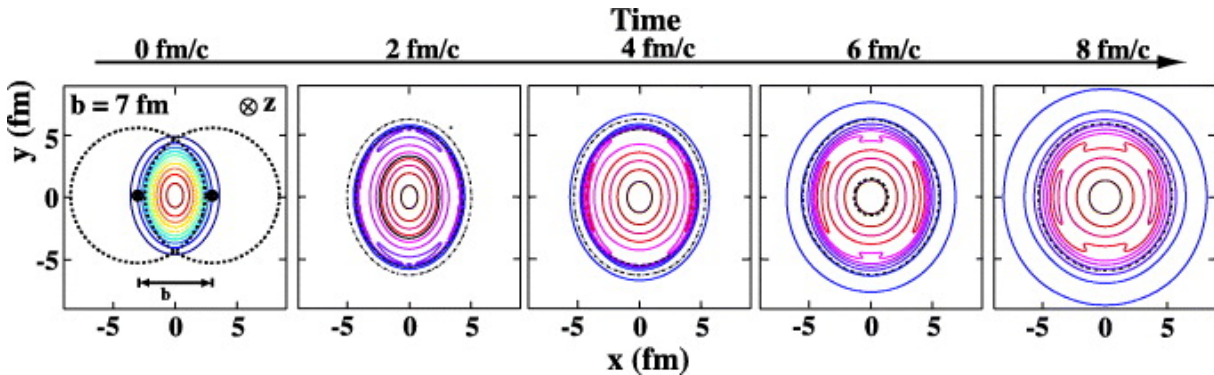


**Figure 2.8:** A calculation from a hydrodynamic model showing collective flow in a mid-central heavy ion collision as a function of time [37].

For low  $p_T$  particles, if we make several assumptions we can describe the behavior of the particles in the medium with a relativistic hydrodynamic model [40, 41]. The necessary assumptions for the

validity of this model are that the mean free path of partons travelling through the medium is much smaller than the characteristic size of the medium, that the particles are in a local thermal equilibrium, and that the temperature and pressure vary slowly with respect to the evolution of the medium.

Relativistic hydrodynamics begins essentially with basic thermodynamic principles, and it is described by the standard thermodynamic variables such as the energy density. We can start by defining the energy-momentum tensor for a relativistic fluid, given in equation 2.4:

$$T^{\mu\nu} = (\epsilon + P)u^\mu u^\nu - P g^{\mu\nu} \quad (2.4)$$

Ultimately the laws of relativistic hydrodynamics are a set of conservation laws among the various currents of the system [42]. The most general form for a medium like the quark-gluon plasma is given in equations 2.5 and 2.6:

$$\partial_\mu (n u^\mu) = 0 \quad (2.5)$$

$$\partial_\mu T^{\mu\nu} = 0 \quad (2.6)$$

Equation 2.5 gives the conservation of baryon number, while equation 2.6 in turn provides conservation of energy and momentum. These equations are not complete, and additional terms will depend on the number of conserved quantities. Other prominent examples of conserved currents are net charge and strangeness [43]. What then distinguishes the quark-gluon plasma is the equation of state of the medium, which gives the relationship between thermodynamic variables such as the pressure, volume, and temperature. This equation must be derived from the known mechanics of the medium. The starting point for a fluid like the QGP, where many particles will be created and destroyed in quantum interactions is the grand canonical ensemble. There has been a great deal of work with lattice QCD attempting to calculate the QGP equation of state [44, 45].

For high  $p_T$  particles, above 5 – 6 GeV/c, hydrodynamics is no longer the appropriate model for particle production so the  $v_n$  components must arise from other effects. In addition to bulk processes, hard scatterings in the initial collision will also produce partons with a very high momentum that do not thermalize with the medium [21]. These high momentum partons however will still pass through the medium and interact with the particles composing it. The primary mechanism through which this energy loss occurs is gluon brehmstrahlung [46, 47] by partons travelling through the quark-gluon plasma, with smaller corrections due to collisions with other particles in the medium. At high  $p_T$  the  $v_2$  component in particular contains information about the path-length dependence on energy loss in the medium [48]. In this region the primary mode of particle production is fragmentation of jets, and high  $p_T$  partons that give rise to jets will lose more or less energy depending on whether they travel along the long or short axis of the almond-shaped overlap region.

At intermediate  $p_T$ , 2 – 5 GeV/c, the issue is not as clear cut. Hydrodynamics is not entirely applicable in this region, but there will be some overlap from the higher end of the thermal spectrum so there is such a contribution. There will additionally be some contribution from the fragmentation

of jets, which also carries some information about energy loss in the medium. At intermediate  $p_T$  these effects are not easy to disentangle and both will have some contribution to the measured  $v_2$ . Additionally at intermediate  $p_T$  we observe a difference between the  $v_2$  of baryons and mesons [49]. This is part of the phenomenon called the baryon-meson anomaly, which will be discussed further in section 2.3.

One important distinction to realize is that between the reaction plane defined by the position of the two colliding nuclei and the event plane that is experimentally measured in the detector. The reaction plane itself is not an observable quantity, and is correlated with the event plane by the shape of the overlap region. However initial-state fluctuations in the nuclear distribution function of the overlapping nuclei can play a large role in determining the particle distribution of the final event [22]. Figure 2.9 shows a diagram of a Glauber [50] Monte Carlo simulation of two overlapping nuclei. Fluctuations in the initial state give rise to an irregularly shaped overlap region.

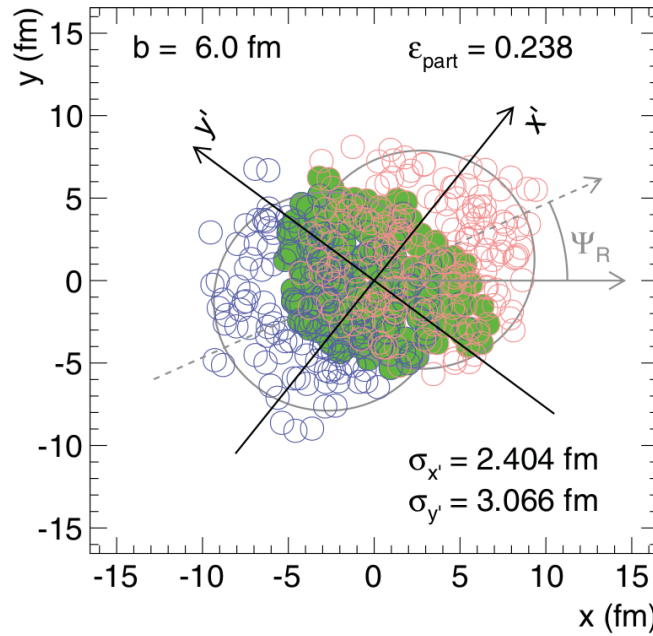


**Figure 2.9:** A diagram showing the definition of the second-order participant plane from the distribution of participants in a heavy ion collision from Glauber MC [30]. The two large overlapping circles are the profiles of the two colliding nuclei, and the smaller circles are the individual nucleons with red and blue corresponding to either nucleus. The green shaded circles are participating nucleons, and the open circles are spectator nucleons.

The eccentricity of the participants in the overlap region defines a participant plane  $\Psi_{PP}$  which will fluctuate around the true reaction plane event by event. This participant plane is defined differently for every order of  $v_n$ , but for this analysis will be considering only the second-order participant plane corresponding to  $v_2$ . The participant plane itself is also not a direct observable, but when we determine an event plane from the detector information it will be correlated with this participant plane. The method for correcting for these fluctuations will be discussed in section 5.4

## 2.3 Baryon-Meson Anomaly

Experiments at RHIC observed a phenomenon with identified particles that hadn't been predicted. Several different measurements such as particle ratios [29, 51, 52], nuclear modification factor, and anisotropic flow [49, 53, 54] all showed an unexpected difference between baryons and mesons in the intermediate  $p_T$  region. Ratios of the  $p_T$  spectra of baryons to mesons showed an increase in the yield of baryons at intermediate  $p_T$ . Similarly measurements of  $R_{AA}$  and  $R_{CP}$  (analogous to  $R_{AA}$  comparing central and peripheral nucleus-nucleus collisions) showed an enhancement of baryon production at intermediate  $p_T$ . Figure 2.10 shows an example of the ratio of protons and pions illustrating this enhancement. Measurements of the  $v_2$  of identified hadrons showed an increase of the  $v_2$  of baryons over that of mesons at intermediate  $p_T$ . These phenomena have been collectively referred to as the baryon-meson anomaly.

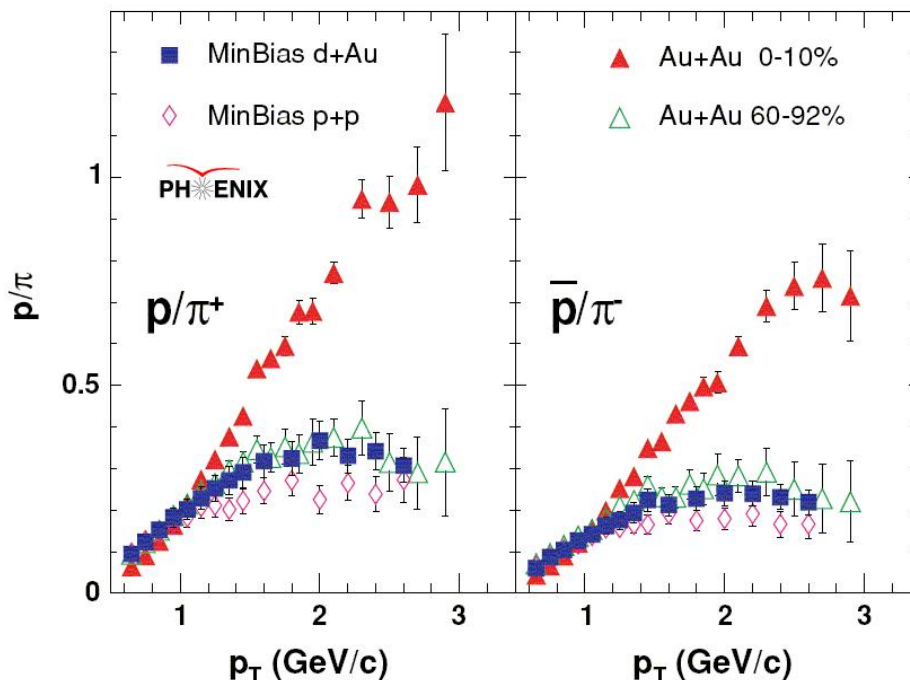


**Figure 2.10:** Ratios of identified protons/pions (left) and antiprotons/pions (right) for peripheral and central gold-gold (AuAu) collisions, deuteron-gold (dAu) collisions, and proton-proton (pp) collisions, as measured by the PHENIX experiment. [55]

Hydrodynamic models [41, 43] predicting particle abundances were seen to match the measured  $v_2$  and particle yields at low  $p_T$ , but these models were unsuccessful at predicting the intermediate  $p_T$  results. Similarly fragmentation mechanisms [56] that successfully predicted the particle suppression at high  $p_T$  did not explain the baryon-meson anomaly. A vital clue to the anomaly was the observation that when these quantities were scaled by the number of constituent quarks, the anomalous difference disappeared and particles followed the same trends [49, 53, 54]. An example of this scaling in identified particle  $v_2$  is shown in Figure 2.12.

Quark number scaling of azimuthal anisotropy in particular provided a very strong indication of

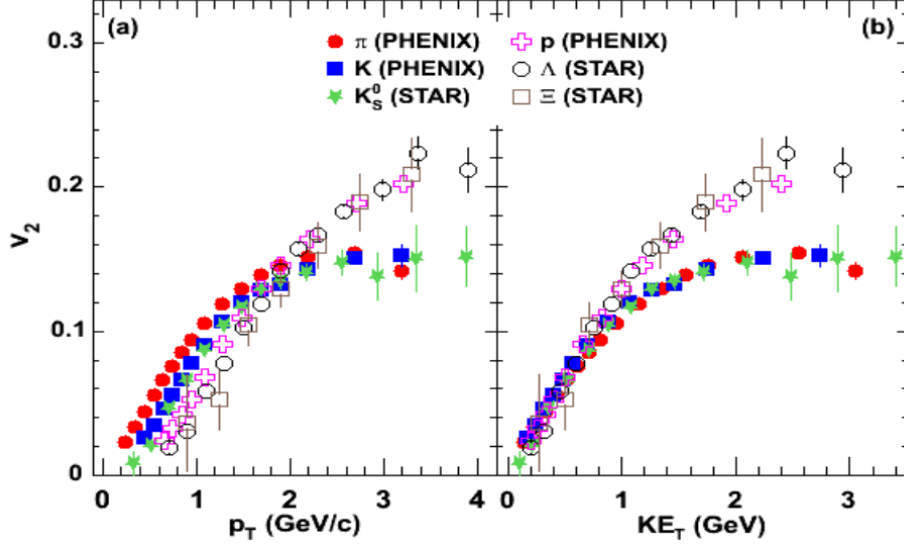


**Figure 2.11:** The  $v_2$  of identified particles as a function of  $p_T$  (left) and transverse kinetic energy  $KE_T$  (right), measured by the PHENIX experiment. [54]

deconfinement in the hot and dense medium produced at RHIC energies. The scaling of  $v_2$  with the number of constituent quarks indicates that the relevant degrees of freedom that give rise to this anisotropy are the individual quarks and gluons, not the final state hadrons [57]. In order to explain how this lead to the enhancement of baryons in the final state, a model of quark coalescence was developed for hadronization at intermediate  $p_T$  [58]. This recombination model [59, 60] was successful in predicting the enhancement of baryons at intermediate  $p_T$  as well as the observed quark number scaling of azimuthal anisotropy [61]. A comparison of theoretical predictions from a recombination model with data from PHENIX is shown in figure 2.13.

Figure 2.14 shows a cartoon of how recombination of low  $p_T$  partons can give rise to hadrons at intermediate  $p_T$ , as well as illustrating the competing mechanism of fragmentation in this momentum region. Hydrodynamics predicts that the partons in the expanding quark-gluon plasma will have a common flow velocity. Quarks that are close together in phase space will preferentially combine into hadrons as the medium transitions from a soup of quarks and gluons into a hadron gas. Depending on how many quarks the final state hadrons contain (ie 3 for baryons, 2 for mesons) then we expect to see an enhancement for hadrons with a larger number of quarks as they will all contribute momentum to the final state. This effect becomes visible at intermediate  $p_T$  where the enhancement dominates. At higher  $p_T$  quark coalescence ceases to be a contributing mechanism to hadronization and fragmentation of high  $p_T$  partons will dominate, and the baryon-meson anomaly disappears.

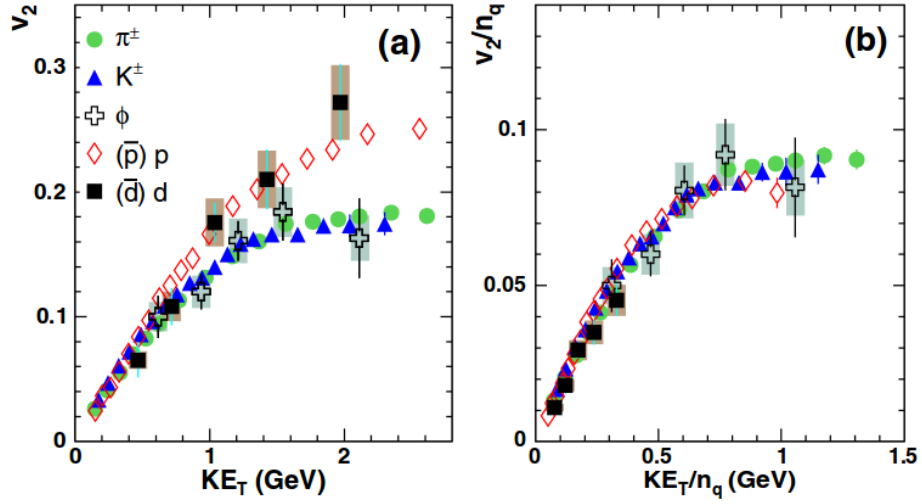


**Figure 2.12:** Left: The  $v_2$  of several identified particles as a function of transverse kinetic energy ( $KE_T$ ), measured by the PHENIX experiment. Right: The  $v_2$  as a function  $KE_T$  for several identified particles, scaled by the number of constituent quarks. [53]

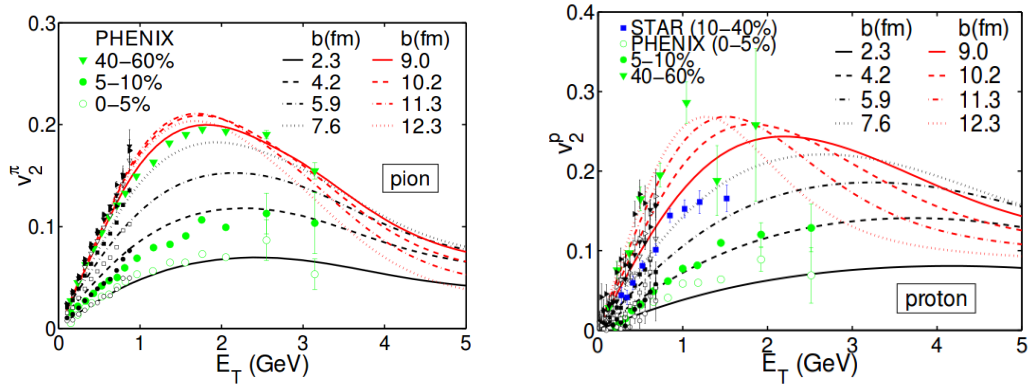


**Figure 2.13:** A comparison of the  $v_2$  calculated from a recombination model for pions (left) and protons (right) as a function of  $E_T$  at several different impact parameters, compared with data from the PHENIX and STAR experiments. [61]

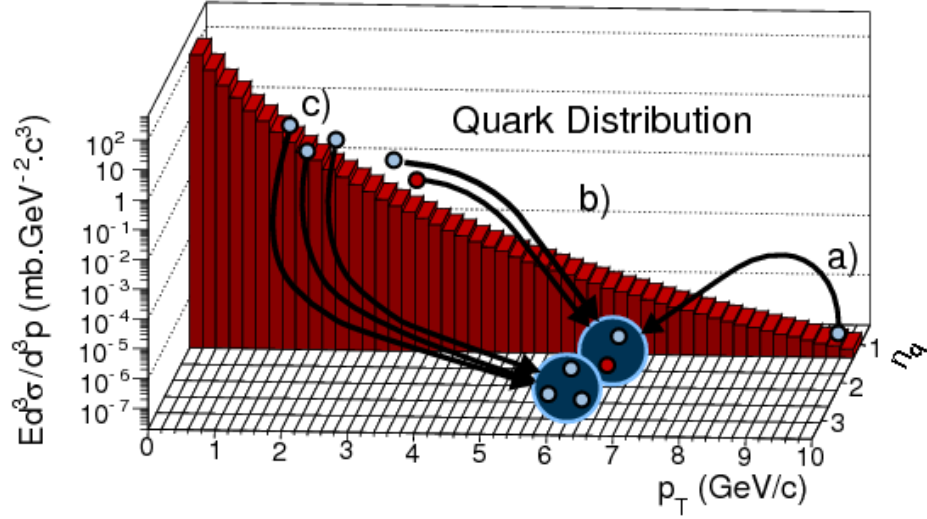


**Figure 2.14:** A diagram illustrating hadronization by quark coalescence [35]. Low  $p_T$  quarks can combine to form a hadron with a higher collective  $p_T$ . An example of fragmentation from a high  $p_T$  parton into a hadron at intermediate  $p_T$  is also shown for comparison of the competing effects at intermediate  $p_T$ .

The measurement of identified neutral pions in lead-lead collisions at a center-of-mass energy per nucleon  $\sqrt{S_{NN}} = 2.76$  TeV allows us to explore this quark number scaling in the higher energy regime produced at the LHC. Previous measurements of the azimuthal anisotropy of  $\pi^0$  mesons by the PHENIX experiment [62] have been highly valuable for understanding the behavior of produced mesons at intermediate  $p_T$ . By comparing the  $v_2$  of identified neutral pions at LHC energies with other particle types and collision systems we will be able to provide an insight into the evolution of the strongly-interacting medium at higher energies.

## Chapter 3

### The CMS Detector

The Compact Muon Solenoid [63, 64] (see Figure 3.1) is a highly segmented detector with full azimuthal coverage and a large coverage in pseudorapidity, allowing the detector to capture a wealth of data from particle collision events. The detector resides at interaction point 5 (IP5) along the LHC tunnel, where information is collected from proton-proton (pp), lead-lead (PbPb), and proton-lead (pPb) collisions. The CMS detector's excellent tracking and calorimetry capabilities make it an ideal detector for many different types of measurements. These include high- $p_T$  measurements such as dijet asymmetry in heavy-ion collisions and searches for Higgs-like particles in pp collisions, and lower- $p_T$  measurements such as two-particle correlations and the anisotropy of  $\pi^0$  mesons.

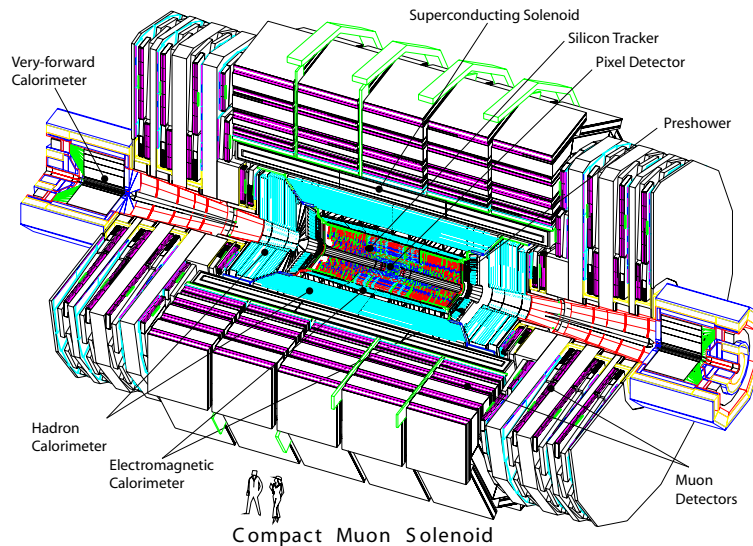


**Figure 3.1:** A cutaway view of the CMS detector, showing the location and geometry of the tracker, calorimetry system, and muon system.

In this chapter we will provide a general overview of the LHC accelerator and the CMS detector itself. A detailed description of the electromagnetic calorimeter and forward hadron calorimeter in particular as the most important subsystems used for this measurement will also be described in more detail.

### 3.1 The Large Hadron Collider

The Large Hadron Collider [65] at CERN is currently the most powerful particle accelerator in the world, located on the border of Switzerland and France near the city of Geneva. Figure 3.2 shows an overhead view of the LHC site and the position of the experiments. It is housed in a circular tunnel

27 kilometers in circumference, buried underground at a depth ranging from 50 to 175 meters. The accelerator is made up of 1,232 dipole bending magnets, 392 quadrupole focusing magnets, and a series of radio-frequency cavities to accelerate and maintain the beam.



**Figure 3.2:** An aerial view of the LHC site, with a graphical overlay showing the location of the ring and the underground experiment sites.

The beams into the LHC are produced by a sequence of prior accelerators that bring the beams to their input energy. For protons, the beam starts at the LINAC 2 linear accelerator, which feeds into the Proton Synchrotron (PS) Booster, whereas ions start from the LINAC 3, which injects into the Low-Energy Ion Ring. Both of these systems inject into the Proton Synchrotron, which in turn feeds into the Super Proton Synchrotron, which provides the final boost before injection into the LHC ring itself.

The machine typically runs pp collisions for eight months of the year, with an additional month dedicated to ion running before shutting down for the winter. During the initial 2010 pp run the LHC ran at 3.5 TeV for each beam, with a center of mass energy  $\sqrt{S} = 7$  TeV. For the 2010 lead ion run, the machine ran at  $\sqrt{S_{NN}} = 2.76$  TeV. Starting in February 2013, the LHC entered Long Shutdown 1 for ring and detector upgrades, after which the machine will reach full design energy of  $\sqrt{S} = 14$  TeV for pp and  $\sqrt{S_{NN}} = 5.5$  TeV for PbPb.

### 3.2 Detector Overview

The CMS coordinate system defines its origin at the geometric center of the detector. The X axis is taken to point towards the center of the LHC ring and the Y direction is taken to be upwards, with Z pointing along the counter-clockwise direction along the beampipe for a conventional right-handed coordinate system.

The core of the CMS detector is a superconducting solenoidal magnet capable of generating a 4 Tesla magnetic field, though in order to prolong the lifetime of the machine the magnet is run at 3.8 T. The inner radius of the magnet is 5.9 m and it has a length of 12.9 m. This powerful magnetic field is necessary in order to provide sufficient momentum resolution for tracking particles with  $p_T$  in the TeV range, especially in the muon system in order to distinguish the sign of high-momentum muons.

Inside the magnet are the hadron and electron calorimeters, the silicon strip tracking system, and the inner pixel detector around the collision point. Outside of the magnet radius is the outer hadron calorimeter and the muon system. The forward region also contains the forward hadron calorimeter, the Zero Degree Calorimeters (ZDC), and the Beam Scintillator Counters (BSC). There is also a very forward calorimetry system, CASTOR, but this system was not used for the 2010 heavy ion running.

The pixel detector is made up of a central barrel section and two endcaps, sharing the same pseudorapidity coverage as the silicon strip tracker. A schematic of the pixel detector is shown in Figure 3.3. The pixel detector barrel is constructed from 3 layers of silicon pixels, each pixel measuring  $100 \times 150 \mu\text{m}^2$ , with radii of 4.4, 7.3, and 10.2 cm. The pixel endcaps are constructed from 2 disks on each side with an inner radius of 6 cm and an outer radius of 15 cm. In total there are 66 million individual pixels, with position resolution of approximately  $10 \mu\text{m}^2$  in the  $\delta r, \phi$  plane and  $20 \mu\text{m}$  in the  $z$ -direction.

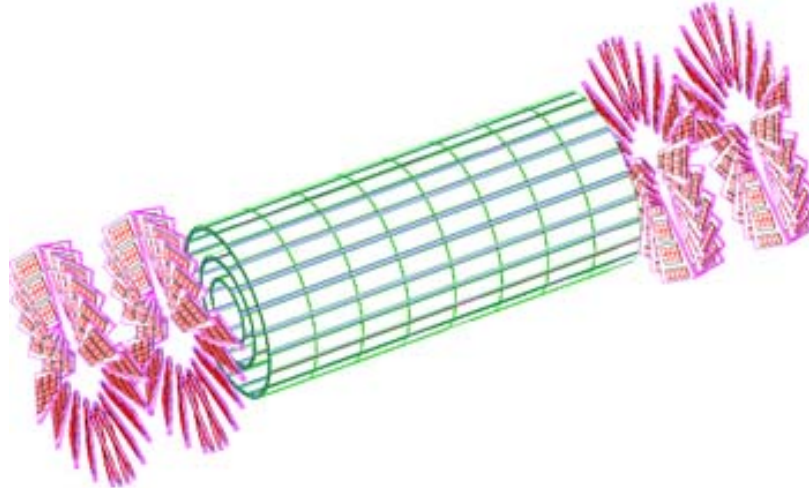


**Figure 3.3:** The CMS pixel detector, showing the geometry of the barrel and endcap layers.

The silicon strip tracker barrel has two distinct sections, the Tracker Inner Barrel (TIB) and Tracker Outer Barrel (TOB). Figure 3.4 shows a schematic of the tracker system. The TIB has 4 layers of silicon strips, each strip measuring  $320 \mu\text{m}^2$  in thickness, with a minimum cell size of  $10 \text{ cm} \times 80 \mu\text{m}^2$ , with a spatial resolution of  $2334 \mu\text{m}^2$  in the  $\delta r, \phi$  plane and  $230 \mu\text{m}^2$  in  $z$ . The TOB has 6 layers of silicon strips measuring  $500 \mu\text{m}^2$  thick with a minimum cell size of  $25 \text{ cm} \times 180 \mu\text{m}^2$ , and a spatial resolution of  $35\text{-}52 \mu\text{m}^2$  in the  $\delta r, \phi$  plane and  $530 \mu\text{m}$  in  $z$ .

There are two endcap systems for the silicon strip tracker, a set of Tracker Inner Discs (TID) and

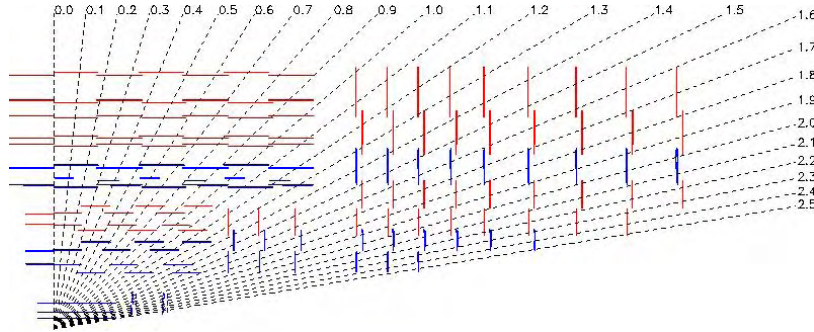


**Figure 3.4:** A side view of the CMS Silicon Strip Tracker, showing the position and geometry of the inner and outer barrel and endcap tracking layers.

the Tracker Endcaps (TEC). The TIDs sit outside of the TIB and inside of the TOB, and are made of 3 discs on each side with silicon chips measuring  $320 \mu\text{m}^2$ . The TEC comprises 5 additional discs on each side beginning at the outer end of the TOB. The first three discs have silicon chips  $320 \mu\text{m}^2$  thick, and the outermost two discs have chips measuring  $500 \mu\text{m}^2$  thick. With the addition of the endcap systems, the entire silicon tracking system has a pseudorapidity acceptance of  $|\eta| < 2.5$ .

In this analysis the tracking system is not used directly for photon reconstruction, but it is indirectly used for providing the collision vertex for each event and certain tracker related variables are used as event selection criteria as discussed in section 4.2.

The electromagnetic calorimeter (ECAL) surrounds the silicon tracker and has two distinct sections, the barrel and the endcaps. A schematic of the ECAL is shown in Figure 3.5. Both the barrel and endcap use lead tungstate ( $\text{PbWO}_4$ ) scintillator crystals. The barrel has an inner radius of 1.29 meters and covers a pseudorapidity range of  $|\eta| < 1.479$ , and the endcaps sit at a distance of 314 cm from the center of the detector, and cover the pseudorapidity range  $1.479 < |\eta| < 3.0$ . The endcaps also have a preshower system in order to help distinguish minimally-ionizing events from charged hadrons from electromagnetic showers. A fully detailed description of the ECAL systems will be given in the next section.

In this analysis the ECAL barrel is the primary detector subsystem, used to measure and identify the daughter photons from decaying  $\pi^0$  mesons.

The hadronic calorimeter (HCAL) surrounds the ECAL sits inside the solenoid magnet, except for a small Hadron Outer (HO) detector surrounding the magnet. Figure 3.6 shows a schematic of the HCAL. The inner HCAL consists of a barrel section and two endcap sections, similar to the ECAL. These components are constructed from towers of interleaved layers of brass absorber plate and plastic scintillator tiles, with embedded wavelength-shifting fibers. There are 32 rings of 72 towers each, 2304 towers total in the HCAL barrel, giving it a segmentation of  $\Delta\eta \times \Delta\phi = 0.087 \times 0.087$ . The pseudorapidity coverage of the HCAL barrel is  $|\eta| < 1.4$ . The endcaps consist of similar towers arranged in an  $\delta r, \phi$  grid separated into wedges, with a pseudorapidity range of  $1.3 < |\eta| < 3.0$ . The HO wraps around the magnet, located inside the muon system, having a pseudorapidity range of  $|\eta| < 1.26$ . This results in an effective thickness for the HCAL of 10 interaction lengths, improving the energy resolution and the performance for measuring missing transverse energy in an event.

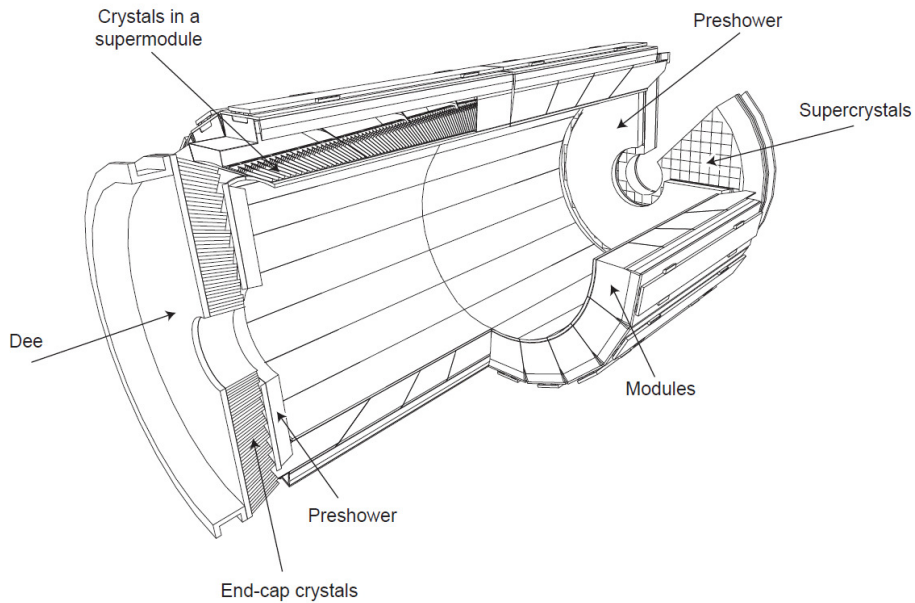


**Figure 3.5:** A schematic of the CMS electromagnetic calorimeter, showing the arrangement of crystals in the barrel and endcap sections.

The Hadron Forward (HF) calorimeter is located 11.2 m from the center of the detector, with two identical units on either side. The towers are constructed of steel absorber plate and quartz fiber scintillaors, arranged into 18 wedges in  $\phi$ , with a full pseudorapidity coverage of the HF detector is  $3 < |\eta| < 5$ . A detailed description of the HF detector is given in a later section.

The muon system consists of a central barrel section surrounding the magnet and two endcaps on either side of the detector. Figure 3.7 shows an end-on view of the CMS detector, showing the layout of the barrel muon system. The muon barrel is made of four layers of Drift Tube (DT) sensors and Resistive Plate Chambers (RPC) interleaved with the iron return yoke for the magnet. The two innermost layers consist of one DT unit with RPCs overlaid on the inner and outer surface, the outer two layers have one DT and one RPC overlaid on the inner surface only. The barrel section

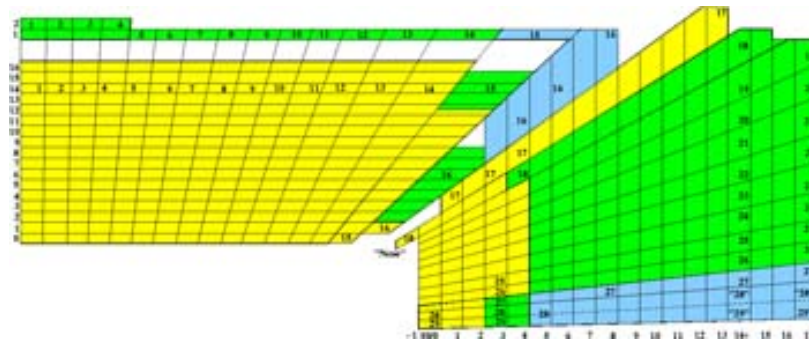


**Figure 3.6:** A side view of the CMS Hadron Calorimeter, showing the geometry of the barrel and endcap systems. Not visible is the Hadron Forward detector.

is segmented in 5 rings along the z axis to match the segmentation of the return yoke, and has a pseudorapidity coverage  $|\eta| < 1.2$ . Each of the 5 rings is divided into 12 sections on the 3 innermost layers, and 14 sections in the outermost layer, staggered in order that a high- $p_T$  muon will always be intercepted by at least 3 of the 4 layers.

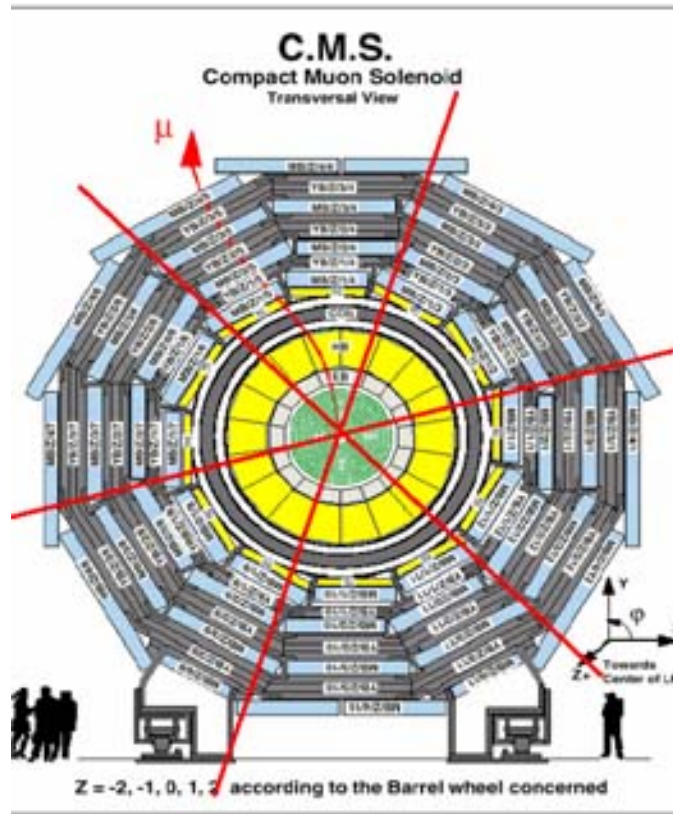


**Figure 3.7:** A transverse view of the CMS detector, showing the rings of the barrel section of the muon detection system, as well as the calorimetry and tracking systems.

The muon endcaps consist of 4 discs of Cathode Strip Chambers (CSC) and RPCs interleaved with the endcap portions of the iron return yoke, and each disc separated into rings in the radial direction. Figure 3.8 shows a side-view schematic of the muon system, detailing the layout of the endcaps. There are 3 rings for the innermost disc and 2 for the others, with each ring consisting of 18 sections in  $\phi$  for the innermost ring in each disc, the outer (1 or 2) discs having 36 sections in  $\phi$ . The outermost (1 or 2) rings in each disc have a CSC chamber with an RPC overlaid on the inner surface, while the innermost rings in each disc contain only the CSC chambers. The endcaps extend the pseudorapidity coverage of the muon system to  $|\eta| < 1.6$  with the RPCs, and  $|\eta| < 2.4$  with the CSCs.

The muon system was not used for this analysis, but the description is included for completeness.

The ZDC and BSC are very forward subdetectors in the CMS detector, particularly useful for heavy

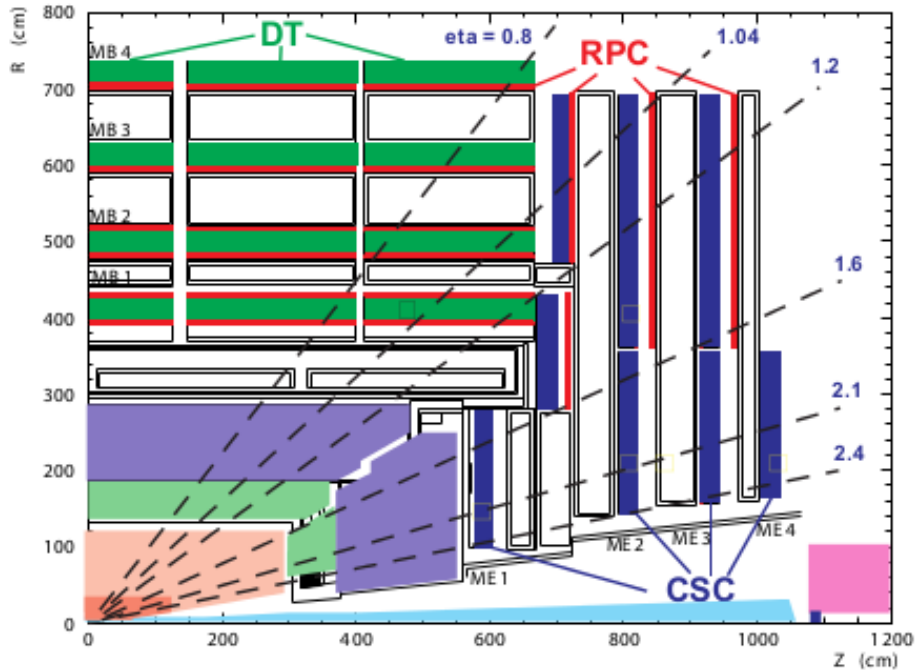


**Figure 3.8:** A side view of CMS muon system, showing the layers of the barrel and endcap systems and the coverage of the individual sensor subsystems.

ion studies and in the case of the Beam Scintillator Counters, for event triggering. The ZDC has both an electromagnetic and hadronic calorimeter component composed of tungsten absorber and quartz fiber scintillator, and covers the pseudorapidity region  $8.4 < |\eta|$ , located on either side of the interaction point (IP). The BSCs are plastic scintillator tiles that overlap partially with the HF calorimeter, covering a pseudorapidity range of  $3.9 < |\eta| < 4.4$ , with an inner disc separated into 8 sections and 4 larger tiles beyond the inner disc to provide further coverage.

### 3.3 Electromagnetic Calorimeter (ECAL)

The CMS Electromagnetic Calorimeter is a hermetic  $4\pi$  detector, covering  $360^\circ$  in azimuth and a pseudorapidity range of  $|\eta| < 3.0$  in total. Figure 3.9 shows a side-view rendition of the ECAL barrel and endcap with the pseudorapidity coverage of each. With such coverage accompanied by high energy resolution, it is an extremely capable detector for measurement of the  $\pi^0 \rightarrow \gamma\gamma$  decay channel. The calorimeter is made of a central barrel and two endcaps, utilizing lead tungstate scintillator crystals for detection of electromagnetic showers, as well as preshower silicon tracking layer incorporated into the endcap systems.

The ECAL Barrel (EB) has an internal radius of 1.29 m from the IP to the front face of the crystals, and covers a pseudorapidity range of  $|\eta| < 1.49$ . The crystals are arranged into 36 supermodules, each covering one half of the barrel longitudinally to meet in the middle, and  $20^\circ$  of  $\phi$ . Each supermodule holds an array of  $20 \times 85$  crystals, in the  $\phi$  and  $z$  directions respectively, giving the EB a segmentation of 360 crystals in the  $\phi$  direction and 170 end-to-end along the  $z$  axis. Each crystal is tilted in a quasi-projective geometry towards the IP, with a deviation of no more than  $3^\circ$  in any direction between a vector from the IP to the front face of the crystal and the long axis of the crystal.

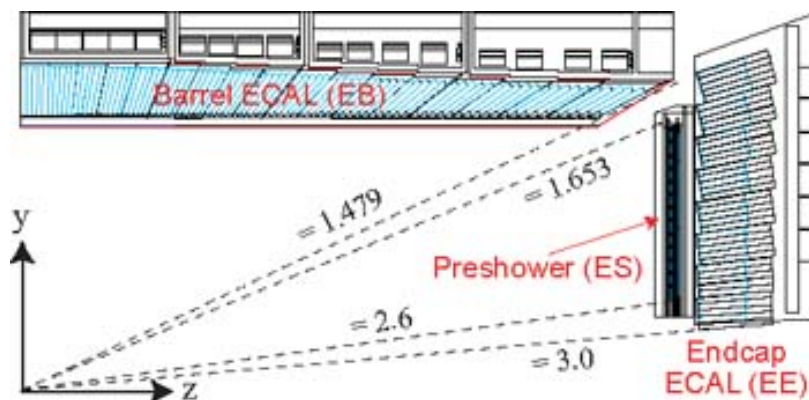


**Figure 3.9:** A side view of the ECAL barrel and endcaps, showing the crystal orientation with respect to the vertex.

Each of the ECAL Endcaps (EE) are situated on either side of the barrel covering a pseudorapidity range of  $1.49 < |\eta| < 3.0$ , and the front face of the subdetector systems are 3144 mm from the IP in the  $z$  direction. The endcap crystals are housed in supercrystals (SC), with 276 full SCs of  $5 \times 5$  crystals each and an additional 36 partial SCs on the periphery, arranged in an  $x$ - $y$  grid covering the annular area of the endcap. The crystals are focused at a point along the  $z$  direction 1300 mm behind the IP, the angular offset varying as a function of  $\eta$ .

In front of the EE crystals is a preshower detector (ES), covering the pseudorapidity range  $1.653 < |\eta| < 2.6$ . The ES is composed of 2 layers of lead absorber plate in front of silicon strip detectors, which measure the energy of showers initiated in the lead plate. This system provides improved discrimination between electrons and minimally-ionizing particles in the endcap, as well as providing improved position resolution for electrons and photons in the endcaps.

The scintillator crystals in the ECAL are made of lead tungstate ( $\text{PbWO}_4$ ), with a Molière radius of 2.2 cm and a radiation length  $\chi_0$  of 0.89 cm, allowing for a compact detector with high granularity. The scintillation decay time is approximately 25 ns, which matches the bunch crossing rate of the LHC at design luminosity. The crystals in the EB are square frustums measuring  $22 \times 22$  mm on the front face and  $26 \times 26$  mm<sup>2</sup> on the rear, with a length of 230 mm, or  $25.8 \chi_0$ , allowing for a vast majority of the deposited energy to be captured in the crystal. The crystals in the EE are square frustums measuring  $28.62 \times 28.62$  mm on the front face and  $30 \times 30$  mm<sup>2</sup> on the rear, with a length of 220 mm, or  $24.7 \chi_0$ . Radiation damage to the crystals is tracked and corrected for by using a laser monitoring system to check the transparency of the crystals and adjust the calibration to account for any losses.

### 3.4 Forward Hadron Calorimeter

The forward hadron calorimeter (HF) is one of the forward subdetectors of the CMS experiment, covering a pseudorapidity range of  $3 < |\eta| < 5$ , measuring energy deposited by high rapidity particles emitted from the IP. It is separated into 18 wedges in  $\phi$ , each with 13 layers in  $\eta$ . A diagram of one wedge of the HF detector is shown in Figure 3.10. The two innermost layers have a single tower apiece while the remaining layers all have two towers side-by-side along the  $\phi$  direction, for a total of 24 towers per wedge, and 432 towers in total on each side. The towers are laid out in a non-projective geometry, with a segmentation of  $\Delta\eta \approx 0.1$  for the innermost layer,  $\Delta\eta \approx 0.175$  for the next 11 layers, and  $\Delta\eta \approx 0.3$  for the outermost layer, and  $10^\circ$  in  $\phi$  for all but the outermost layer which is  $20^\circ$ .

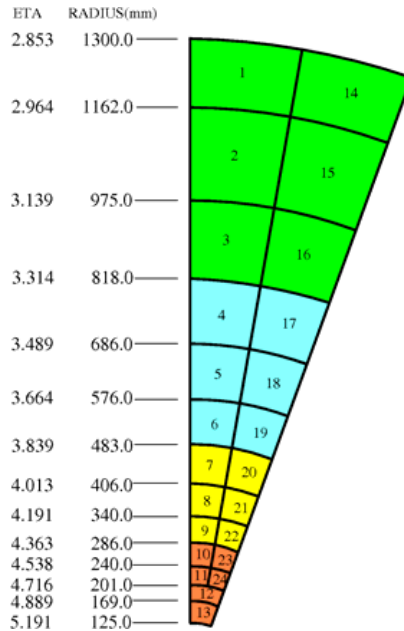


**Figure 3.10:** An illustration of one wedge of the HF detector, showing the segmentation of the individual towers.

The HF towers are constructed of steel absorber blocks with quartz fiber scintillator embedded in

the steel, with the fibers running parallel to the beam axis along the length of the steel blocks. There are two lengths of fibers tuned to detecting different shower topologies, the long fibers running the full 165 cm length of the blocks for detecting the electromagnetic portion, and shorter fibers running 143 cm from the back of the blocks to measure the hadronic portion.

## Chapter 4

### Dataset and Event Selection

The dataset for this analysis is composed of  $24 \times 10^6$  minimum-bias PbPb collisions at a center of mass energy of 2.76 TeV  $\sqrt{S_{NN}}$  collected by the CMS experiment during the November 2010 heavy ion running at the LHC. These events are taken from data-quality approved runs 150887 to 152957, from a full dataset containing approximately  $30 \times 10^6$  minimum-bias events. The data were reconstructed with CMS analysis software version 3\_9\_9\_patch1 [64].

#### 4.1 Minimum Bias Trigger

With the high luminosity supplied by the LHC machine, the CMS experiment requires a powerful triggering system [64] to distinguish interesting events for recording to tape. This process starts with the Level-1 trigger system, a system of custom hardware processors that are fed by the detector electronics. The L1 trigger is based on the presence of “trigger primitive” objects such as electrons, photons, muons, jets. Some event characterizing variables based on a lower-resolution readout of the muon systems and calorimeters are also included. Based on the presence of these trigger objects and coincidence signals between them, the L1 trigger will pass interesting events for further processing in a High Level Trigger (HLT) farm. This farm will perform more sophisticated processing including a partial reconstruction of the event in full resolution in the region of interest for the relevant trigger. The HLT uses a fully software-based trigger defined by the physics groups in order to read out and record the most promising events for analysis.

The minimum-bias trigger used in CMS for the 2010 heavy ion data taking is highly efficient and robust, capturing  $97 \pm 3\%$  of the total inelastic hadronic cross chapter for PbPb at 2.76 TeV. The trigger was required to be very effective at removing noise and non-collision events as well as ultra-peripheral collisions due to a number of constraints imposed by the running conditions during 2010. The pixel detector required a hold-off time ranging from 100 – 300 microseconds after the acceptance of L1 trigger events in order to read out the signals in Virgin Raw mode. Additionally, a total rate limitation of 150 Hz for the physics stream at the HLT was necessitated by bandwidth limitations due to operating the silicon strip tracker in Virgin Raw mode during the 2010 run and the need to fit within disk storage constraints for the final dataset.

To provide the necessary high efficiency and low fake rate, a HLT path comprised of a logical OR of two triggers was devised, a BSC coincidence trigger and an HF coincidence trigger respectively. The BSC coincidence trigger requires at least one segment of the BSC detectors on either side of the interaction point to register a hit. The HF coincidence trigger requires at least one tower to register at least 3 GeV of deposited energy in the HF systems on both sides of the interaction point. These triggers are also gated by a beam presence detector (BPTX) L1 trigger bit requiring two colliding ion bunches present in the detector. The combination of these triggers provides a fake rate less than 1 Hz at full beam intensity.

## 4.2 Event Selection

For this analysis, additional event selection cuts were applied on top of the standard minimum bias trigger, following a standard event selection procedure derived by the CMS Heavy Ion group for the 2010 dataset [66]. A coincidence filter requiring three HF calo towers above threshold on either side was applied, as well as the requirement of at least one primary vertex within a range of  $|z| < 15$  cm. The  $z$ -vertex distribution in minimum-bias PbPb events is shown in Figure 4.1. A cut on the cluster shape in the pixel detector was applied requiring a compatibility with the primary vertex to filter out beam-gas and beam scraping events originating outside of the collision region. A beam-halo rejection cut based on the BSC L1 trigger was also applied. Finally and specifically for this analysis a cut was applied rejecting all events between 0 – 20% centrality, which had too much combinatorial background for a singles  $\pi^0$  measurement.

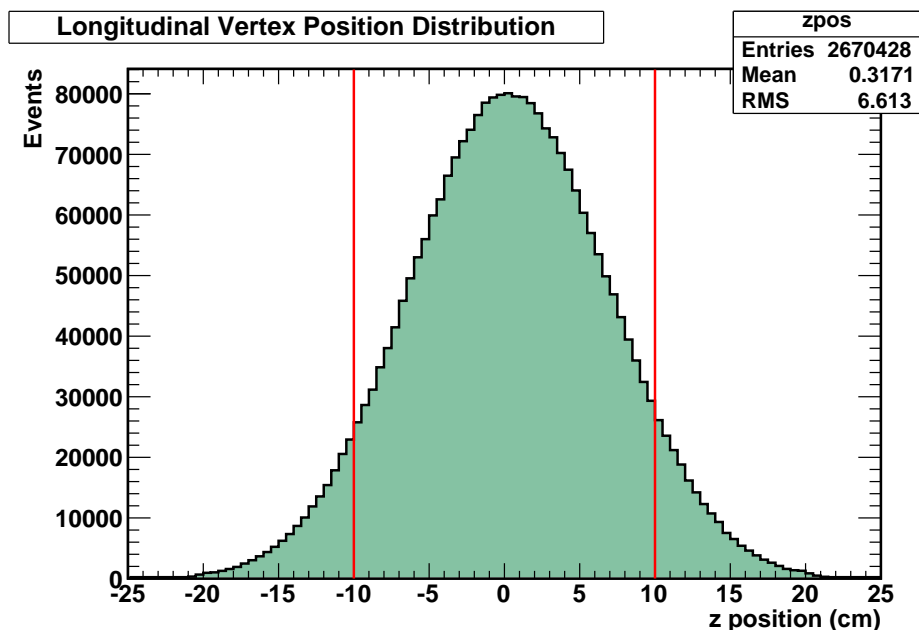


**Figure 4.1:** A distribution of the  $z$ -vertex of minimum-bias PbPb events in the CMS detector for the data used in this analysis.

## 4.3 Centrality Determination

In the CMS experiment, centrality in PbPb collisions is determined by the sum of energy in both HF detectors on either side of the collision point [66]. The distribution of the total transverse energy was made over a minimum-bias sample of events from the 2010 dataset, and corrections were applied for the efficiency of the min-bias trigger and the effects of the standard event selection. This distribution was then sliced into 2.5% bins of the total nuclear hadronic cross-sections, with the 0 – 2.5% bin containing the highest sum of HF energy corresponding to the most central events, the 2.5 – 5% bin the next most central, and so on out to the 97.5 – 100% bin containing the lowest

sum of HF energy corresponding to the most peripheral events. Figure 4.2 shows the division of HF energy into centrality bins as used in this analysis.

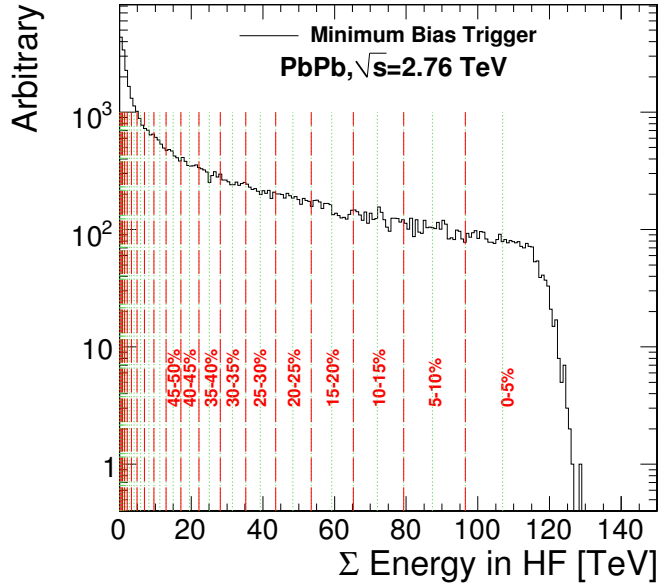


**Figure 4.2:** A plot of the sum of HF energy for minimum-bias PbPb in CMS sliced into centrality bins. The red dashed lines indicate 5% bins in centrality, with the green dotted lines marking the division into 2.5% centrality bins.

For this analysis we used the standard centrality determination provided by the Heavy Ion physics group, with the 2.5% bins further combined into 10% bins. The final centrality classes used in the analysis were 20 – 30%, 30 – 40%, 40 – 50%, 50 – 60%, 60 – 70%, and 70 – 80% centrality. The range 0 – 20% in centrality was excluded due to the very high backgrounds in the most central heavy ion collisions, and the most peripheral 80 – 100% would not produce enough neutral pions to measure a  $v_2$  anisotropy parameter with a reasonable statistical error bound.

## Chapter 5

### Analysis Methodology

The measurement of the anisotropy coefficient  $v_2$  of  $\pi^0$  mesons in CMS [62] follows the basic analysis strategy established in previous experiments, most notably previous results in the PHENIX experiment at RHIC [48, 67]. There are some aspects unique to the CMS detector, particularly the much larger contribution of conversion correlation effects due to the larger radiation length of tracker material in the CMS detector compared to PHENIX. This chapter will discuss the experimental methods used for this measurement, with a discussion of systematic uncertainties to follow in the next chapter.

#### 5.1 $\pi^0$ Reconstruction

For this analysis we reconstructed  $\pi^0$  mesons in CMS via the  $\pi^0 \rightarrow \gamma\gamma$  decay channel, by which 98.8% of  $\pi^0$  mesons decay. In order to reconstruct the daughter photons, every recorded energy deposit (rechit) in a crystal in the ECAL barrel was sorted from greatest to least energy, and these sorted rechits were used as seeds for building photon clusters. During the 2010 data taking, the ECAL was read out in Virgin Raw mode, so there was no prior zero suppression or selective readout on the rechits.

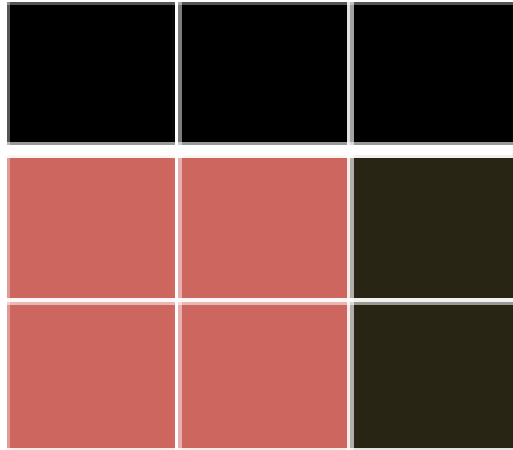


**Figure 5.1:** Diagram showing a  $3 \times 3$  cluster of ECAL crystals as used for photon candidates. The red squares define an inner  $2 \times 2$  cluster containing the seed crystal, used for computing the S4/S9 ratio.

The seeds were then taken in descending order and  $3 \times 3$  clusters were built around each seed, with seeds that have a rechit energy less than 400 MeV being discarded. Figure 5.1 provides an illustration of this clustering of ECAL rechits. This is adapted from the technique used to measure

$\pi^0$  mesons in the CMS detector for alignment and calibration (ALCA) purposes in pp collisions [64]. These  $3 \times 3$  clusters add up the total energy in each rechit neighboring the seed, with any rechit in the cluster below 200 MeV being discarded. A  $3 \times 3$  cluster size was chosen to allow for capturing most of the total deposited energy of photons while maximizing the range of  $\pi^0$   $p_T$  before clusters begin to physically overlap due to the narrowing of the opening angle. Figure 5.2 shows a comparison of  $3 \times 3$  and  $5 \times 5$  clusters for the total energy captured, and shows us that  $3 \times 3$  clusters capture over 85% of the total energy for typical photons in the  $p_T$  region of interest, merely 1 – 2% less than a  $5 \times 5$  cluster.

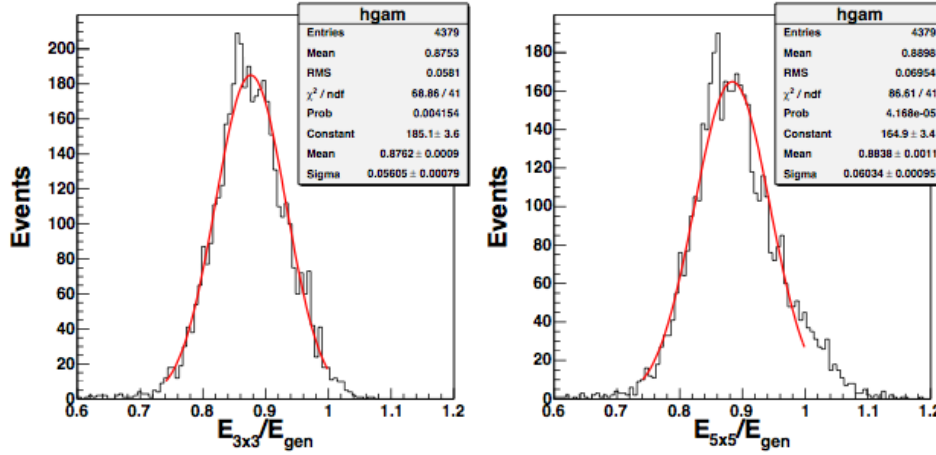


**Figure 5.2:** Left: The fraction of photon energy captured by a  $3 \times 3$  cluster of crystals in the EB, with a mean of  $0.876 \pm 0.001$ . Right: The fraction of photon energy captured by a  $5 \times 5$  cluster of crystals in the EB, with a mean of  $0.8884 \pm 0.001$ . Both plots are from particle gun simulations with 2-3 GeV photons.

A standard cut was applied by finding the highest-energy  $2 \times 2$  cluster containing the cluster seed, designated the S4, and dividing it by the total  $3 \times 3$  cluster energy, called the S9. Figure 5.1 shows the a  $2 \times 2$  subdivision within a  $3 \times 3$  cluster. Any cluster with an S4/S9 ratio less than 0.87 was discarded. The value of 0.87 was chosen by studying simulated PbPb collisions at 2.76 TeV generated from the HYDJET [68] event generator. Figure 5.3 shows distributions of the S4/S9 ratio for clusters matched to generator-level photons in central and peripheral events. The value 0.87 allows for the majority of real photons to pass the cut while excluding noise. The  $3 \times 3$  clusters that pass this cut were taken as photon candidates.

With the selected photon candidates we reconstructed the  $\gamma\gamma$  invariant mass spectrum for the event, following the formula given in equation 5.1. In this equation  $p_\gamma$  is the four-momentum of a photon candidate,  $E$  is the total energy of a photon candidate (as measured with the  $3 \times 3$  cluster), and  $\theta_{12}$  is the angle between the two photon candidates. A loop was performed over every pair photon candidates, computing the invariant mass of the pair as well as the  $p_T$ . At this point additional cuts were applied on the pairs, in order to help control the effects of photon conversions.

$$m_{\gamma_1\gamma_2} = \sqrt{p_{\gamma_1}^2 + p_{\gamma_2}^2} = \sqrt{2E_1E_2\cos[1 - \theta_{12}]} \quad (5.1)$$

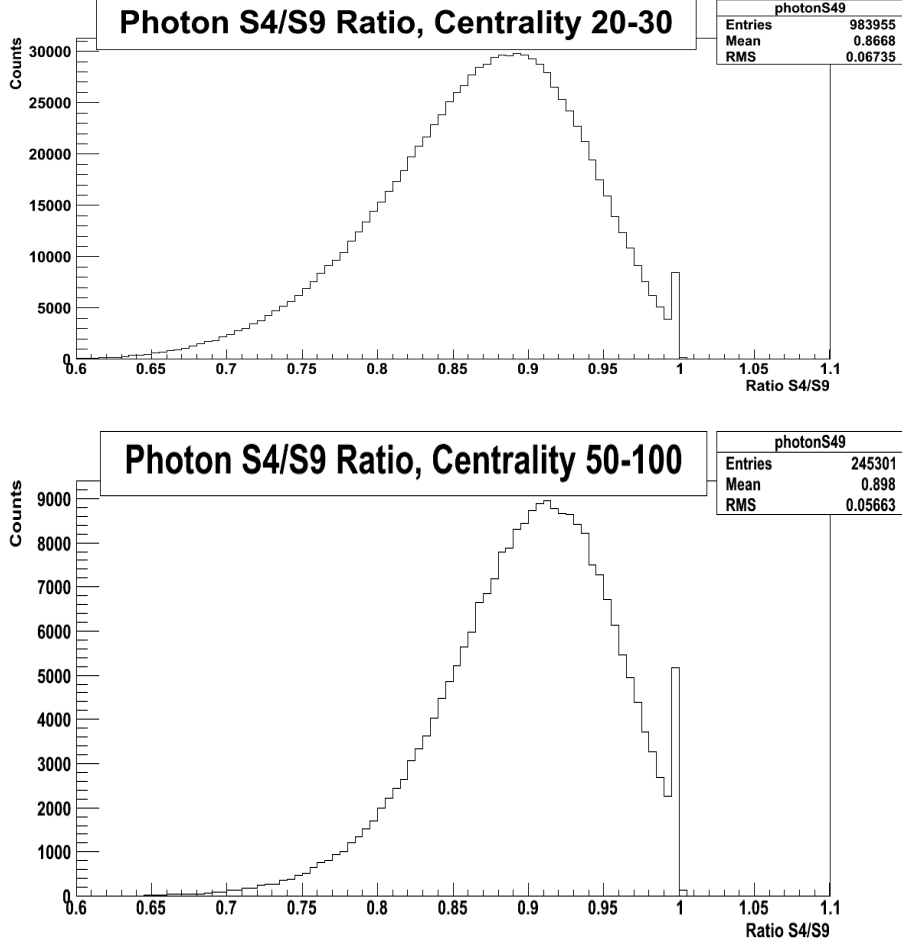


**Figure 5.3:** Top: A distribution of the S4/S9 ratio of reconstructed photons in the 20–30% centrality class. Bottom: A distribution of the S4/S9 ratio of reconstructed photons in the combined 50–100% centrality class. Both plots are from HYDJET simulations of PbPb at  $\sqrt{S_{NN}} = 2.76$  TeV. Reconstructed photons were matched to generator-level photons to measure the distributions.

As photons pass through the material of the silicon strip tracker, there is a chance for the photons to interact and convert into  $e^+e^-$  pairs. Figure 5.4 shows the photon conversion probability as a function of  $\eta$ . If the resulting electrons and positrons have sufficient momentum they will reach the ECAL and deposit energy which can result in reclustered clusters that pass the S4/S9 cut and contribute to the combinatorial background. The specific effects of these photon conversions on the combinatorial background will be discussed in the following section, and a detailed explanation of photon conversions in the CMS detector and possibilities for mitigating them in future analyses is presented in Appendix A.

The first cut applied was a  $p_T$ -dependent minimum opening angle cut, described in equation 5.2, where the parameters “a” and “b” were determined from PYTHIA 6.422 [70] simulations, seen in Figure 5.5. Any photon pairs with an opening angle between them smaller than 70% of this value were discarded. This is similar to  $\pi^0$  analyses performed at other experiments, particularly the

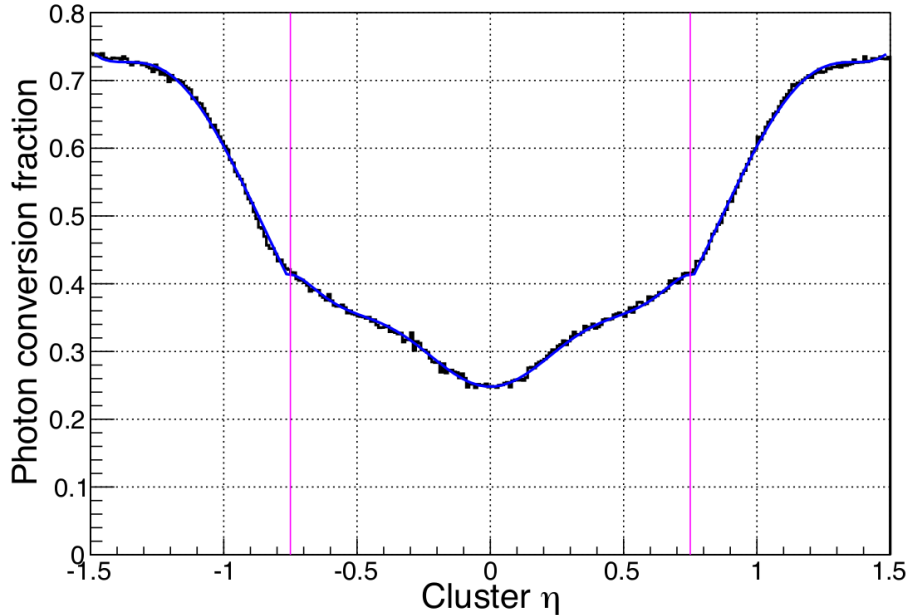


**Figure 5.4:** A plot of the probability for single photons to convert into  $e^+e^-$  pairs through interaction with the CMS silicon tracker as a function of  $\eta$ , determined as the fraction of generator photons to undergo a conversion from HIJING [69] simulations of pPb events. The solid magenta lines indicate  $\pm 0.75$  in  $\eta$ , and the blue curve is two sets of polynomial fits to the histogram in the region  $|\eta| < 0.75$  and  $|\eta| > 0.75$ .

PHENIX experiment at RHIC. The second cut was an additional  $p_T$ -dependent minimum cluster separation cut, similar in form to the opening angle cut in equation 5.2. The parameters for this cut were determined by a functional fit to cluster separation in cm determined from additional PYTHIA simulations, as shown in Figure 5.6.

$$\theta_{\gamma_1\gamma_2} \geq \frac{a}{p_T} + \frac{b}{p_T^2} \quad (5.2)$$

In addition, there was a cut restricting all  $\pi^0$  candidates to  $|\eta| < 0.8$  within the ECAL barrel. This was in order to allow a direct comparison with CMS results for the azimuthal anisotropy of inclusive charged particles in PbPb at 2.76 TeV  $\sqrt{S_{NN}}$ . This restricted  $\eta$  range also minimizes the effects of photon conversions, due to the smaller radiation length of the silicon strip tracker in this region, but photon conversion effects do not preclude future analyses with a larger  $\eta$  range.

Pairs that pass the opening angle and cluster separation cuts within the  $|\eta| < 0.8$  window were then used to compute the same-event invariant mass spectrum which consists of the  $\pi^0$  peak itself, the uncorrelated background, and any same-event correlations that arise from other effects, most notably photon conversions. In order to extract the yield we also constructed a mixed-event invariant mass spectrum in order to subtract the uncorrelated background, which is described in the next section.

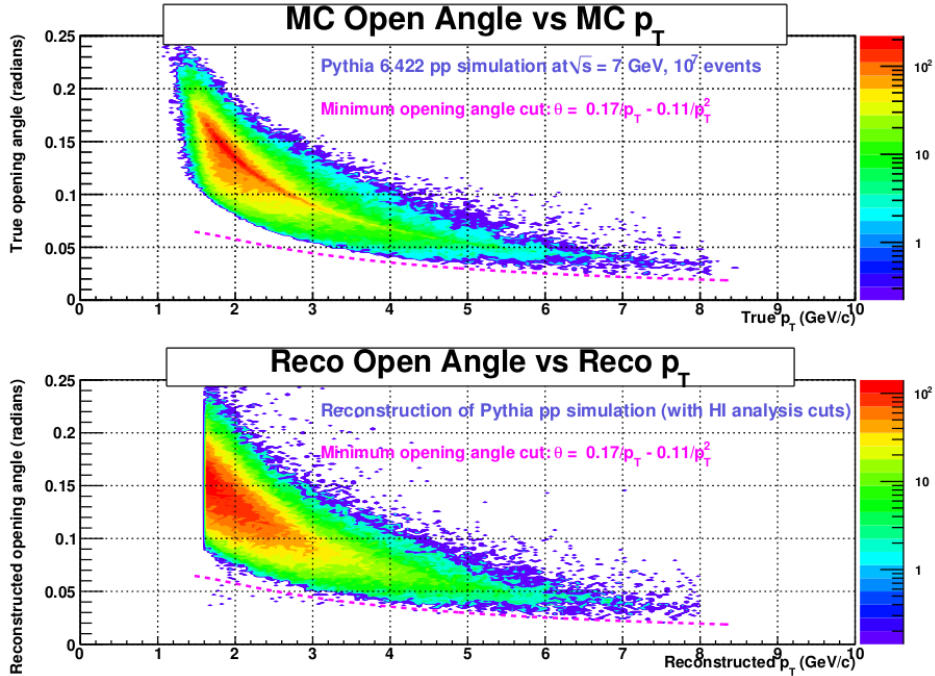


**Figure 5.5:** Top: A distribution of  $\pi^0$  decay photon opening angle vs  $\pi^0 p_T$ , with the opening angle and  $p_T$  taken from generator level information. Bottom: distribution of  $\pi^0$  decay photon opening angle vs  $\pi^0 p_T$ , with the opening angle and  $p_T$  determined from reconstructed photon kinematics from  $3 \times 3$  clusters. The magenta dashed line shows the fit function for minimum opening angle determined from  $\sqrt{S} = 7$  TeV pp simulations.

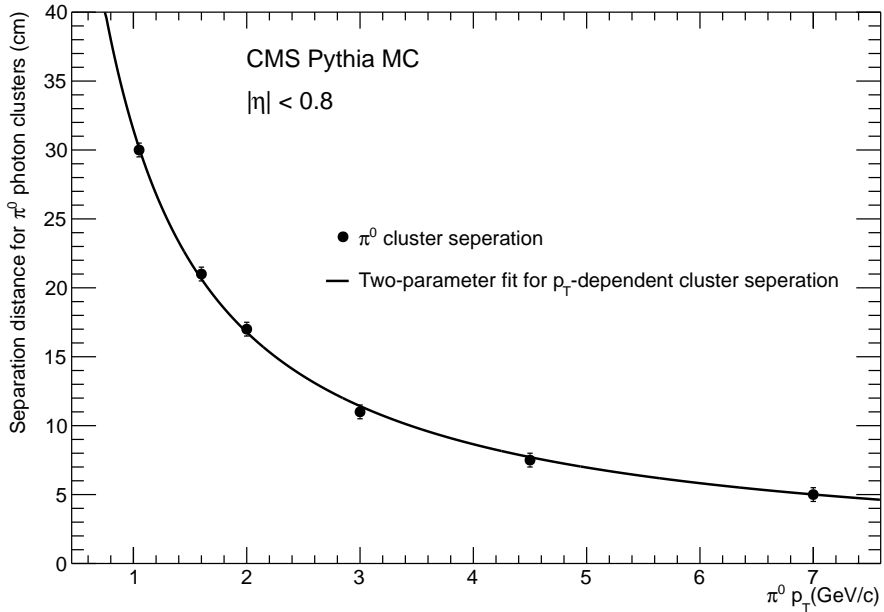


**Figure 5.6:** Cluster separation in cm as a function of  $\pi^0 p_T$  in simulated 7 TeV  $\sqrt{S}$  pp events. The red line shows the two-parameter fit function used to determine the cluster separation cut.

## 5.2 Event Mixing Technique

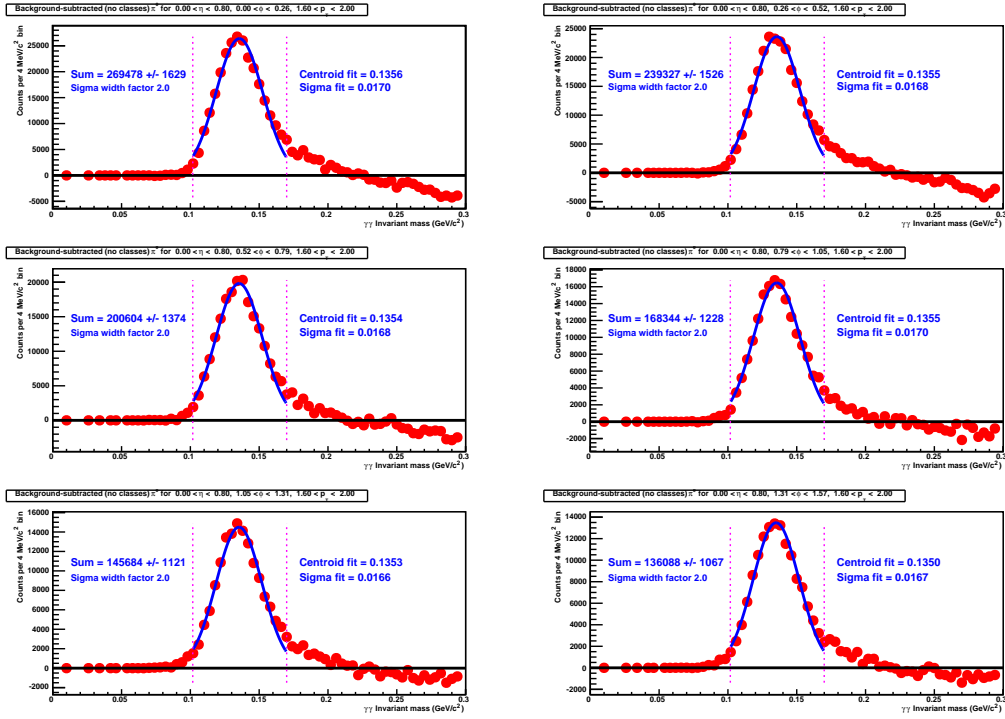
In order to extract the  $\pi^0$  peak from the invariant mass spectrum, we employed a standard event mixing technique that allows us to subtract out the uncorrelated background. This strength of the event mixing technique is that it is a data-driven method for computing the uncorrelated background, with no parameterized fitting. Every event was classified into six bins in centrality as previously described in section 4.3, six bins in the z-vertex position with  $\delta z = 5$  cm, and six bins in event-plane angle in the range  $0 < \phi_{EP} < \pi$ . Each event was classified into one of these sets of bins in an array, and a buffer of events in each class was kept three events deep.

To create the mixed-event background, the same procedure was used to construct the invariant mass spectrum as in the same events, except that the loop paired all the photon candidates from one event with the photon candidates from the three saved events in the same centrality, z-vertex, and event-plane bins. Two photons from different events cannot be correlated with each other, so the resulting invariant mass spectrum must be the result of the pure uncorrelated background. All of the same cuts were applied to the mixed-event background as in the same events, including the opening angle and cluster separation cuts and were produced in the same  $p_T$  bins for the resulting photon pairs, in order to match the exact conditions of the same events.

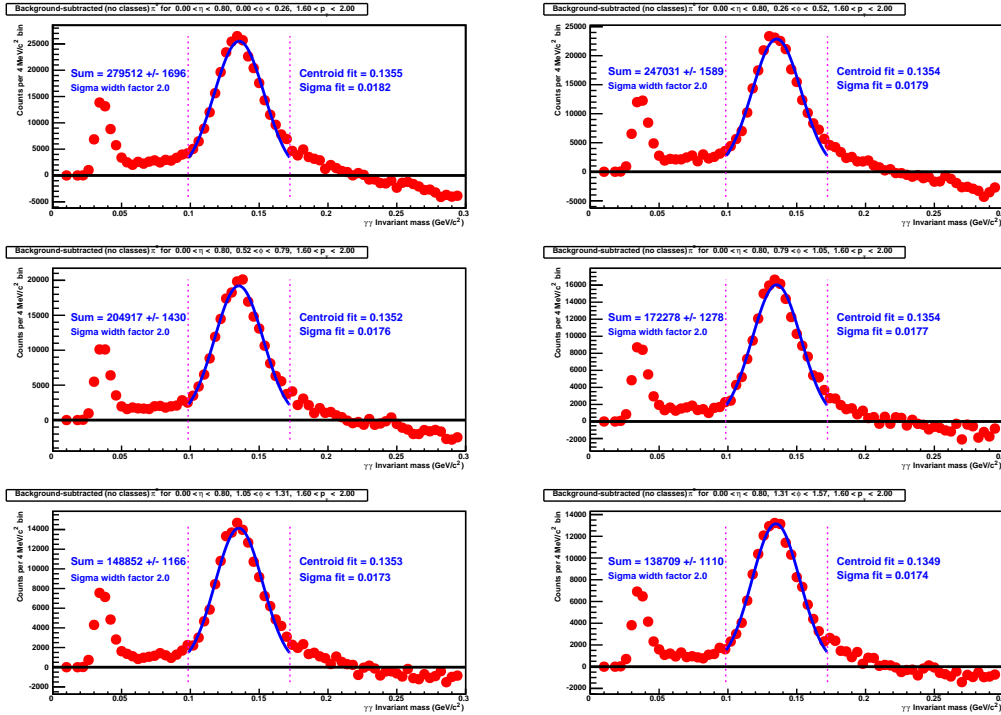
Once the mixed-event background was computed, it was normalized to the same-event foreground in the same class in a region of the spectrum well away from the  $\pi^0$  invariant mass peak, in the region  $0.20 < m_{\gamma\gamma} < 0.25$  GeV/c<sup>2</sup>. After being normalized, the mixed-event spectrum was subtracted from the same-event foreground, leaving behind ideally just the  $\pi^0$  mass peak. However there are also other correlations within an event that distorts the shape of the foreground away from that of the uncorrelated background. The most significant of these effects is the photon conversion correlations.

Figure 5.7 shows an example of the mixed-event background subtraction in PbPb data from CMS, with all of the standard selection cuts for  $\pi^0$  candidates. Figure 5.8 shows an example of the mixed-event background subtraction from the same data without the opening angle and cluster separation cuts, for illustration. In both Figures there is a noticeable oversubtraction on the high-mass side of the  $\pi^0$  peak. Without the opening angle and cluster separation cuts an undersubtraction can be observed on the low-mass side of the peak in Figure 5.8. These over- and undersubtraction effects were created by the same-event correlations caused by photon conversions, which lead to misreconstructed  $\pi^0$  candidates with a distorted mass and  $p_T$ .

Figure 5.9 shows a decomposition of the effects of photon conversions, obtained from a particle gun simulation of  $\pi^0$  mesons that were allowed to convert in the tracker. Here photon candidate clusters were matched to the generator-level information of daughter photons from  $\pi^0$  decays in order to identify photons that did not convert, and to determine which clusters did not match to a daughter photon, which must be from conversion electrons. The dominant contribution underlying the true  $\pi^0$  peak comes from cases where one photon has not converted and it is matched with a cluster from a conversion electron, which results in the very broad peak partially underlying the  $\pi^0$  mass peak. Figure 5.10 shows a comparison of real data to simulations, showing how the effects of over- and undersubtraction disappear when conversion photons are rejected. Section 6.2 explains how we took into account the uncertainties introduced by this effect when extracting the  $\pi^0$  yield.



**Figure 5.7:** Background-subtracted invariant mass spectrum based on S4/S9 ratio cuts and standard  $p_T$  dependent opening angle and cluster separation cuts, in 6 bins of angle with respect to the event plane. Taken from CMS PbPb events at  $\sqrt{S_{NN}} = 2.76$  TeV, in the 40 – 50% centrality class, with  $\pi^0$   $p_T$  in the range  $1.6 < p_T < 2.0$  GeV/c.



**Figure 5.8:** Background-subtracted invariant mass spectrum based on S4/S9 ratio cuts with no  $p_T$  dependent opening angle and cluster separation cuts, in 6 bins of angle with respect to the event plane. Taken from CMS PbPb events at  $\sqrt{s_{NN}} = 2.76$  TeV, in the 40 – 50% centrality class, with  $\pi^0$   $p_T$  in the range  $1.6 < p_T < 2.0$  GeV/c. Same-event correlation artifacts on the low-mass side become less prominent in higher  $p_T$  bins, as fewer clusters from conversion electrons pass cluster selection cuts.

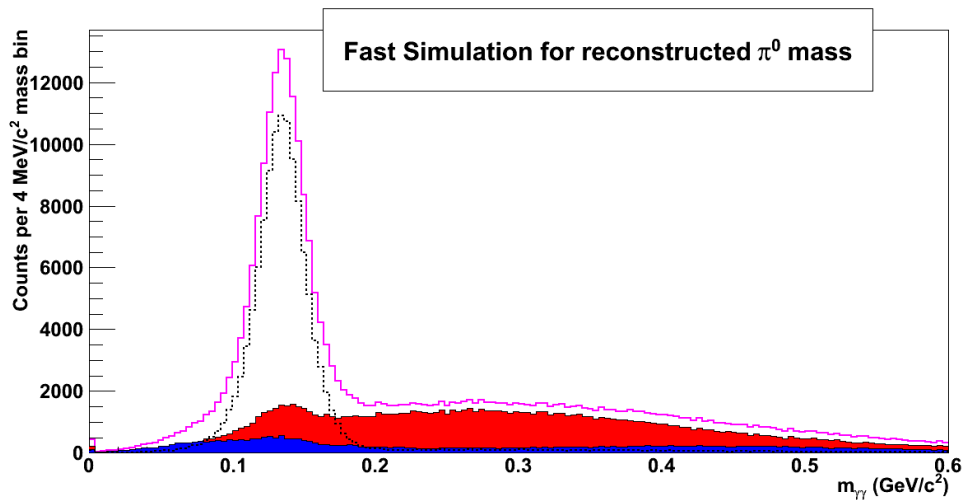


**Figure 5.9:** A plot of the different contributions to the  $m_{\gamma\gamma}$  invariant mass spectrum, determined from single  $\pi^0$  particle gun simulations where the decay photons are allowed to convert in the CMS silicon tracker. The solid blue region designates the spectrum where neither cluster is matched to a photon, resulting from conversion electrons. The solid red region designates the spectrum where one cluster is matched to a  $\pi^0$  decay photon and the other cluster is unmatched, resulting from a conversion electron. The dotted black line designates the spectrum where both clusters are matched to decay photons with no conversions. The magenta line shows the sum of all three components, illustrating the extended distortion of the  $\pi^0$  peak on the high-mass side.

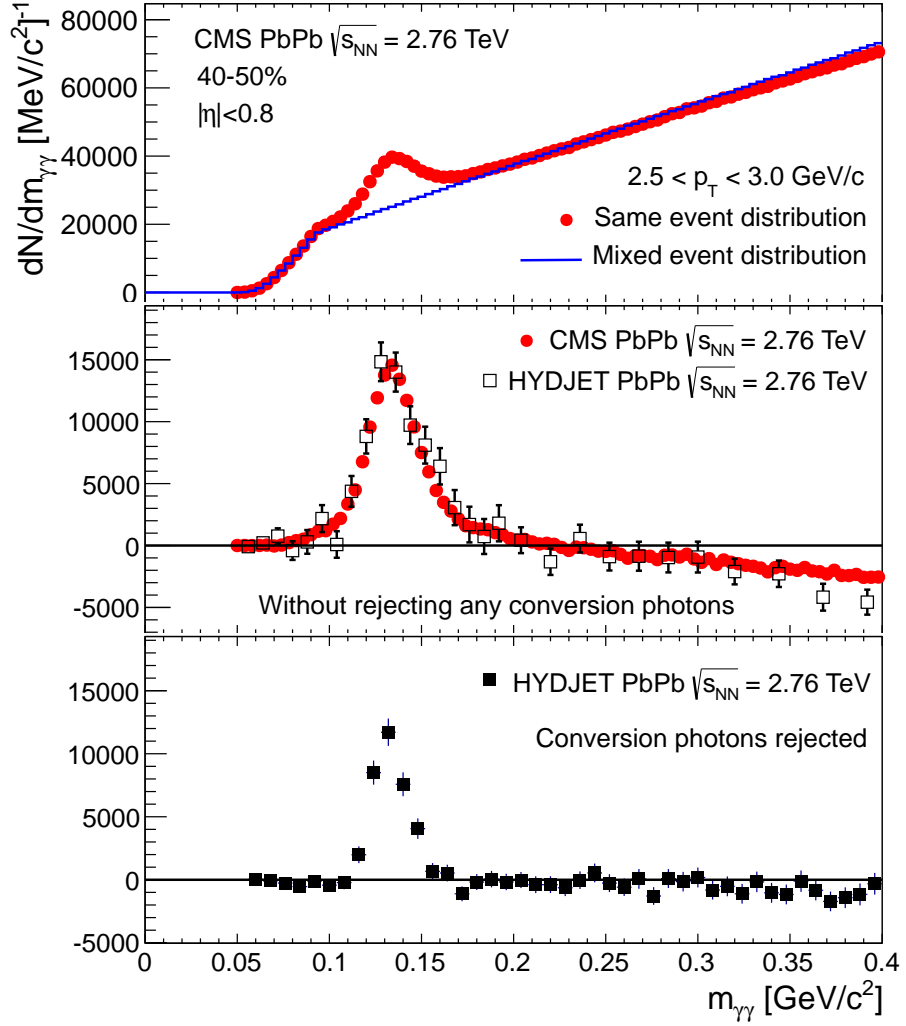


**Figure 5.10:** Top panel:  $m_{\gamma\gamma}$  invariant mass distribution from CMS PbPb data at 2.76 TeV  $\sqrt{s_{NN}}$ , with normalized mixed-event background in blue, from 40 – 50% centrality class with  $\pi^0$   $p_T$  from 2.5 to 3 GeV/c. Middle panel: Background-subtracted invariant mass spectrum from the same centrality and  $p_T$  bin. Square points are from background-subtracted invariant mass generated from HYDJET PbPb in the same centrality and  $p_T$  bin. Bottom panel: Background-subtracted invariant mass generated from HYDJET PbPb in the same centrality and  $p_T$  bin, but with conversion photons rejected, eliminating oversubtraction effects on the high-mass side.

### 5.3 Yield Extraction and Efficiency Corrections

The same-event spectrum and mixed-event background was measured in each centrality class from 20 – 80% centrality in 10% bins, in each of six  $p_T$  bins with the bins 1.6 – 2, 2 – 2.5, 2.5 – 3, 3 – 4, 4 – 6, and 6 – 8 GeV/c in  $p_T$ . These invariant mass distributions were further subdivided into six bins of angle between the  $\pi^0$  candidate and the event plane, given in equation 5.3, with the  $\Delta\Phi$  angle symmetrized to fall between 0 and  $\pi/2$ . The  $\Delta\Phi$  yields are guaranteed to be symmetrical about  $\pi/2$  due to the even order of  $\cos^2\Delta\phi$ . Details of the event plane definition and reconstruction can be found in the next section. The yields in these  $\Delta\Phi$  bins were used as the ingredients to calculate the  $\pi^0 v_2$  in each centrality class and  $p_T$  bin by the Event-Plane Method, discussed in the next section.

$$\Delta\Phi = |\Psi_{\text{EP}} - \phi_{\pi^0}| \quad (5.3)$$

After the background subtraction was performed to extract a  $\pi^0$  mass peak, a Gaussian fit was performed on the peak in order to calculate the mean  $\mu$  and the width  $\sigma$  of the peak. An example is shown in Figure 5.11. To measure the yield, an integration of the counts in a window of  $\pm 2\sigma$  around the mean ( $\mu - 2\sigma, \mu + 2\sigma$ ) was performed, with the result taken as the raw  $\pi^0$  yield for that bin.

In order to calculate the final  $\pi^0$  yields in each bin corrections were made for inefficiencies in reconstructing true  $\pi^0$  mesons, which may arise from detector effects, high occupancy from the large heavy ion background, and photon conversion effects. As the final result depends only on the relative yields in different  $\Delta\Phi$  bins, we did not need to correct for the absolute efficiency in reconstructing  $\pi^0$  mesons, but only the relative efficiencies in various bins of centrality,  $p_T$ , and  $\Delta\Phi$ .

To determine the efficiency effects we performed an embedding study, embedding 10 simulated  $\pi^0$  mesons into each of 100,000 minimum-bias heavy ion events taken from real data. For this study 20,000 events were recycled 5 times each with different embeddings each time in order to produce the 100,000 embedded events, in order to reduce processing time and disk space. The 10 simulated  $\pi^0$  mesons were randomly distributed in  $360^\circ$  in  $\phi$ ,  $|\eta| < 1$  in pseudorapidity, and from 0.2 to 10 GeV/c in  $p_T$  with a uniform distribution. The events were then reconstructed with the standard HI sequence for PbPb data in CMS, using GEANT 4 to interact the simulated particles with the detector and processed with our  $\pi^0$  reconstruction software. Photon candidate clusters from the data were matched to generator-level photons from the embedded  $\pi^0$  mesons and then reconstructed into pair candidates using the standard selection cuts for this analysis. The efficiency was calculated by determining how many of the embedded  $\pi^0$  mesons were successfully reconstructed. Matching between generator-level photons and reconstructed clusters was accomplished by matching in  $\Delta\eta = \eta_{\text{gen}} - \eta_{\text{reco}}$  and  $\Delta\phi = \phi_{\text{gen}} - \phi_{\text{reco}}$ . Figure 5.12 shows matching residuals for  $\Delta\eta$  and  $\Delta\phi$  in the 20 – 30% centrality bin, and Figures 5.13 shows these residuals for the 70 – 80% centrality bin to allow for comparison.

Results of the embedding study can be seen in Figures 5.14 and 5.15, showing the  $\pi^0$  reconstruction efficiency in different centrality classes as a function of  $p_T$ ,  $\eta$ , and  $\Delta\Phi$ . The efficiency was found

to be roughly flat as a function of  $\eta$  within the region  $|\eta| < 0.8$ , and similarly flat as a function of  $\Delta\Phi$  between 0 and  $90^\circ$  in the  $p_T$ -integrated region. A strong dependence on  $p_T$  was observed for each centrality bin, first rising sharply from 0 to a maximum at roughly 4 GeV/c, and then falling slowly as the  $p_T$  increases towards 8 GeV/c.

Figures 5.16 and 5.17 shows an example of the efficiency as a function of  $\Delta\Phi$  in separate  $p_T$  bins. A constant fit was applied and compared to a linear fit, and the change in the probability of the fit used to determine whether a significant change in efficiency was present. A dependence was observed for 20 – 30% centrality in the lower  $p_T$  bins with efficiency higher near  $\Delta\Phi = 0$ , and falling linearly towards  $\Delta\Phi = 90$ . Figures 5.18 and 5.19 show the efficiency as a function of  $\Delta\Phi$  in the 70 – 80% centrality bin for comparison, where no significant variation from a constant fit was observed.

The increased efficiency for  $\pi^0$  mesons emitted parallel to the event plane (in-plane) vs those emitted perpendicular to the event-plane (out-of-plane) in more central events comes from a “promotion effect” whereby clusters that would have not passed minimum energy cuts are “promoted” by sitting on top of a high-occupancy background in the direction of the event plane. The change in efficiency was extracted from the linear fit to the points in each  $\Delta\Phi$  bin for each  $p_T$  and centrality.

In the 20 – 30%, 30 – 40%, 40 – 50%, and 50 – 60% centralities, corrections were made for both the in-plane efficiency and the  $p_T$ -dependent efficiency in the 1.6-2, 2-2.5, and 2.5-3 GeV/c  $p_T$  bins. The correction was performed by weighting the raw  $\pi^0$  yields by  $1/\epsilon$ , with  $\epsilon$  being the measured efficiency in that bin. Figure 5.20 shows an example of the corrections for 20 – 30% centrality. For higher  $p_T$  bins in these centrality classes, and for all  $p_T$  bins in the 60 – 70% and 70 – 80% centrality classes, efficiency corrections were found to be small and were only used as a source of systematic uncertainty. Systematic uncertainties from efficiency corrections are discussed in section 6.3.

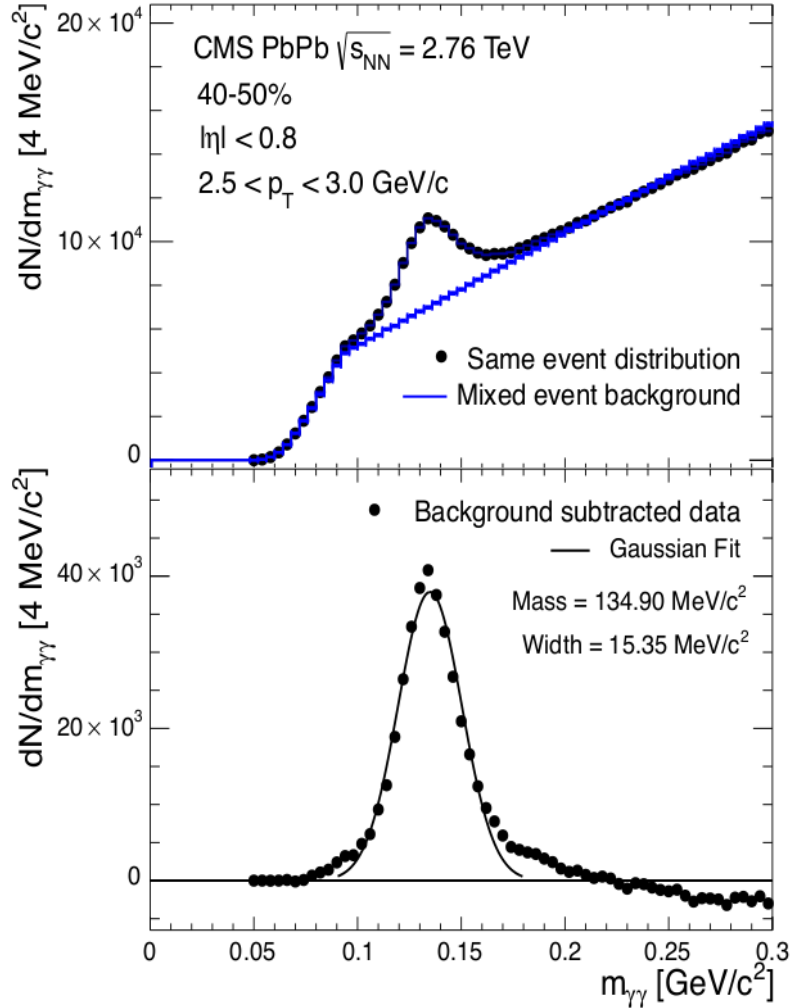


**Figure 5.11:** Top panel:  $m_{\gamma\gamma}$  invariant mass distribution from CMS PbPb data at 2.76 TeV  $\sqrt{s_{NN}}$ , with normalized mixed-event background in red, from 40 – 50% centrality class with  $\pi^0$   $p_T$  from 2.5 to 3 GeV/c. Bottom panel: Background-subtracted invariant mass spectrum from the same centrality and  $p_T$  bin. The black line shows a Gaussian fit to the  $\pi^0$  peak, used to extract the mean and the width of the peak.

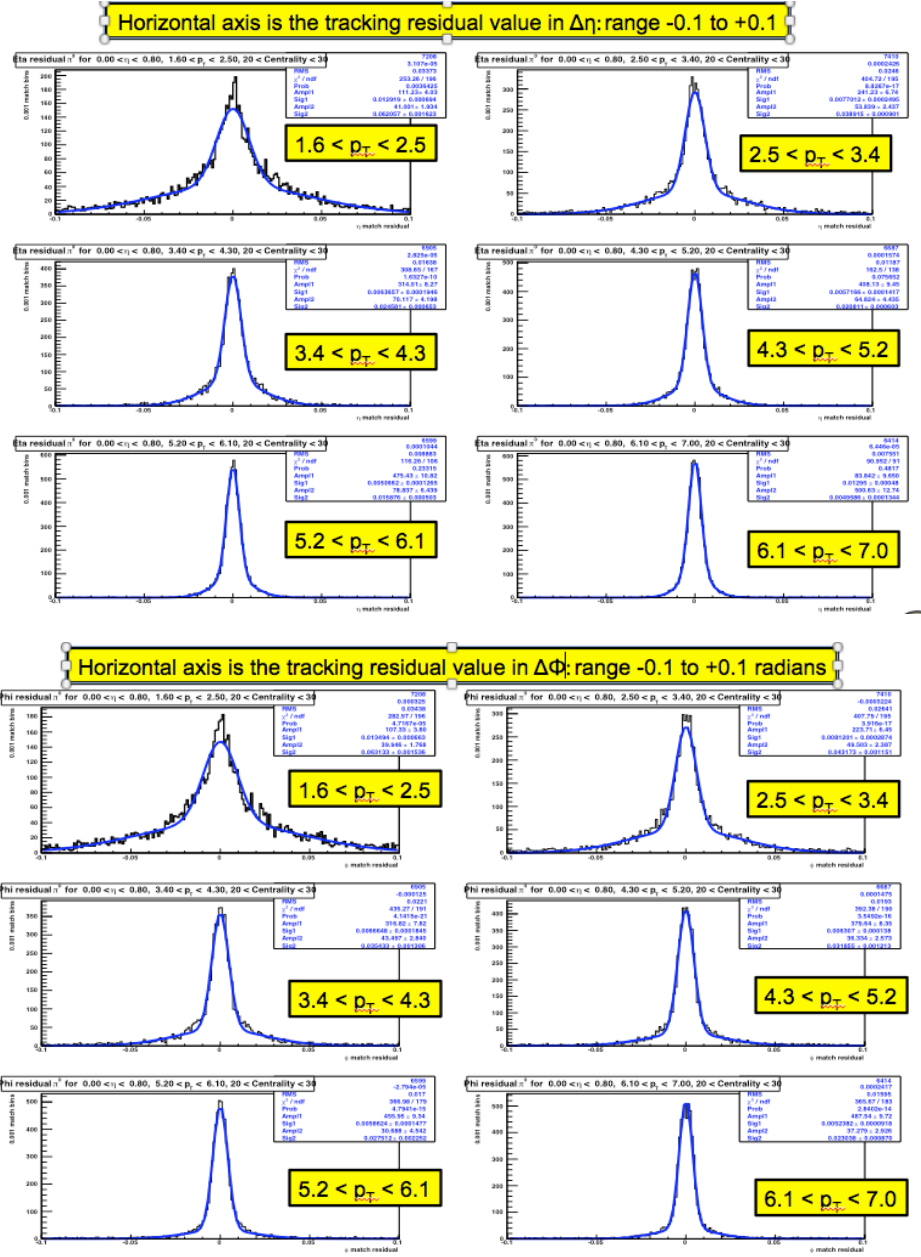


**Figure 5.12:** Top: Matching residuals in  $\Delta\eta = \eta_{gen} - \eta_{reco}$  for  $\pi^0$  decay photons in six  $\pi^0$   $p_T$  bins in 20 – 30% centrality. Bottom: Matching residuals in  $\Delta\phi = \phi_{gen} - \phi_{reco}$  for  $\pi^0$  decay photons in six  $\pi^0$   $p_T$  bins in 20 – 30% centrality. Calculated from HYDJET PbPb MC at  $\sqrt{S_{NN}} = 2.76$  TeV.

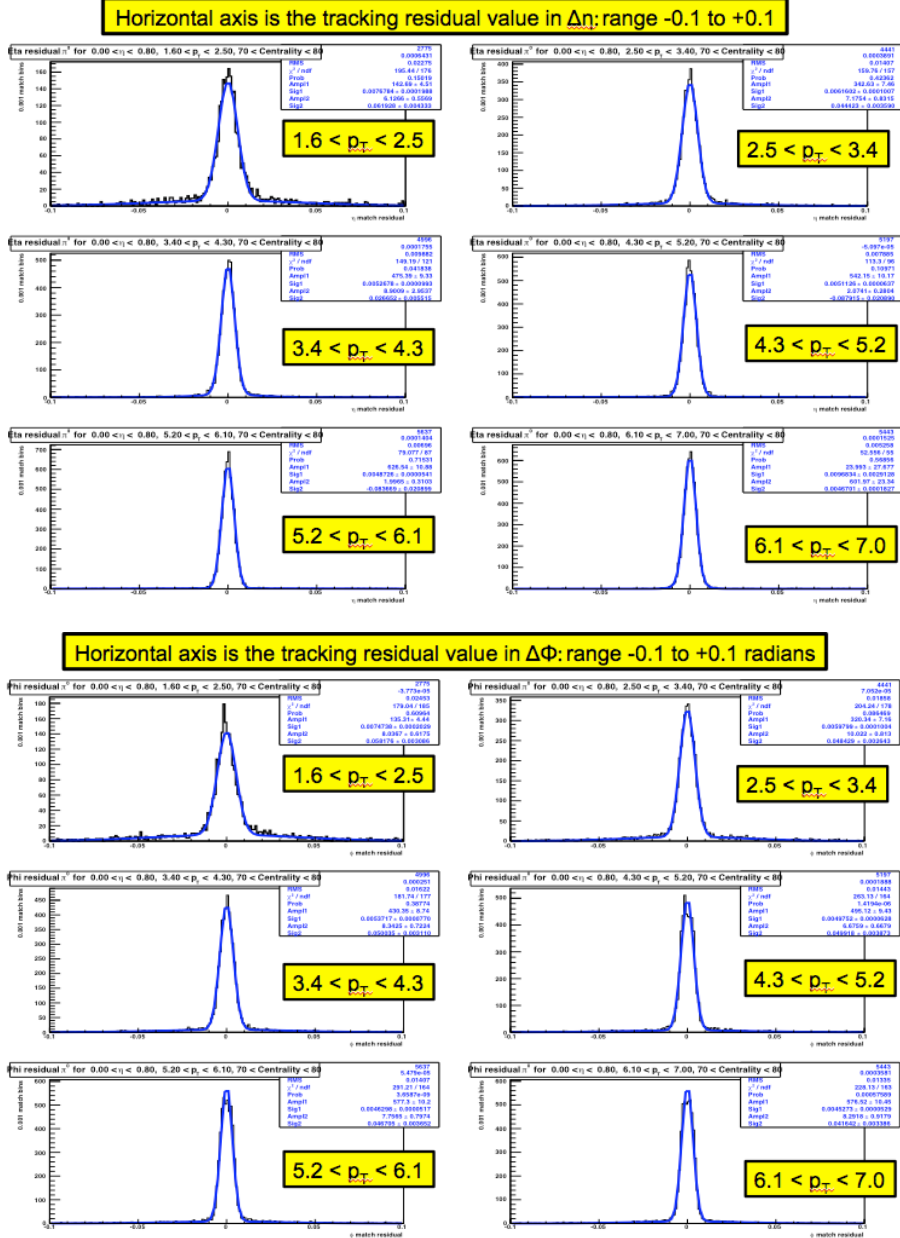


**Figure 5.13:** Top: Matching residuals in  $\Delta\eta = \eta_{gen} - \eta_{reco}$  for  $\pi^0$  decay photons in six  $\pi^0$   $p_T$  bins in 70 – 80% centrality. Bottom: Matching residuals in  $\Delta\phi = \phi_{gen} - \phi_{reco}$  for  $\pi^0$  decay photons in six  $\pi^0$   $p_T$  bins in 70 – 80% centrality. Calculated from HYDJET PbPb MC at  $\sqrt{S_{NN}} = 2.76$  TeV.

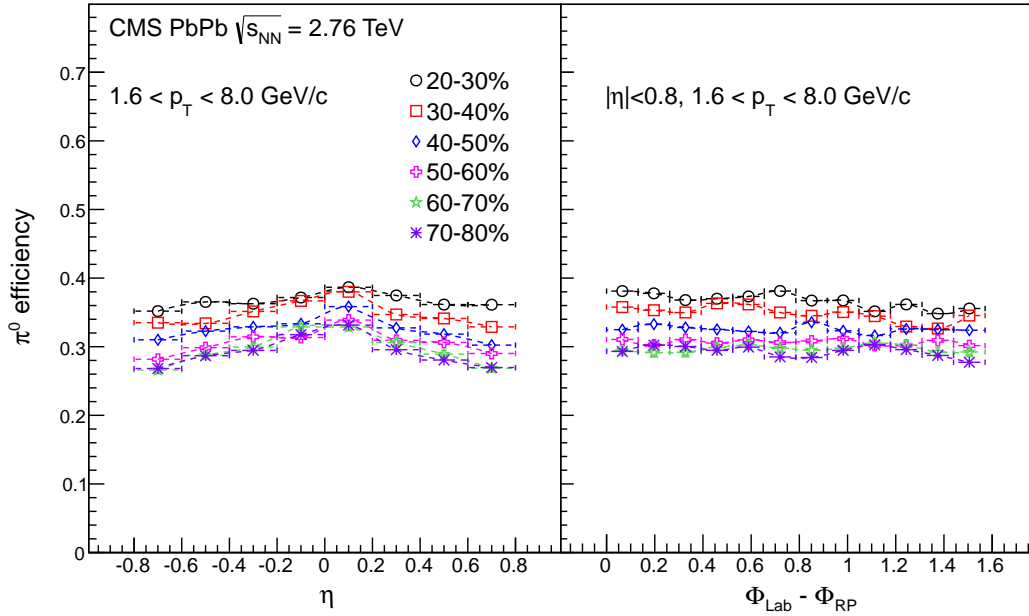


**Figure 5.14:**  $\pi^0$  reconstruction efficiency as a function of  $\eta$  and  $\Delta\Phi$  in six centrality bins, calculated from embedding studies. Results presented are integrated in  $p_T$ .

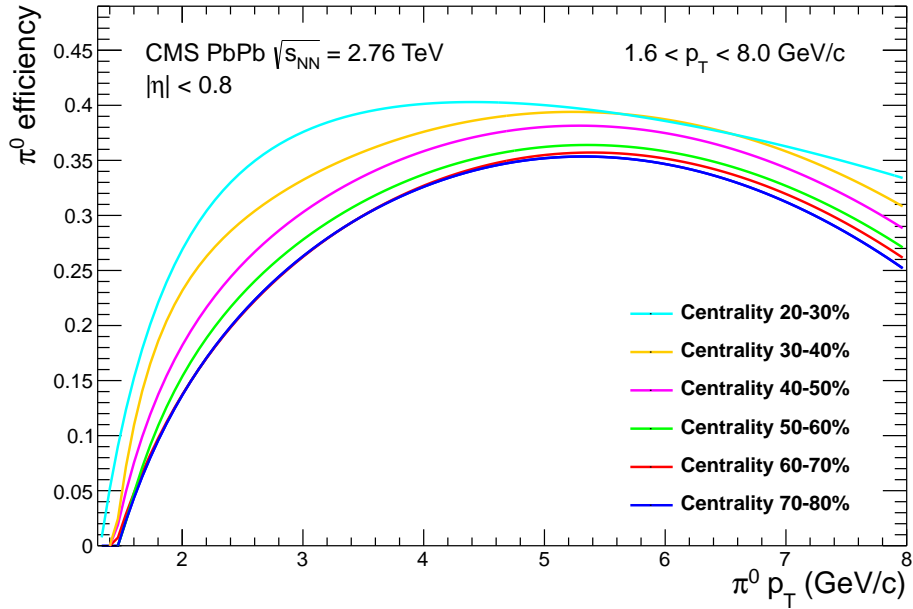


**Figure 5.15:** Fit functions for  $\pi^0$  reconstruction efficiency as a function of  $p_T$  in six centrality bins, calculated from embedding studies. Results presented are integrated in  $\eta$  and  $\Delta\Phi$ .

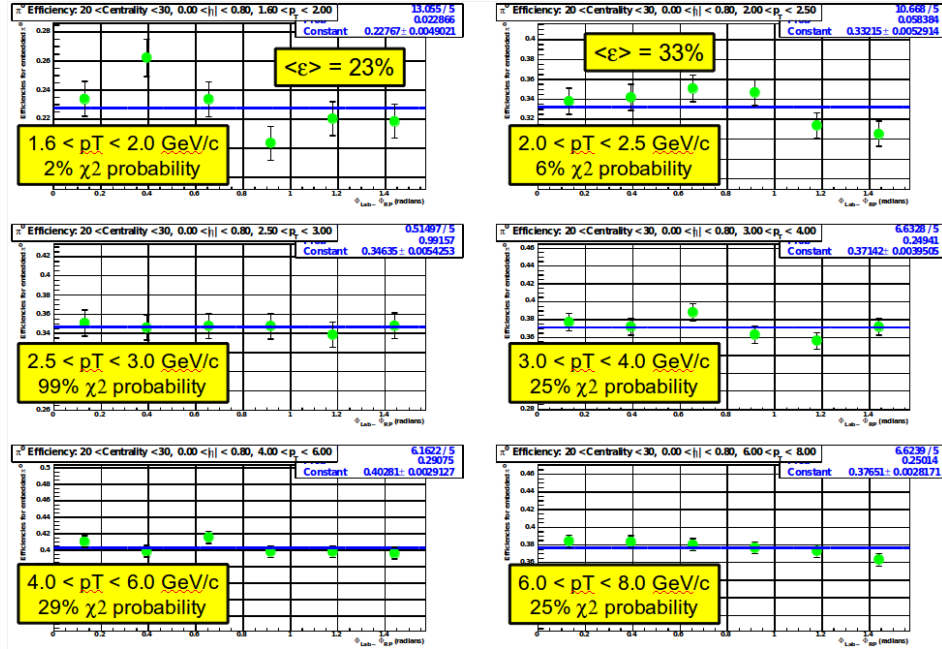


**Figure 5.16:** The  $\pi^0$  reconstruction efficiency as a function of  $\Delta\Phi$  in six  $p_T$  bins at 20–30% , calculated from embedding studies. A constant fit was made to the data to determine the  $\chi^2$  goodness of fit and to determine variation of efficiency with respect to  $\Delta\Phi$ .

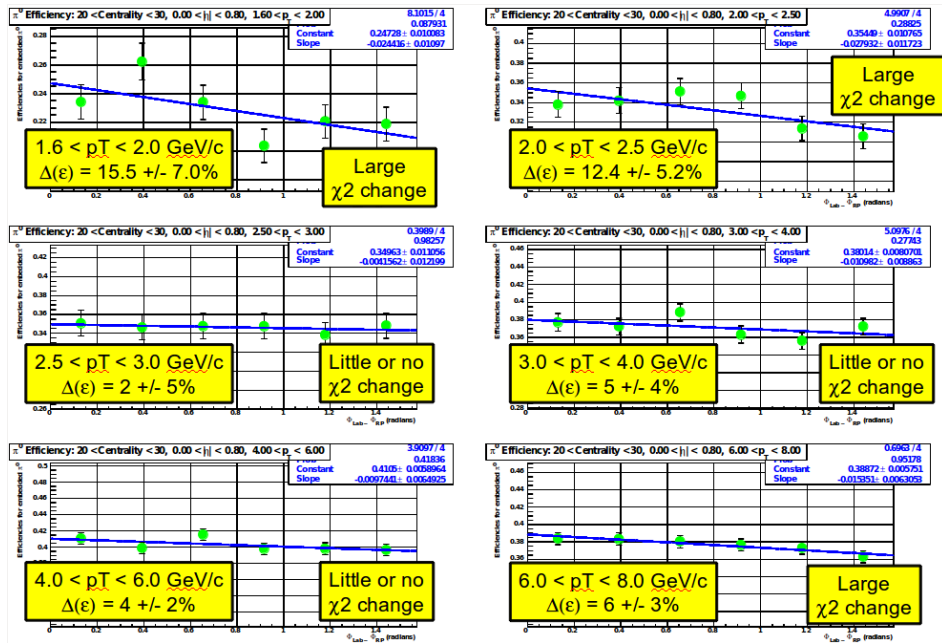


**Figure 5.17:** The  $\pi^0$  reconstruction efficiency as a function of  $\Delta\Phi$  in six  $p_T$  bins at 20–30% , calculated from embedding studies. A linear fit was made to the data to determine the  $\chi^2$  goodness of fit and to determine variation of efficiency with respect to  $\Delta\Phi$ . A better  $\chi^2$  for the linear fit vs a constant fit was observed for the lowest three  $p_T$  bins, indicating a  $\Delta\Phi$  dependence to the efficiency.

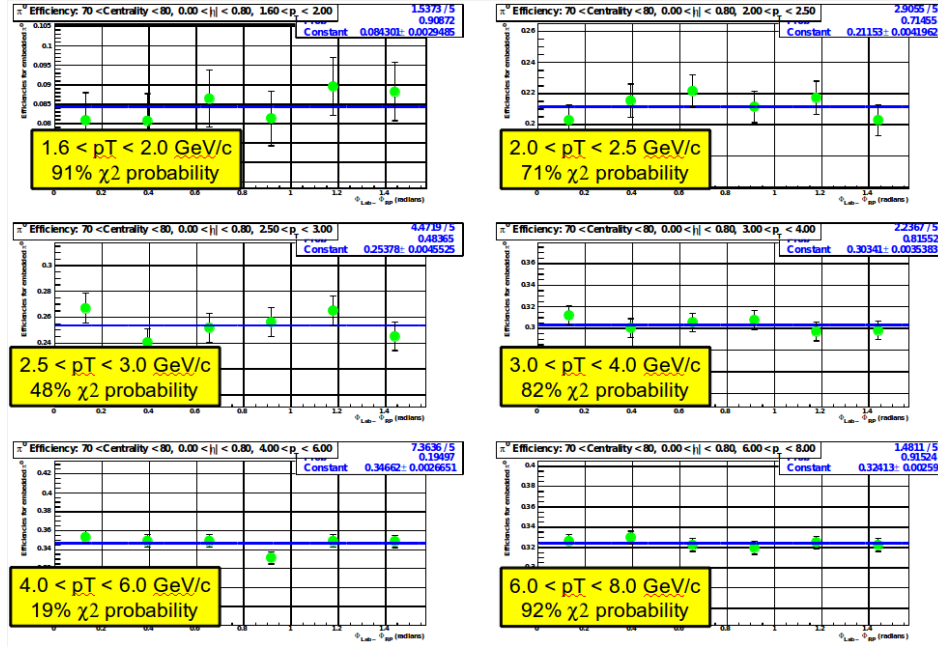


**Figure 5.18:** The  $\pi^0$  reconstruction efficiency as a function of  $\Delta\Phi$  in six  $p_T$  bins at 70–80% , calculated from embedding studies. A constant fit was made to the data to determine the  $\chi^2$  goodness of fit and to determine variation of efficiency with respect to  $\Delta\Phi$ .

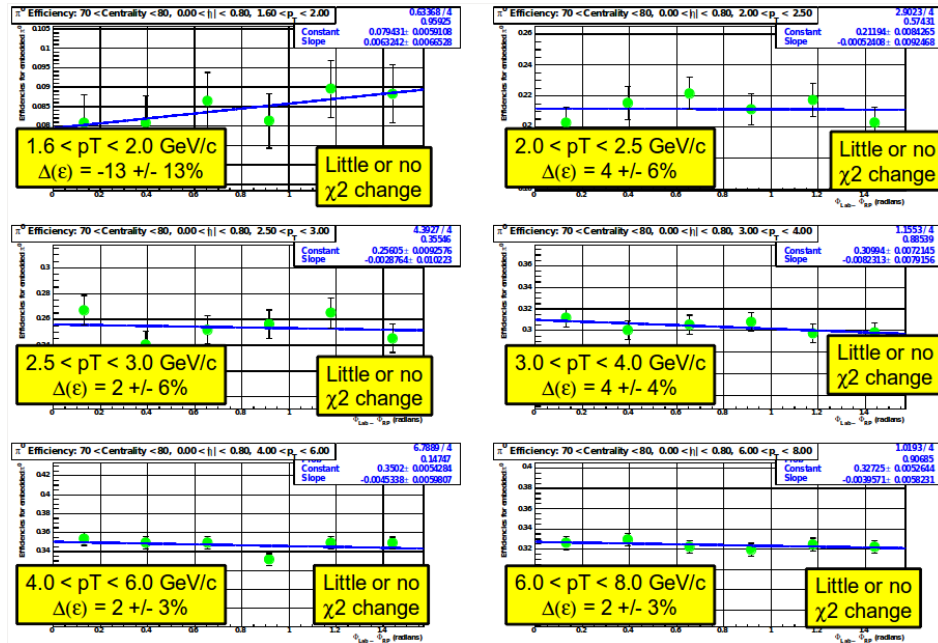


**Figure 5.19:** The  $\pi^0$  reconstruction efficiency as a function of  $\Delta\Phi$  in six  $p_T$  bins at 70–80% , calculated from embedding studies. A constant fit was made to the data to determine the  $\chi^2$  goodness of fit and to determine variation of efficiency with respect to  $\Delta\Phi$ . No significant improvement in  $\chi^2$  was observed for a linear fit vs a constant fit, suggesting no significant variation in efficiency as a function of  $\Delta\Phi$ .

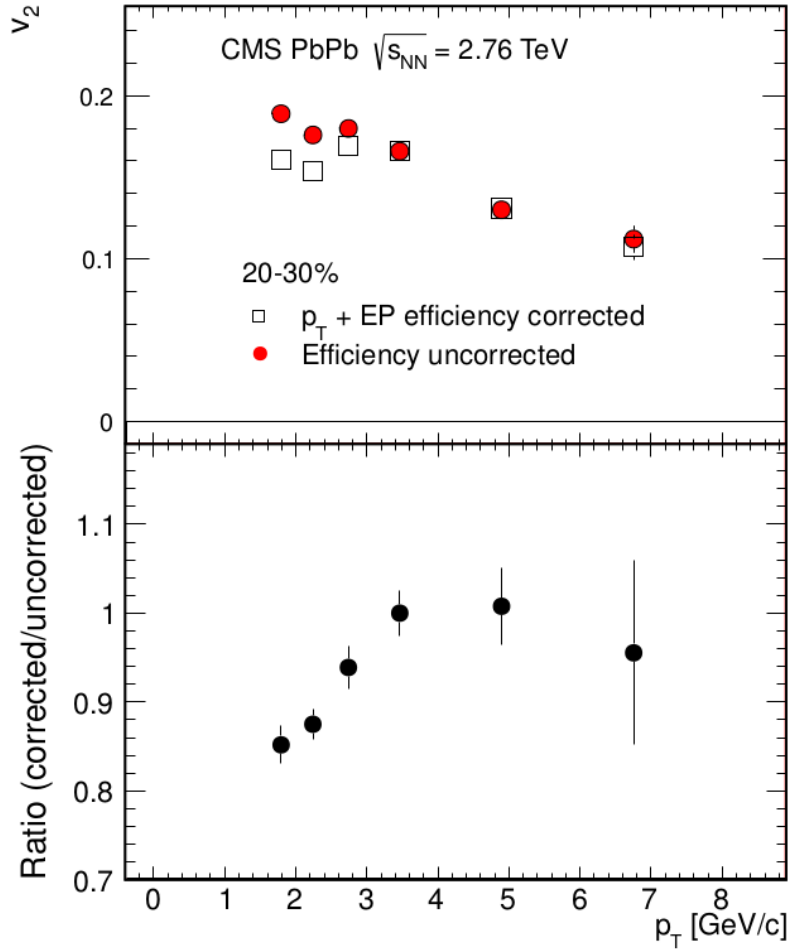


**Figure 5.20:** Top panel: Extracted  $v_2$  values for the CMS PbPb data at  $\sqrt{s_{NN}} = 2.76$  TeV in the 20 – 30% centrality bin. The red points are the values with all efficiency corrections, and the hollow squares are without corrections for efficiency as a function of  $p_T$  and angle with respect to event plane. Bottom panel: Ratio of efficiency-corrected over uncorrected  $v_2$  values.

## 5.4 Event Plane Method

In order to compute the  $v_2$  of neutral pions the standard event-plane method [36] was used, following the same procedure as in the CMS inclusive charged particle measurement. We used standard CMS-HI reconstruction software to produce the event plane on an event-by-event basis. The event plane was taken to be the plane formed by the vector along the beam direction, and the vector pointing in the azimuthal direction of maximum energy deposition in both HF modules averaged together, as given in equation 5.4. This enforced a pseudorapidity gap of at least 2.2 units in  $\eta$  between the region of the EB used for reconstructing  $\pi^0$  mesons and the HF detectors used to measure the event plane, avoiding possible autocorrelations between the event-plane measurement and the  $v_2$  measurement of neutral pions using this event plane.

$$\Psi_{\text{EP}} = \frac{1}{2} \arctan \left( \frac{\sum_{\text{towers}} E_{\text{tower}} \sin(2\phi_{\text{tower}})}{\sum_{\text{towers}} E_{\text{tower}} \cos(2\phi_{\text{tower}})} \right) \quad (5.4)$$

The distribution of event plane angles was flattened with a standard Fourier decomposition to 21st order in order to account for variations in event plane angle acceptance due to detector effects and any other sources of variation. These flattening parameters were calculated for every centrality class and 5-cm z-vertex bin.

The finite segmentation of the detector and finite multiplicity of particles produced in any event mean that the measured event plane will fluctuate around the value of the participant plane as discussed in section 2.2, introducing an error into the  $v_2$  measurement made with the event plane. In order to correct for this, the true  $v_2$  is taken to be the observed value,  $v_2^{\text{obs}}$ , divided by a correction factor  $R$  based on the event-plane resolution.

A sub-event method was employed to find the correction factor for the HF event plane. Subevent A was taken to be the region  $3 < |\eta| < 5$ , with the event plane  $\Psi_A$  determined by the HF as earlier described. Subevent B was taken to be the region  $|\eta| < 0.8$ , with the event plane  $\Psi_B$  determined from charged particle tracks in the silicon tracking system and defined similarly to the HF event plane. Equation 5.5 defines the correction factor as function of the difference between the event plane from these two sub-events, averaged over many events. This was performed independently for each centrality class in the analysis. The correction factors for each centrality are given in table 5.1.

$$R = \langle \cos[2(\Psi_{\text{EP}} - \Psi_r)] \rangle = \sqrt{\langle \cos[2(\Psi_A - \Psi_B)] \rangle} \quad (5.5)$$

Centrality class	Event-Plane Resolution Correction Factor R
20 – 30%	0.914
30 – 40%	0.894
40 – 50%	0.837
50 – 60%	0.729
60 – 70%	0.553
70 – 80%	0.341

**Table 5.1:** Table of the event-plane resolution correction factor values for each centrality class.

In order to calculate the  $v_2^{obs}$ , for every centrality class and  $p_T$  bin we plotted the yield of  $\pi^0$  mesons (after any efficiency corrections) as a function of  $\Delta\Phi$ . We then fit a cosine function to the points as given in equation 5.6, taken from the Fourier decomposition discussed in section 2.2. An example of this cosine fit is shown in Figure 5.21. The value of  $v_2^{obs}$  was taken from the fit parameter. This value was then corrected with the event plane resolution correction factor for the given centrality in order to determine the final  $v_2$  value. The final values are presented in chapter 7.

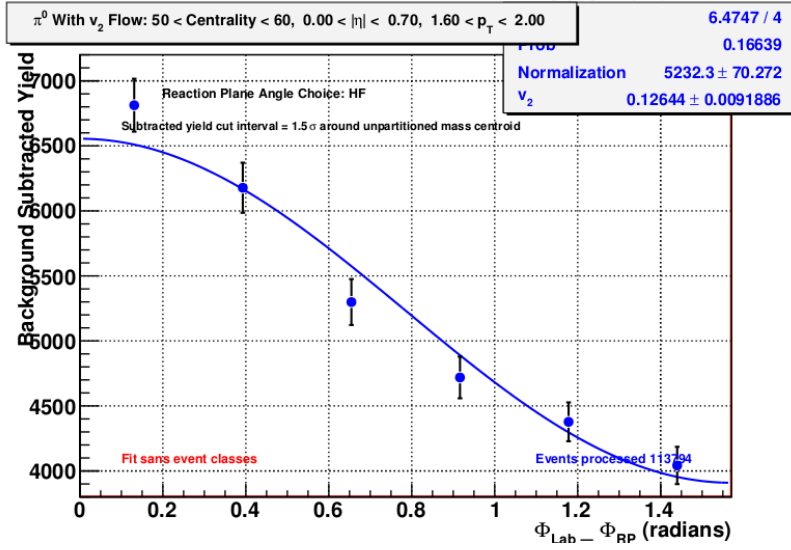


**Figure 5.21:** Reconstructed  $\pi^0$  yields as a function of  $\Delta\Phi$  in the 50 – 60% centrality bin, in the range  $1.6 < p_T < 2.0$  GeV/c. Blue curve shows fit to  $2v_2\cos(2\Delta\Phi)$

$$\frac{dN}{d\Phi} = N_0 (1 + 2v_2\cos[2\Delta\Phi]) \quad (5.6)$$

## Chapter 6

### Systematic Uncertainties

In this analysis, we had several sources of systematic uncertainty in the final measurement. The most significant sources of systematic uncertainty were the S4/S9 ratio and the variation mass integration window. Other significant sources of uncertainty include the  $\gamma\gamma$  opening angle and cluster separation cuts, uncertainties related to the reconstruction efficiency as a function of  $p_T$  and  $\Delta\Phi$ , and the event-plane resolution corrections. Each of these will be discussed in this chapter separately, as well as a summary of other small sources of systematic uncertainty.

#### 6.1 S4/S9 Ratio

The S4/S9 ratio is used as an important selector for photon candidate clusters, as discussed in section 5.1. In order to assess the systematic uncertainty associated with this cut, we performed the analysis with all other parameters held constant but varying the S4/S9 ratio around the reference value of 0.87. For computing the systematic uncertainty we chose an S4/S9 ratio of 0.83 and 0.91 around the value used in the analysis. The mass integration window of  $\pm 2\sigma$  around the mean was kept constant. The largest difference of the final  $v_2$  value for an S4/S9 ratio of either 0.83 or 0.91 was taken as a systematic uncertainty, in each centrality and  $p_T$  bin. The evaluated systematic uncertainties from varying the S4/S9 ratio are given in section 6.6.

#### 6.2 Symmetric and Asymmetric Mass Integration Window

To extract the raw yields of  $\pi^0$  mesons, we used a statistical measurement integrating the counts in the invariant-mass spectrum after background subtraction in a window of  $2\sigma$  around the mean, as discussed in section 5.3. In order to assess the systematic uncertainty associated with the effect of the window size on the measured yield we ran the analysis with the S4/S9 and other cut parameters held at the reference value, but with different integration windows of  $\mu \pm 1.5\sigma$  and  $\mu \pm 3\sigma$ . Figures 6.1 and 6.2 show a set of invariant mass distributions highlighting a window of  $\mu \pm 2\sigma$  and  $\mu \pm 3\sigma$ , respectively. The largest variation of the measured  $v_2$  from the value measured in the standard analysis is taken as a systematic uncertainty.

In addition, we used an asymmetric integration window in order to take into account the effect of conversion correlations on the background-subtracted invariant mass spectrum. The  $p_T$ -dependent opening angle and cluster separation cuts alleviate most of the effects of conversion correlations on the low-mass side of the peak, so an integration window that covers only the low-mass side of the invariant-mass peak was chosen to measure the effect on the extracted yield. The analysis was run with all other parameters held constant but the window of integration was taken to be the intervals  $(\mu - 2\sigma, \mu)$  and  $(\mu - 3\sigma, \mu)$ , with the yield extracted from this asymmetric window doubled

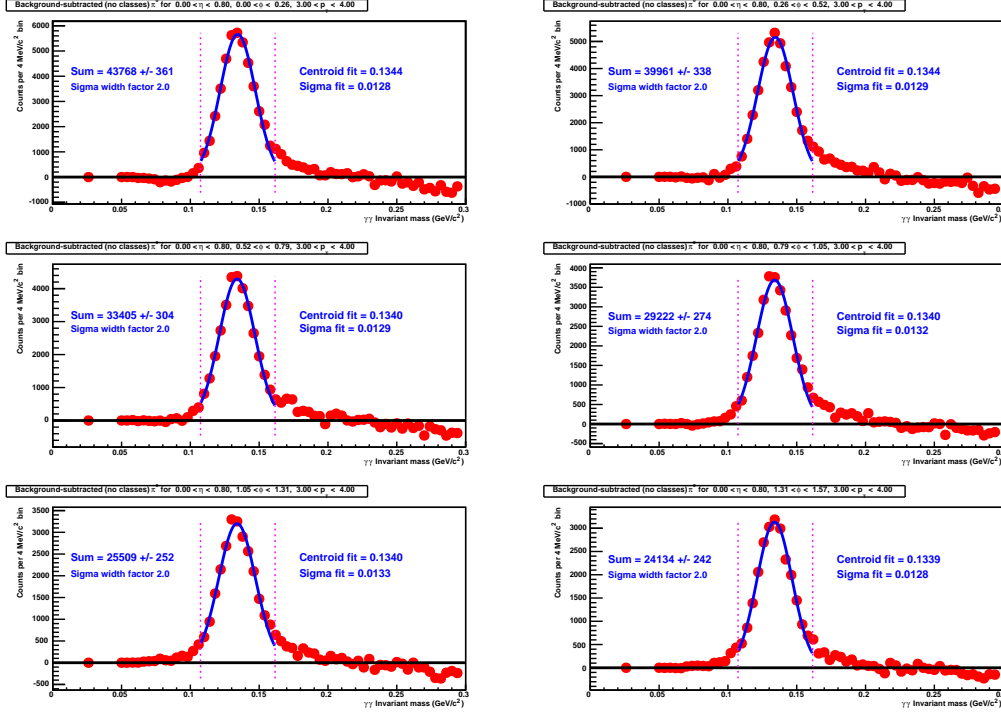


**Figure 6.1:** Background-subtracted invariant mass spectrum based on S4/S9 ratio cuts and standard  $p_T$  dependent opening angle and cluster separation cuts, in 6 bins of angle with respect to the event plane. Taken from CMS PbPb events at  $\sqrt{S_{NN}} = 2.76$  TeV, in the 40 – 50% centrality class, with  $\pi^0$   $p_T$  in the range  $3.0 < p_T < 4.0$  GeV/c . Dotted red line shows mass integration window  $\pm 2\sigma$  around the mean.

to account for taking only the low-mass side of the peak. The largest variation of the measured  $v_2$  value from the value measured in the standard analysis is taken as an additional systematic uncertainty. The evaluated systematic uncertainties from the symmetric and asymmetric mass integration windows are given in section 6.6.

### 6.3 $\pi^0$ Reconstruction Efficiency

The relative efficiency of  $\pi^0$  production as a function of  $p_T$  and angle with respect to the reaction plane is used as a source of systematic uncertainty in each centrality and  $p_T$  bin, regardless of whether these bins were corrected or corrections were found unnecessary. To assess systematic uncertainties related to the efficiency, the analysis was performed without any efficiency corrections, as well as with corrections in all centrality classes and  $p_T$  bins, including bins where corrections were not used in the final result. This evaluation was done separately for both the  $p_T$ -dependent efficiency corrections, and corrections for the efficiency as a function of the angle with respect to the event plane. The difference from the measured  $v_2$  in the final analysis was taken as a systematic uncertainty for the efficiency. The evaluated systematic uncertainties from the  $\pi^0$  reconstruction efficiency are given in section 6.6.

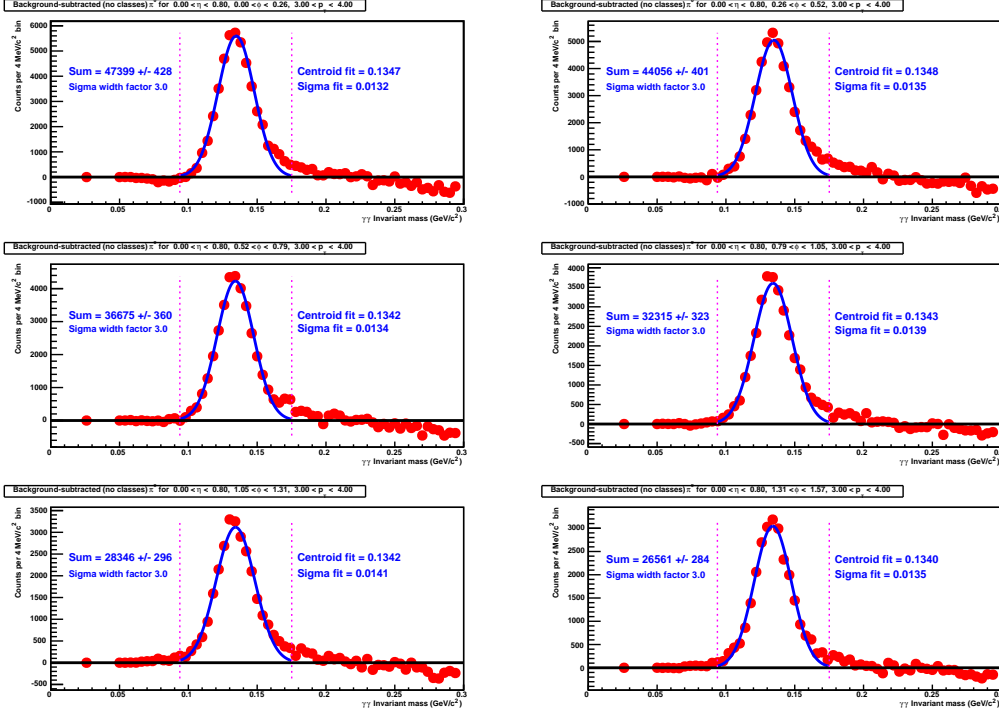


**Figure 6.2:** Background-subtracted invariant mass spectrum based on S4/S9 ratio cuts and standard  $p_T$  dependent opening angle and cluster separation cuts, in 6 bins of angle with respect to the event plane. Taken from CMS PbPb events at  $\sqrt{S_{NN}} = 2.76$  TeV, in the 40 – 50% centrality class, with  $\pi^0$   $p_T$  in the range  $3.0 < p_T < 4.0$  GeV/c . Dotted red line shows mass integration window  $\pm 3\sigma$  around the mean.

## 6.4 Event Plane Method

The event-plane resolution correction factor  $R$  and the event-plane flattening procedure were both considered as possible sources of systematic uncertainty on the final value of  $v_2$ . For the flattening of the event plane, studies performed for the measurement of inclusive charged particle  $v_2$  in CMS [30] determined that the flattening procedure used by CMS introduced a negligible systematic uncertainty. This study introduced a  $15^\circ$  hole in the tracker acceptance using an event plane based on charged particle tracks and found the effect on the flattening of the tracker-based event plane resulted in a systematic change in  $v_2$  of less than 1%. This result was extended to the HF as well. As the event plane method employed for this analysis followed this procedure, we did not include the flattening procedure in the final systematics. For the event-plane resolution correction factor, the statistical uncertainty on the resolution correction factor is used to vary the correction and the  $\pi^0$   $v_2$  and used as a source of systematic uncertainty. The evaluated systematic uncertainties from the event-plane resolution correction factor are given in section 6.6.

## 6.5 Other Sources of Systematic Uncertainty

The  $p_T$ -dependent opening angle and cluster separation cuts are primarily used to control the effects of conversion correlations on the low-mass side of the  $\pi^0$  peak, as discussed in section 5.1. To assess systematic uncertainties related to these cuts, we performed the analysis with all other parameters held constant, but relaxed the cuts from 15% less than the minimum opening angle/cluster separation respectively obtained from Pythia, to a value 30% less than the minimum, by adjusting the parameters of equation 5.2. These two cuts are highly correlated, so we vary both together to assess a single systematic uncertainty for both cuts.

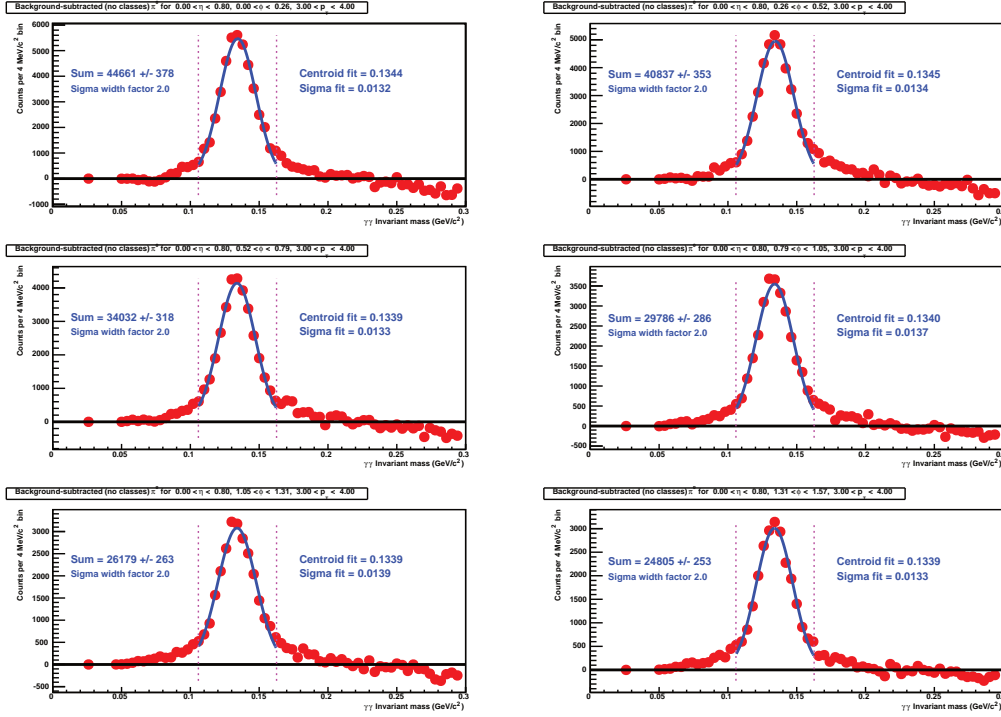


**Figure 6.3:** Background-subtracted invariant mass spectrum based on S4/S9 ratio cuts and modified  $p_T$  dependent opening angle and cluster separation cuts with a value 30% less than the minimum determined from simulations, in 6 bins of angle with respect to the event plane. Taken from CMS PbPb events at  $\sqrt{S_{NN}} = 2.76$  TeV, in the 40 – 50% centrality class, with  $\pi^0$   $p_T$  in the range  $1.6 < p_T < 2.0$  GeV/c .

Figure 6.3 show an example of background subtracted invariant mass plots in the 40 – 50% centrality bin with lowered threshold cut, compare to Figure 5.7. In each bin the difference in extracted  $v_2$  value was found to be negligible within errors, so this cut was not used as a source of systematic uncertainty.

For the trigger efficiency, we ran the analysis with a different centrality definition with the HF energy bin boundaries adjusted for an assumption of 100% efficiency instead of 97%. An example of the variation on the final measurement for one centrality bin is given in Figure 6.4.

The variation in measured  $v_2$  of the  $\pi^0$  mesons was found to be less than 1% in every centrality class

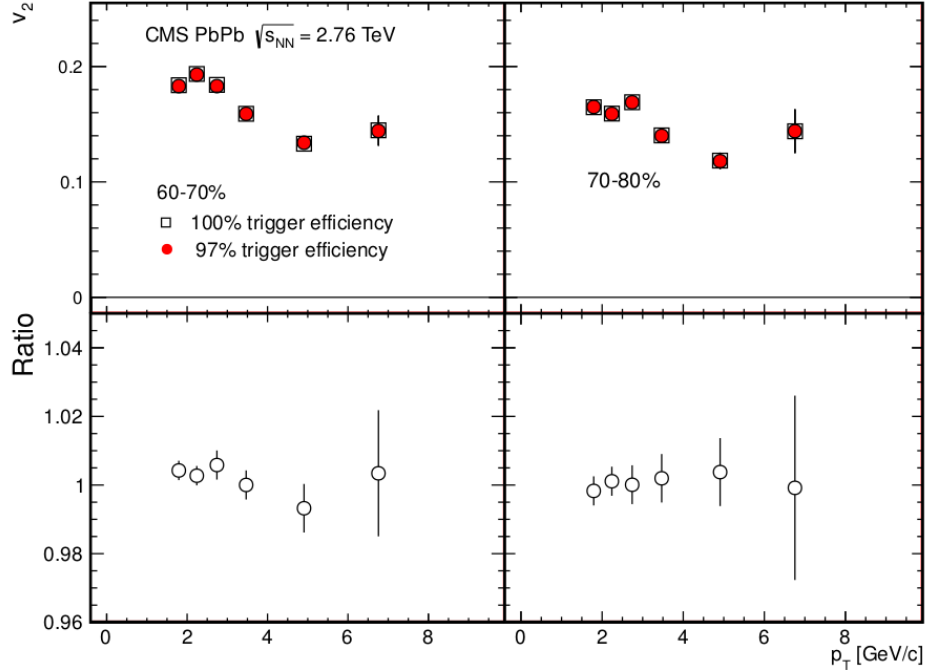


**Figure 6.4:** Top panel: Extracted  $v_2$  values in CMS PbPb at  $\sqrt{s_{NN}} = 2.76$  TeV for the 20 – 30% centrality bin. The red points are the values with the standard centrality definition assuming 97% trigger efficiency, and the hollow squares are with modified centrality bins assuming 100% trigger efficiency. Bottom panel: Ratio of  $v_2$  values assuming 97% efficiency over 100% efficiency.

and  $p_T$  bin, and so this source of systematic uncertainty was not included in the final result.

Similarly, the analysis was performed varying the pseudorapidity window from  $|\eta| < 0.7$  and  $|\eta| < 0.9$ , and separately with the z-vertex acceptance varying from within 10 cm of the center of the detector to within 20 cm of the center. The analysis was also performed with the region of normalization for the mixed-event background and same-event foreground shifted to the intervals  $0.175 < m_{\gamma\gamma} < 0.225$  GeV/ $c^2$  and  $0.225 < m_{\gamma\gamma} < 0.275$  GeV/ $c^2$ . The variation in measured  $v_2$  for the  $\eta$  window, z-vertex cut, and background normalization region were each found to be negligible and were not taken as sources of systematic uncertainty.

## 6.6 Total Systematic Uncertainties

Tables 6.1 through 6.6 give the final systematic uncertainties in each  $p_T$  bin for centrality classes 20 – 30% through 70 – 80%. The contributions to final uncertainties were taken from the S4/S9 ratio, the symmetric and asymmetric mass window variations,  $\pi^0$  correction efficiency as a function of  $p_T$  and  $\Delta\Phi$ , and the event-plane resolution correction factor. Other sources of systematic uncertainty considered were found to be negligible for the total systematic uncertainty. The evaluated uncertainties were added together in quadrature to obtain the final systematic uncertainty in each bin.

$p_T$ Range (GeV/c)	S4/S9 Ratio	Symm. Mass Window	Asymm. Mass Window	$p_T$ - Efficiency	$\Delta\Phi$ - Efficiency	EP Resolution	Total Syst.
1.6 – 2.0	0.007	0.012	0.010	0.000	0.029	0.001	0.034
2.0 – 2.5	0.008	0.008	0.018	0.001	0.022	0.001	0.031
2.5 – 3.0	0.006	0.003	0.018	0.001	0.011	0.001	0.022
3.0 – 4.0	0.016	0.008	0.027	0.001	0.000	0.001	0.033
4.0 – 6.0	0.022	0.010	0.015	0.002	0.000	0.001	0.029
6.0 – 8.0	0.031	0.003	0.007	0.009	0.004	0.001	0.034

**Table 6.1:** Table of systematic uncertainties for  $v_2$  of  $\pi^0$  mesons at 20 – 30% centrality. Column 1 lists the  $p_T$  bin for each row. Columns 2-6 list the evaluated uncertainty for each source in each  $p_T$  bin. Column 7 lists the total systematic uncertainty in each  $p_T$  bin, adding the individual uncertainties in quadrature.

$p_T$ Range (GeV/c)	S4/S9 Ratio	Symm. Mass Window	Asymm. Mass Window	$p_T$ - Efficiency	$\Delta\Phi$ - Efficiency	EP Resolution	Total Syst.
1.6 – 2.0	0.003	0.007	0.003	0.0016	0.012	0.001	0.016
2.0 – 2.5	0.009	0.004	0.008	0.0021	0.009	0.001	0.017
2.5 – 3.0	0.008	0.006	0.018	0.0007	0.009	0.001	0.023
3.0 – 4.0	0.008	0.003	0.021	0.0014	0.008	0.001	0.024
4.0 – 6.0	0.016	0.006	0.015	0.0006	0.008	0.001	0.024
6.0 – 8.0	0.007	0.007	0.011	0.0034	0.008	0.001	0.018

**Table 6.2:** Table of systematic uncertainties for  $v_2$  of  $\pi^0$  mesons at 30 – 40% centrality. Column 1 lists the  $p_T$  bin for each row. Columns 2-6 list the evaluated uncertainty for each source in each  $p_T$  bin. Column 7 lists the total systematic uncertainty in each  $p_T$  bin, adding the individual uncertainties in quadrature.

$p_T$ Range (GeV/c)	S4/S9 Ratio	Symm. Mass Window	Asymm. Mass Window	$p_T$ - Efficiency	$\Delta\Phi$ - Efficiency	EP Resolution	Total Syst.
1.6 – 2.0	0.004	0.005	0.004	0.0006	0.008	0.001	0.012
2.0 – 2.5	0.006	0.005	0.006	0.0004	0.006	0.001	0.013
2.5 – 3.0	0.008	0.000	0.016	0.0007	0.006	0.001	0.020
3.0 – 4.0	0.006	0.001	0.013	0.0006	0.006	0.001	0.017
4.0 – 6.0	0.009	0.000	0.010	0.0006	0.007	0.001	0.016
6.0 – 8.0	0.008	0.006	0.008	0.0015	0.007	0.001	0.016

**Table 6.3:** Table of systematic uncertainties for  $v_2$  of  $\pi^0$  mesons at 40 – 50% centrality. Column 1 lists the  $p_T$  bin for each row. Columns 2-6 list the evaluated uncertainty for each source in each  $p_T$  bin. Column 7 lists the total systematic uncertainty in each  $p_T$  bin, adding the individual uncertainties in quadrature.

$p_T$ Range (GeV/c)	S4/S9 Ratio	Symm. Mass Window	Asymm. Mass Window	$p_T$ - Efficiency	$\Delta\Phi$ - Efficiency	EP Resolution	Total Syst.
1.6 – 2.0	0.003	0.004	0.004	0.0007	0.009	0.002	0.011
2.0 – 2.5	0.004	0.001	0.011	0.0003	0.007	0.002	0.014
2.5 – 3.0	0.003	0.004	0.010	0.0004	0.007	0.002	0.013
3.0 – 4.0	0.007	0.001	0.011	0.0005	0.008	0.001	0.015
4.0 – 6.0	0.011	0.004	0.007	0.0003	0.008	0.001	0.016
6.0 – 8.0	0.018	0.001	0.010	0.0006	0.008	0.001	0.026

**Table 6.4:** Table of systematic uncertainties for  $v_2$  of  $\pi^0$  mesons at 50 – 60% centrality. Column 1 lists the  $p_T$  bin for each row. Columns 2-6 list the evaluated uncertainty for each source in each  $p_T$  bin. Column 7 lists the total systematic uncertainty in each  $p_T$  bin, adding the individual uncertainties in quadrature.

$p_T$ Range (GeV/c)	S4/S9 Ratio	Symm. Mass Window	Asymm. Mass Window	$p_T$ - Efficiency	$\Delta\Phi$ - Efficiency	EP Resolution	Total Syst.
1.6 – 2.0	0.005	0.005	0.003	0.0005	0.007	0.002	0.011
2.0 – 2.5	0.007	0.004	0.006	0.0001	0.007	0.002	0.012
2.5 – 3.0	0.003	0.003	0.009	0.0013	0.007	0.002	0.012
3.0 – 4.0	0.011	0.002	0.001	0.0003	0.007	0.002	0.013
4.0 – 6.0	0.014	0.004	0.013	0.0015	0.007	0.001	0.021
6.0 – 8.0	0.029	0.010	0.035	0.0006	0.007	0.001	0.047

**Table 6.5:** Table of systematic uncertainties for  $v_2$  of  $\pi^0$  mesons at 60 – 70% centrality. Column 1 lists the  $p_T$  bin for each row. Columns 2-6 list the evaluated uncertainty for each source in each  $p_T$  bin. Column 7 lists the total systematic uncertainty in each  $p_T$  bin, adding the individual uncertainties in quadrature.

$p_T$ Range (GeV/c)	S4/S9 Ratio	Symm. Mass Window	Asymm. Mass Window	$p_T$ - Efficiency	$\Delta\Phi$ - Efficiency	EP Resolution	Total Syst.
1.6 – 2.0	0.008	0.001	0.003	0.0001	0.012	0.006	0.016
2.0 – 2.5	0.007	0.005	0.005	0.0000	0.011	0.006	0.016
2.5 – 3.0	0.014	0.002	0.004	0.0000	0.011	0.006	0.019
3.0 – 4.0	0.007	0.004	0.004	0.0000	0.012	0.005	0.016
4.0 – 6.0	0.014	0.004	0.008	0.0000	0.011	0.004	0.021
6.0 – 8.0	0.022	0.033	0.013	0.0000	0.012	0.005	0.044

**Table 6.6:** Table of systematic uncertainties for  $v_2$  of  $\pi^0$  mesons at 70 – 80% centrality. Column 1 lists the  $p_T$  bin for each row. Columns 2-6 list the evaluated uncertainty for each source in each  $p_T$  bin. Column 7 lists the total systematic uncertainty in each  $p_T$  bin, adding the individual uncertainties in quadrature.

## Chapter 7

### Results

Tables 7.1 through 7.6 list data points for the final results of the measurement of the  $v_2$  parameter of identified neutral pions in  $\sqrt{S_{NN}} = 2.76$  TeV PbPb events measured by the CMS experiment. These results are published in Physical Review Letters [62]. Though only published in January of 2013, some interest has already been expressed in these results [27, 71–75]. All corrections for  $p_T$ -dependent efficiency and efficiency as a function of angle with respect to the event plane have been applied, as well as the correction for the event plane resolution. Statistical errors are presented for every point, as well as the total systematic uncertainty as given in chapter 6.

$p_T$ (GeV/c)	Range	Final $\pi^0 v_2$	Statistical Error	Total Systematic Uncertainty
1.6 – 2.0		0.161	0.003	0.034
2.0 – 2.5		0.154	0.002	0.031
2.5 – 3.0		0.169	0.003	0.022
3.0 – 4.0		0.166	0.003	0.033
4.0 – 6.0		0.131	0.004	0.029
6.0 – 8.0		0.107	0.008	0.034

**Table 7.1:** Table of final results for  $\pi^0 v_2$  in 20 – 30% centrality. Column 1 lists the  $p_T$  bin for each row. Column 2 lists the final  $v_2$  values for each bin after corrections for reconstruction efficiency and the event plane resolution. Columns 3 and 4 list the statistical error and systematic uncertainty respectively for each bin.

$p_T$ Range (GeV/c)	Final $\pi^0 v_2$	Statistical Error	Total Systematic Uncertainty
1.6 – 2.0	0.178	0.002	0.016
2.0 – 2.5	0.175	0.002	0.017
2.5 – 3.0	0.192	0.003	0.023
3.0 – 4.0	0.180	0.003	0.024
4.0 – 6.0	0.137	0.004	0.024
6.0 – 8.0	0.118	0.009	0.018

**Table 7.2:** Table of final results for  $\pi^0 v_2$  in 30 – 40% centrality. Column 1 lists the  $p_T$  bin for each row. Column 2 lists the final  $v_2$  values for each bin after corrections for reconstruction efficiency and the event plane resolution. Columns 3 and 4 list the statistical error and systematic uncertainty respectively for each bin.

$p_T$ Range (GeV/c)	Final $\pi^0 v_2$	Statistical Error	Total Systematic Uncertainty
1.6 – 2.0	0.192	0.002	0.012
2.0 – 2.5	0.189	0.002	0.013
2.5 – 3.0	0.194	0.003	0.020
3.0 – 4.0	0.182	0.003	0.017
4.0 – 6.0	0.153	0.004	0.016
6.0 – 8.0	0.108	0.010	0.016

**Table 7.3:** Table of final results for  $\pi^0 v_2$  in 50 – 50% centrality. Column 1 lists the  $p_T$  bin for each row. Column 2 lists the final  $v_2$  values for each bin after corrections for reconstruction efficiency and the event plane resolution. Columns 3 and 4 list the statistical error and systematic uncertainty respectively for each bin.

$p_T$ Range (GeV/c)	Final $\pi^0 v_2$	Statistical Error	Total Systematic Uncertainty
1.6 – 2.0	0.188	0.003	0.011
2.0 – 2.5	0.183	0.003	0.014
2.5 – 3.0	0.180	0.004	0.013
3.0 – 4.0	0.183	0.004	0.015
4.0 – 6.0	0.142	0.006	0.016
6.0 – 8.0	0.102	0.016	0.026

**Table 7.4:** Table of final results for  $\pi^0 v_2$  in 50 – 60% centrality. Column 1 lists the  $p_T$  bin for each row. Column 2 lists the final  $v_2$  values for each bin after corrections for reconstruction efficiency and the event plane resolution. Columns 3 and 4 list the statistical error and systematic uncertainty respectively for each bin.

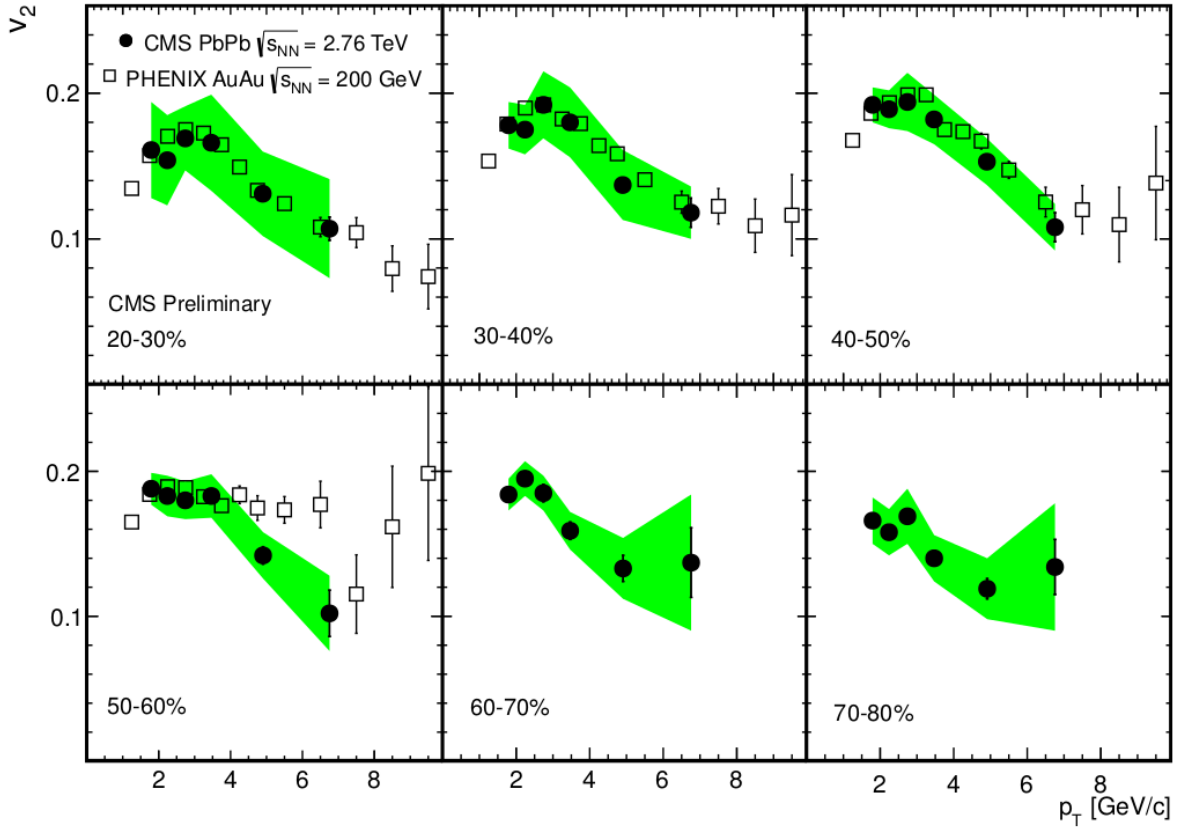
$p_T$ Range (GeV/c)	Final $\pi^0 v_2$	Statistical Error	Total Systematic Uncertainty
1.6 – 2.0	0.184	0.004	0.011
2.0 – 2.5	0.195	0.004	0.012
2.5 – 3.0	0.185	0.006	0.012
3.0 – 4.0	0.159	0.006	0.013
4.0 – 6.0	0.133	0.009	0.021
6.0 – 8.0	0.137	0.024	0.047

**Table 7.5:** Table of final results for  $\pi^0 v_2$  in 60 – 70% centrality. Column 1 lists the  $p_T$  bin for each row. Column 2 lists the final  $v_2$  values for each bin after corrections for reconstruction efficiency and the event plane resolution. Columns 3 and 4 list the statistical error and systematic uncertainty respectively for each bin.

$p_T$ (GeV/c)	Range	Final $\pi^0 v_2$	Statistical Error	Total Systematic Uncertainty
1.6 – 2.0		0.166	0.008	0.016
2.0 – 2.5		0.158	0.009	0.016
2.5 – 3.0		0.169	0.012	0.019
3.0 – 4.0		0.140	0.014	0.016
4.0 – 6.0		0.119	0.021	0.021
6.0 – 8.0		0.134	0.059	0.044

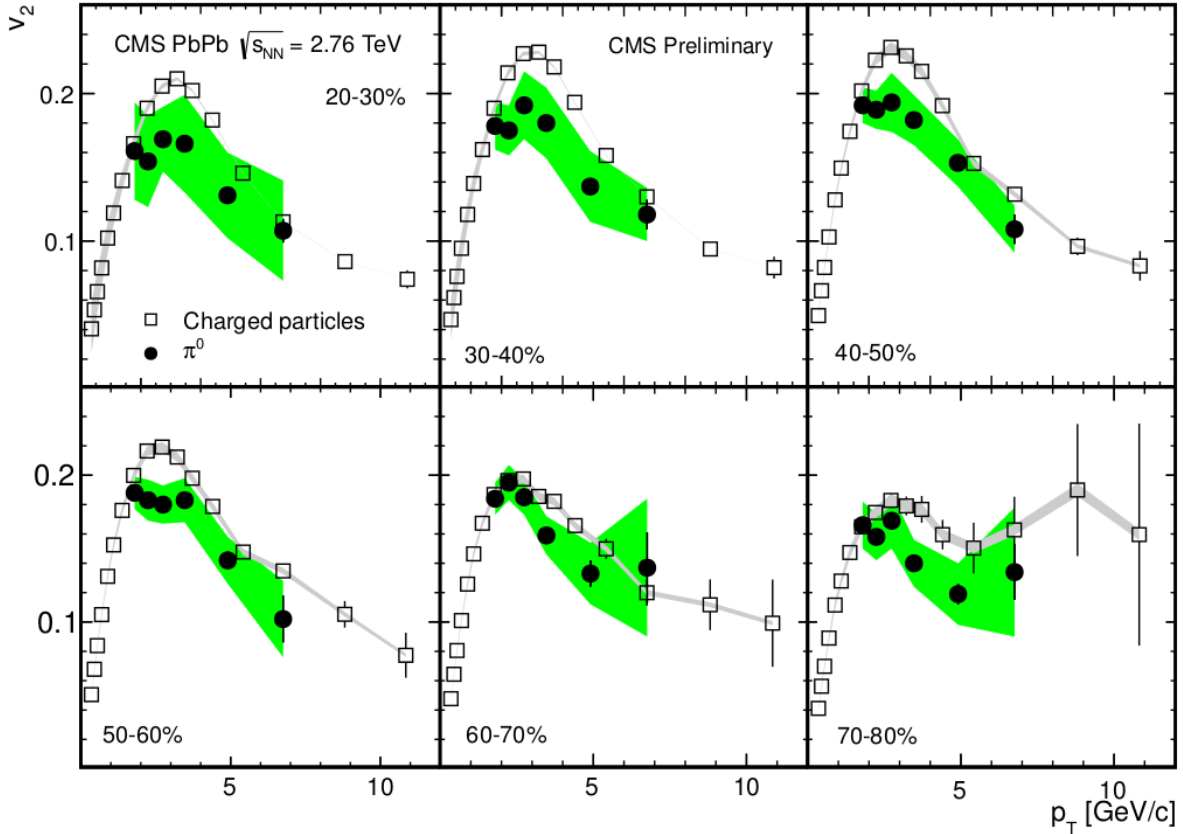
**Table 7.6:** Table of final results for  $\pi^0 v_2$  in 70 – 80% centrality. Column 1 lists the  $p_T$  bin for each row. Column 2 lists the final  $v_2$  values for each bin after corrections for reconstruction efficiency and the event plane resolution. Columns 3 and 4 list the statistical error and systematic uncertainty respectively for each bin.

The most informative presentation of this data is in comparison with other particle species and other collision systems. Figure 7.1 shows a comparison of the  $v_2$  of  $\pi^0$  mesons as a function of  $p_T$  as measured in this analysis at the CMS experiment in PbPb collisions at  $\sqrt{S_{NN}} = 2.76$  TeV with  $\pi^0$  mesons measured by the PHENIX experiment in gold-gold (AuAu) collisions at  $\sqrt{S_{NN}} = 200$  GeV [48]. There are no PHENIX measurements for  $\pi^0$  mesons in the 60 – 70% and 70 – 80% centrality bins. In 20 – 30% centrality through 40 – 50% the CMS and PHENIX points overlap almost completely, and in the 50 – 60% centrality bin these points only diverge from 4 to 8 GeV/c in  $p_T$ , though no systematic uncertainties are available for the PHENIX points. The agreement in the  $v_2$  values is despite an increase in the center of mass energy by nearly an order of magnitude.



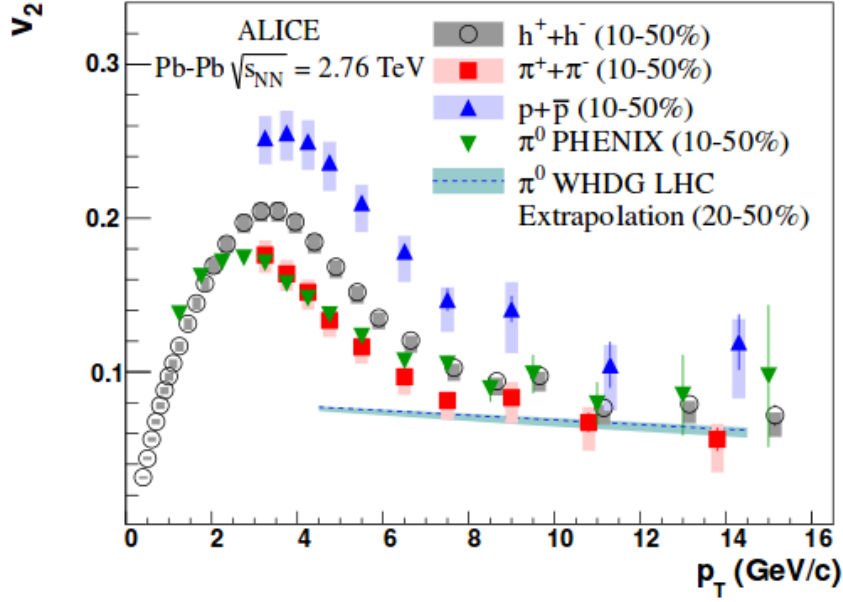
**Figure 7.1:** A comparison of the  $v_2$  of  $\pi^0$  mesons in  $\sqrt{s_{NN}} = 2.76$  TeV PbPb measured by CMS and in  $\sqrt{s_{NN}} = 200$  GeV AuAu measured by PHENIX [48]. The green shaded band shows systematic uncertainties for  $\pi^0$   $v_2$  in CMS. Only statistical errors were plotted for the PHENIX measurement.

Figure 7.2 shows a comparison of the  $v_2$  of identified neutral pions as we measured at the CMS experiment with that of inclusive charged particles also measured at the CMS experiment [30], with both measurements in PbPb collisions at  $\sqrt{S_{NN}} = 2.76$  TeV. Both measurements use the same centrality bins and pseudorapidity window. In the most central collisions we see a systematic difference between neutral pions and inclusive charged particles between 2 to 7 GeV/c in  $p_T$ , at which point the difference disappears. This difference begins to disappear in the peripheral 60–70% and 70–80% centrality bins.



**Figure 7.2:** A comparison of the  $v_2$  of  $\pi^0$  mesons with that of inclusive charged particles in  $\sqrt{S_{NN}} = 2.76$  TeV PbPb measured by CMS [30]. The green shaded band shows systematic uncertainties for  $\pi^0$  mesons, and the grey shaded band shows systematic uncertainties for inclusive charged particles.

The particle species composition of charged particles [76] in PbPb collisions at  $\sqrt{S_{NN}} = 2.76$  TeV indicate that the  $v_2$  of baryons are a large component of the  $v_2$  of inclusive charged particles. This suggests the systematic difference we observe between neutral pions and inclusive charged particles is indicative of the baryon-meson anomaly as discussed in section 2.3. The pattern seen here is very similar to that observed at RHIC energies, suggesting that the recombination mechanism is still the dominant hadronization mechanism at intermediate  $p_T$ . This is similar to the results from measurements of the  $v_2$  of identified hadrons in PbPb collisions at the LHC measured by the ALICE experiment [77], seen in Figure 7.3.



**Figure 7.3:** The  $v_2$  of identified charged pions, protons, and inclusive charged hadrons from the ALICE experiment [77], and neutral pions from the PHENIX experiment [48], as a function of  $p_T$  between 10 – 50% in centrality. The dashed line comes from WHDG model calculations for neutral pions [78].

In addition to the quark coalescence picture, azimuthal anisotropy at high  $p_T$  can provide some information about energy loss mechanisms in the strongly coupled medium produced in PbPb collisions at the LHC. Energy loss calculations from Gyulassy and Horowitz [78] give a  $v_2$  for neutral pions at LHC energies that is in agreement with the measurements presented in this dissertation in the 6 – 8 GeV/c  $p_T$  bin. While the CMS  $\pi^0$  results only extend to 8 GeV/c in  $p_T$ , we see in the comparison with inclusive charged hadrons that they are in agreement in the highest  $p_T$  bin which suggests that in this regime jet fragmentation is the dominant hadronization mechanism for neutral pions. It is not possible to claim confirmation of these energy loss calculations with this CMS  $\pi^0$  measurement but it is possible that future results based on this measurement could provide a stronger claim. Some currently ongoing and possible future studies following from this analysis will be discussed in the next chapter.

## Chapter 8

### Summary and Outlook

This analysis is the first result of the  $\pi^0$  physics program for heavy ions in CMS at Vanderbilt University. With the expertise developed in this analysis, future studies will be able to probe further into the nature of the quark-gluon plasma. Preliminary analysis is underway on  $\pi^0$ -hadron correlations in pPb events recorded by CMS in early 2013, with the current intention of publishing the results in time for the Quark Matter 2014 conference. The  $p_T$  reach of  $\pi^0$  measurements at the CMS detector could be extended by taking advantage of the photon conversions to reconstruct  $\pi^0$  mesons in the  $\pi^0 \rightarrow \gamma e^+ e^-$  decay channel, which will mitigate the effect of cluster overlap in the ECAL. This technique will be tested first in pPb data which has lower occupancy, and then extended to PbPb for future studies. The three-body channel has already been tested in CMS pp data, and the four-body decay channel ( $\pi^0 \rightarrow e^+ e^- e^+ e^-$ ) has been used by ALICE to extend the coverage of their  $\pi^0$  measurements [79].

The techniques used in this analysis can also be extended to studies in the  $\gamma\gamma$  channel using the  $\eta^0$  meson, which can extend the  $p_T$  reach of a such an analysis due to the greater invariant mass of the  $\eta^0$  causing cluster merging to occur at a higher  $p_T$ . A proof-of-concept preliminary invariant mass spectrum showing a peak at the mass of the  $\eta^0$  meson can be seen in figure 8.1. Dr. Monika Sharma and graduate student Ravi Kishore Janjam will be continuing this work with the Vanderbilt heavy ion group. With the remarkable performance of the CMS detector and improvements to the LHC set to come online in 2015, the potential for a physics program based on neutral pions is extraordinary.

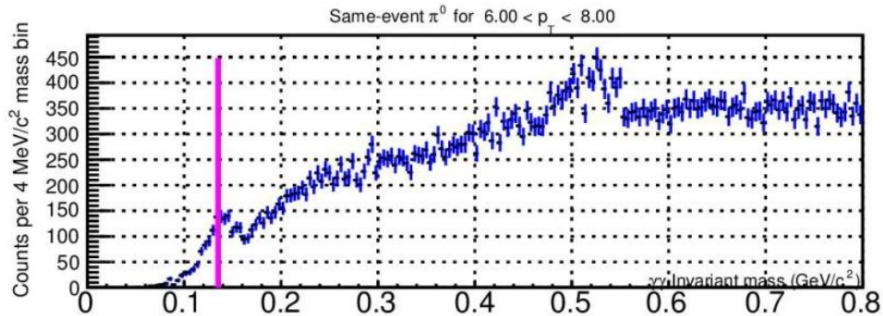


**Figure 8.1:** A preliminary  $\gamma\gamma$  invariant mass spectrum in the 6 – 8 GeV/c  $p_T$  bin from CMS pPb data taken in 2013 showing a peak in the  $\eta^0$  mass region around 545 MeV/c<sup>2</sup>. The solid magenta line indicates the nominal mass of the  $\pi^0$  meson, situated at the prominent  $\pi^0$  mass peak. No selection cuts beyond the S4/S9 ratio have been applied.

In conclusion, we have presented a measurement of the azimuthal anisotropy parameter  $v_2$  for identified neutral pions in PbPb collisions at a center of mass energy per nucleon  $\sqrt{S_{NN}} = 2.76$  TeV, in the pseudorapidity range  $|\eta| < 0.8$ , for a transverse momentum between 1.6 and 8 GeV/c. We have compared this with the  $v_2$  of neutral pions measured by the PHENIX experiment in

AuAu collisions at  $\sqrt{S_{NN}} = 200$  GeV, and observed a nearly identical magnitude of  $v_2$ . We have also compared with inclusive charged hadrons measured by CMS in the same collision system and energy and observed a systematically lower value of  $v_2$  for  $\pi^0$  mesons between 2 to 7 GeV/c in  $p_T$ . We conclude that this confirms the recombination mechanism is the dominant hadronization mechanism at intermediate  $p_T$  for PbPb collisions at LHC energies. This result gives us further insight into the nature of the strongly-interacting quark gluon plasma produced in heavy-ion collisions, and paves the way for a continuing  $\pi^0$  physics program in heavy ions at Vanderbilt University.

## Appendix A

### Conversion Correlations

In order to extract the yield of produced  $\pi^0$  mesons, we have employed in this analysis a mixed-event background subtraction technique. The strength of this method is that it is data-driven, unlike a fit to a parametrized background. The unavoidable deficiency of this technique is its inability to remove unwanted correlations that occur in the same-event foreground. To some degree this must be true as the  $\pi^0$  peak in the  $m_{\gamma\gamma}$  invariant mass spectrum is itself the result of correlations between the decay photons, and we cannot know a-priori the source of correlation between any two photons. Therefore it is necessary to understand the source of any unwanted correlations so we can understand their effect on the invariant mass spectrum. This will allow us to account for any error introduced in the extracted yield, and possibly allow for mitigation strategies to filter out the unwanted correlations.

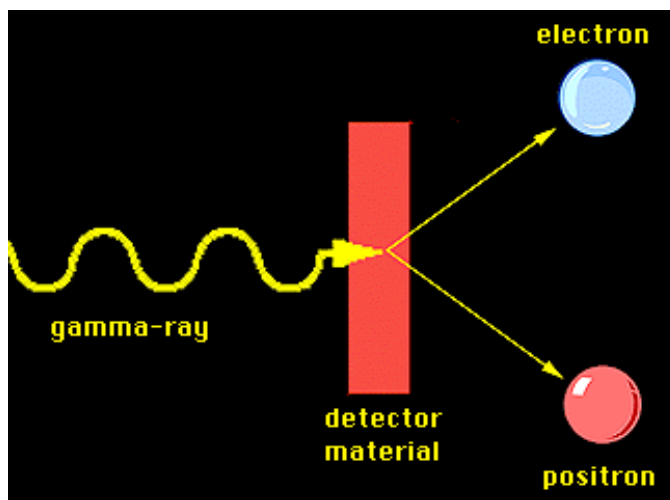


**Figure A.1:** A cartoon showing the process of a high-energy photon producing an  $e^+e^-$  pair through interaction with a layer of the silicon strip detector.

The most prominent source of same-event correlations identified in this analysis was found to come from photon conversions. As photons pass through the CMS silicon strip tracker they have a chance to interact with the silicon nuclei and convert into  $e^+e^-$  pairs, as illustrated in Figure A.1. If the photon has enough energy, one or both of these conversion electrons/positrons may have enough  $p_T$  to reach the ECAL barrel and initiate a shower in the lead tungstate crystals. The resulting clusters of rechits can sometimes pass selection cuts and be mis-identified as photon candidates. We determined from single  $\pi^0$  particle gun simulations that a photon has a roughly 25% chance of converting in the CMS silicon tracker within the  $|\eta| < 0.8$  window used in this analysis. This leads to a large fraction of produced  $\pi^0$  mesons having one or both decay photons convert.

When two clusters are selected to compute the diphoton mass, there are several possibilities. They could come from uncorrelated sources, in which case they will contribute to the normal combinatoric

background. They could come from decay photons of the same  $\pi^0$  parent, in which case they will add to the normal  $\pi^0$  mass peak. Or one cluster could be the result of an unconverted decay photon and the other a conversion electron from the other decay photon from the same  $\pi^0$ , in which case the reconstructed  $\pi^0$  will be distorted from the true parent. This can also occur when both clusters are the result of conversion electrons. We will concentrate on the case where one or both clusters result from photon conversions.

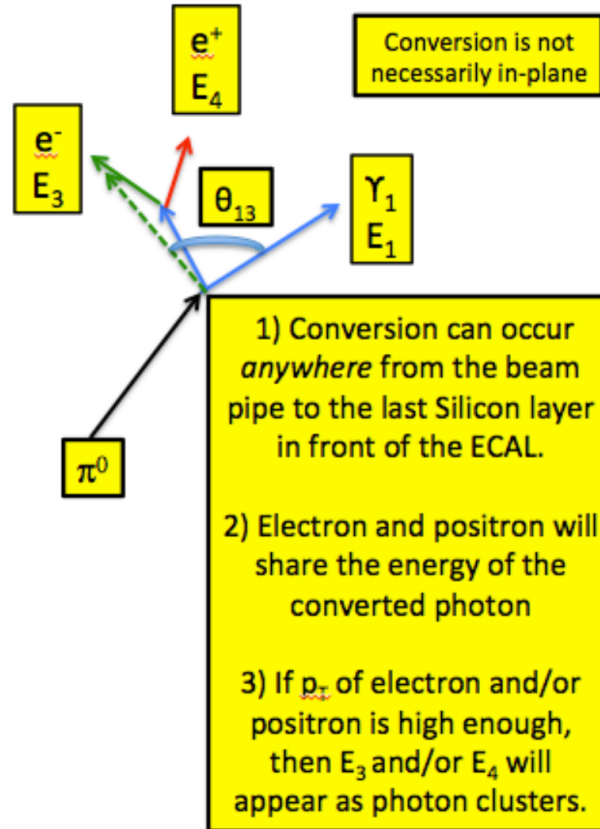


**Figure A.2:** A diagram of a possible photon conversion scenario.

Figure A.2 shows a diagram illustrating the case where one decay photon converts into an electron-positron pair and the other remains unconverted. By equation 5.1, we see that the effect on the reconstructed mass will depend on the total energy  $E$  of the conversion electron cluster, and the calculated opening angle between it and the cluster from the unconverted photon. Depending on the relative orientation of the unconverted photon and the converted photon, the sign of the charge of the conversion electron/positron, and the transverse momentum of the particle, the opening angle can vary widely. If the opening angle is very large, it can lead to a much higher reconstructed mass than the parent  $\pi^0$ . Conversely if the opening angle is small, it can lead to a lower reconstructed mass. This will lead to a very broad structure underlying the true  $\pi^0$  mass peak, as we saw from simulation studies and shown in Figure 5.9.

With a mixed-event background subtraction technique, the excess at high mass can lead to several effects. Since a normalization region must be chosen to scale the mixed-event background to the

same-event foreground, the presence of a broad conversion correlation structure on the high-mass side will lead to an oversubtraction in a higher mass region of the invariant mass spectrum, and an undersubtraction on the lower-mass side. As shown in section 5.1 of this dissertation the low-mass structures can be cleaned up by the use of cuts on the opening angle and cluster separation, but these cuts will not affect the extended structure on the high-mass side.

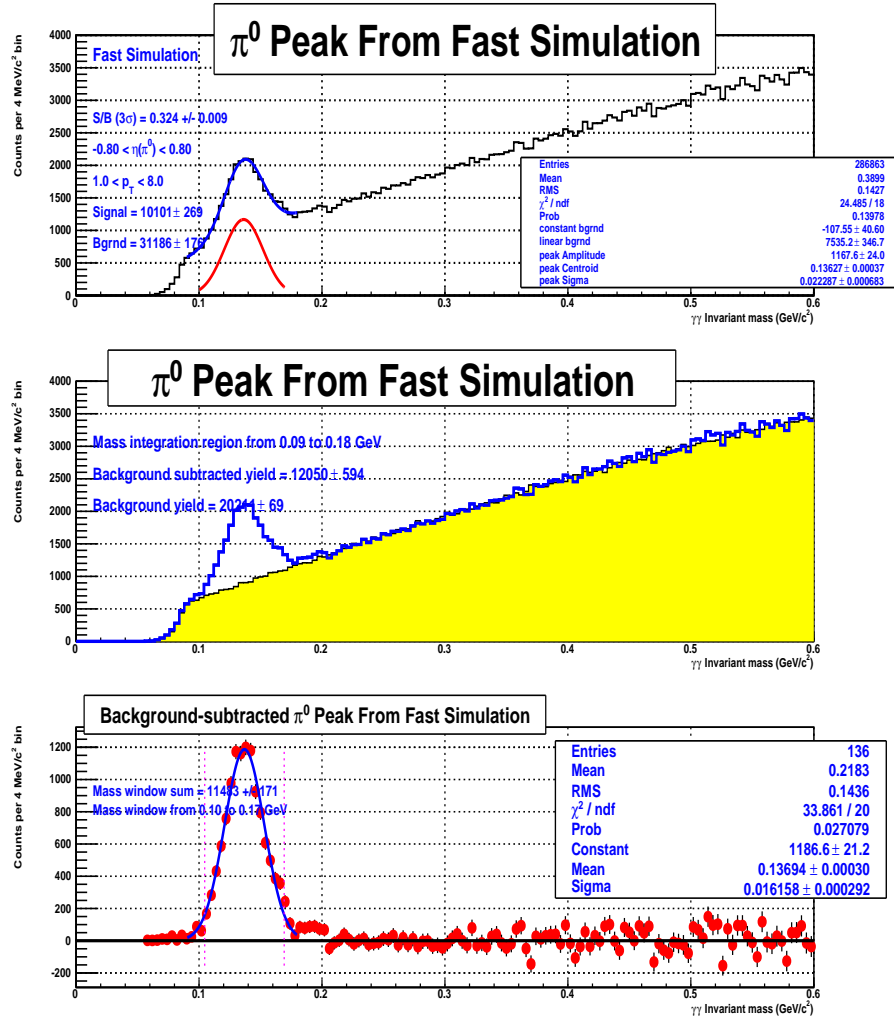


**Figure A.3:** Top Panel: Same-event foreground from  $\pi^0$  particle gun simulations with no photon conversions, with a parametric fit to the background and peak. Middle panel: Same-event foreground and mixed-event background from the same simulation. Bottom panel: Background-subtracted invariant mass from same simulation, with no oversubtraction visible.

Figures A.3 and A.4 show an invariant mass spectrum calculated from  $\pi^0$  particle gun simulations without conversions allowed in the tracker and with conversions turned on, respectively. Figure A.4 shows the same qualitative feature of oversubtraction in the high mass region as is seen in both HYDJET simulations and real PbPb data. Figures A.5 and A.6 show the extracted  $v_2$  from a set of particle-gun simulations with an induced  $v_2$  azimuthal anisotropy, both with and without

conversion effects turned on. There is little observed difference, suggesting that the systematic effect on measured  $v_2$  from conversion correlations is small. Despite this however strategies for mitigating these effects have been considered.

Ideally, we would like to be able to tag the clusters resulting from conversion electrons and reject them as photon candidates. The default tracking algorithms in CMS designed for the relatively low multiplicity of pp collisions can sometime identify photon conversion by tagging the displaced vertex of the electron-positron pair. The tracking algorithms developed for the high-multiplicity HI environment however cannot reconstruct tracks with a displaced vertex as of the time of this writing, so they will not be identified. This makes the identification of conversion electrons in CMS PbPb data difficult at best.

In the January 2013 pPb data taking period, CMS was able to use standard pp tracking for reconstruction. This opens up the possibility of using the native conversion detection tools in order to tag the tracks of conversion electrons, and then match ECAL clusters with the identified conversion electron tracks and filter them out. Another possibility is the implementation of a cluster-seeded tracking algorithm that reconstructs tracks in an outside-in fashion, using clusters in the ECAL as a starting point and working in layer by layer. We have not studied this technique in depth, but any future analysis of  $\pi^0$  mesons in CMS PbPb data may benefit from such a technique.

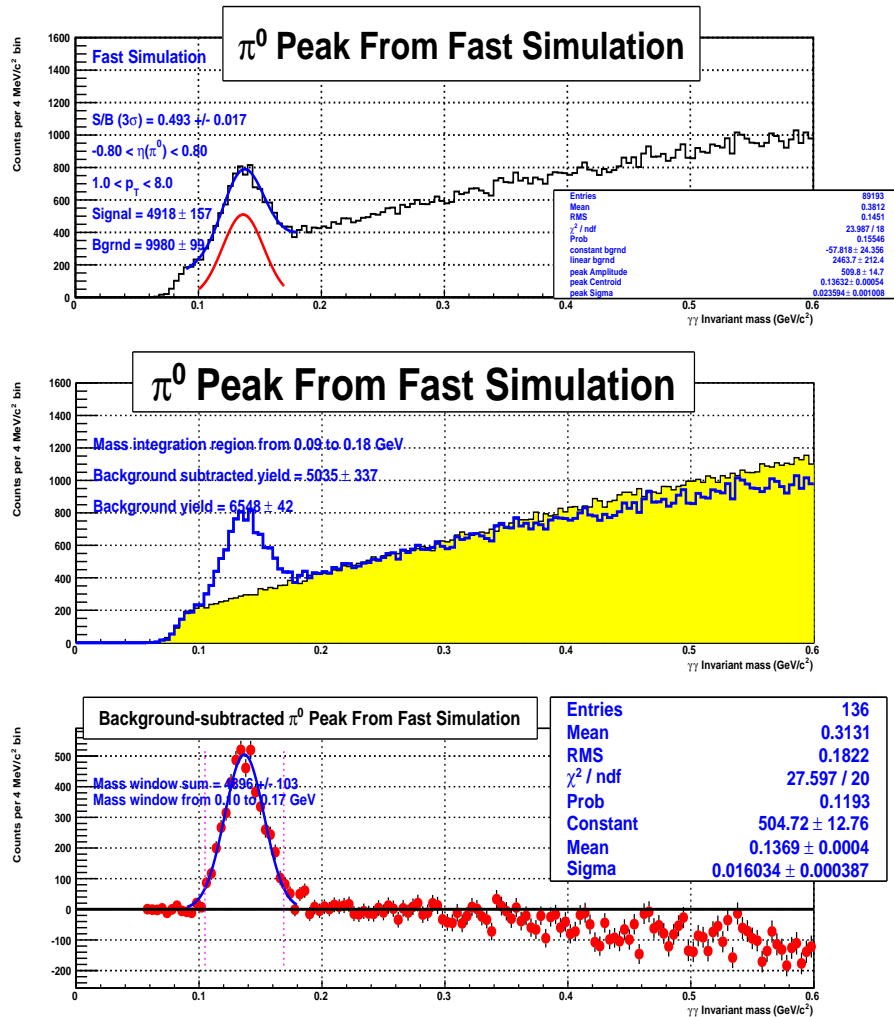


**Figure A.4:** Top Panel: Same-event foreground from  $\pi^0$  particle gun simulations with photon conversions allowed, with a parametric fit to the background and peak. Middle panel: Same-event foreground and mixed-event background from the same simulation. Bottom panel: Background-subtracted invariant mass from same simulation, with oversubtraction apparent on the high mass side.

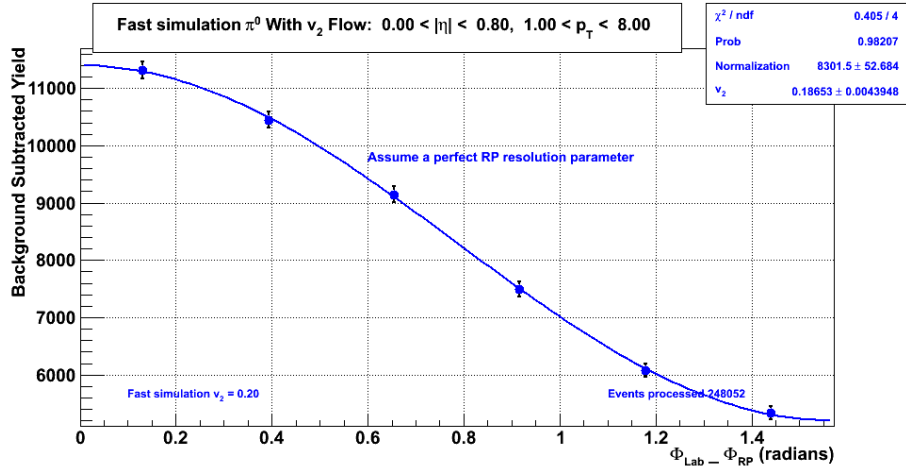


**Figure A.5:** Cosine fit to  $\pi^0$  yield from particle gun simulations with an induced  $v_2$  parameter and no photon conversions.

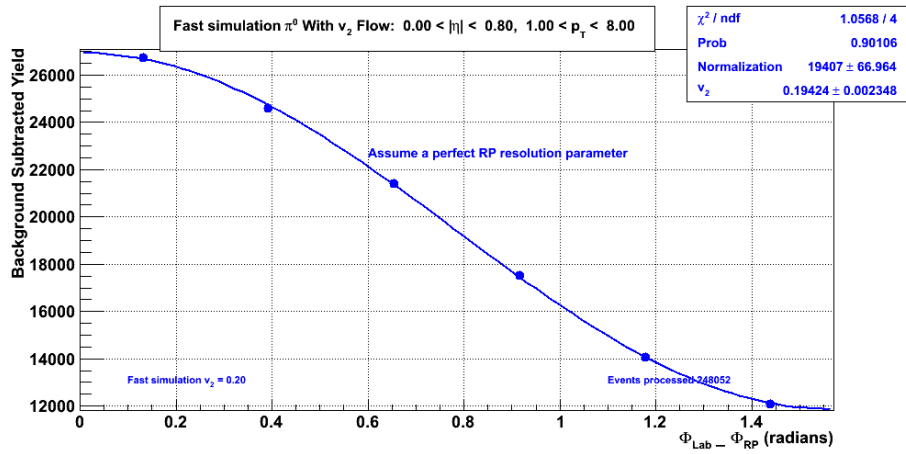


**Figure A.6:** Cosine fit to  $\pi^0$  yield from particle gun simulations with an induced  $v_2$  parameter and photon conversions allowed. Most importantly, there is no significant difference in the  $v_2$  fit parameter versus the no-conversion case.

## Appendix B

### CMS Computing

The CMS computing model [80] has been a major factor in the success of this analysis. It allows for a fast and efficient workflow starting with the processing of raw data at the CERN computer farms straight to the detector all the way to analysis of the processed data by researchers at local computing centers. This appendix will give a brief description of the computing model and its benefits to analyzers.

The CMS computing model begins with the trigger systems that decide which events to record and which to discard, as described in section 4.1. Events that pass the trigger systems are sent directly from the CMS detector itself at Point 5 to the Tier 0 computing farm located at the primary CERN campus in Meyrin. There the streamer files that come from the detector are repacked into RAW format consisting of the readout state of individual detector components. Events tagged by the HLT are sorted into different Primary Datasets that are defined by the analyzer-specified trigger paths. Data in the RAW format is then processed by the Tier 0 farm for an initial Prompt Reconstruction. The output files are in a RECO format that contains reconstructed physics objects such as jets, tracks, muons, etc., as well as fine-grained detector information such as rechits to allow for more in-depth and customized analysis procedures. All RAW and RECO data is archived on tape at the Tier 0 for data preservation purposes. The author of this dissertation participated in this effort as a Tier 0 operator and computing liaison for the CMS Heavy Ion PAG during the 2011 PbPb data taking.

Once RECO files are produced at the Tier 0, they are transferred along with the accompanying RAW source files to one of nine regional Tier 1 centers for secondary archival purposes and any further processing that analyzers request. The nine Tier 1 facilities are located at the Fermilab National Laboratory (FNAL) in the US, Rutherford Appleton Laboratory (RAL) in the UK, the National Institute of Nuclear Physics and Particle Physics in France (IN2P3), the Puerto de Informacion Cientifica (PIC) in Spain, the Karlsruhe Institute of Technology (KIT) in Germany, the National Institute of Nuclear Physics (CNAF) in Italy, the Joint Institute for Nuclear Research (JINR) in Russia, the Academia Sinica Grid Computing (ASGC) in Taiwan, and a central Tier 1 facility at CERN. These Tier 1 facilities are responsible for producing skim datasets containing a subset of interesting events for analyzers, performing re-reconstruction of RAW data with new software and calibrations, and producing Monte Carlo simulations. Typically researchers do not perform analysis tasks directly at Tier 1 sites.

Every Tier 1 facility is linked to a number of Tier 2 computing centers based on their regional proximity and national affiliation. Tier 2 sites can subscribe to data from Tier 1 centers such as full or partial RECO datasets, skims produced on RECO data, or MC data produced at the Tier 1 sites. Data at Tier 2 sites can be directly accessed by local analyzers, or made available to analyzers around the world via grid computing protocols. In addition to user analysis, a portion of a Tier 2 site's computing power is made available for MC production tasks similarly to the Tier 1 sites.

There are also Tier 3 sites that may be hosted in the same location as other Tier 1 and Tier 2 sites or independent, and can subscribe to data from Tier 1 or Tier 2 sites. Tier 3 sites are typically dedicated solely to data analysis by local or regionally-affiliated researchers.

The Tier 2 site at Vanderbilt University is in some ways a special case. The Vanderbilt Tier 2 is a dedicated site for the CMS Heavy Ions program, and shares some responsibilities that would ordinarily fall to Tier 1 facilities. Specifically, the Vanderbilt Tier 2 is responsible for performing re-reconstruction of CMS heavy ion data and other computing-intensive tasks for the CMS-HI community. The Tier 2 center at MIT also has a significant portion dedicated to CMS Heavy Ions, and is primarily tasked with the production of Monte Carlo simulations for CMS-HI. Other Tier 2 sites with a significant HI presence include GRIF in France, SPRACE in Brazil, and SINP in Russia.

The method that CMS uses to connect the many computing resources available through various Tier sites is grid computing. Large data transfers between sites are performed through a system called PhEDEx, Physics Experiment Data Export. The DAS (Data Aggregation Service) is used to catalog datasets and allow researchers to find datasets of interest. Production jobs (reconstruction, re-reconstruction, central Monte Carlo simulations, etc) are managed through a system called WMAgent, which directs jobs to Tier 1 and Tier 2 sites where the necessary input data is resident and CPU resources are available. Individual user analysis is performed through a system called CRAB (CMS Remote Analysis Builder), which directs user analysis jobs to available Tier 2 sites that host the dataset the user is interested in. There are some facilities that support large analysis jobs by local users directly, but the predominate computing model in CMS for individual analyzers is through the grid with CRAB.

For this analysis, analysis was primarily performed at the Vanderbilt Tier 2 computing center. Significant involvement from the MIT Tier 2 for the production of Monte Carlo simulations and the Tier 0 at CERN for the primary data reconstruction were also critical for the success of this analysis.

## Bibliography

- [1] Murray Gell-Mann. A Schematic Model of Baryons and Mesons. *Phys. Lett.*, 8:214–215, 1964.
- [2] Tadao Nakano and Kazuhiko Nishijima. Charge independence for  $v$ -particles. *Progress of Theoretical Physics*, 10(5):581–582, 1953.
- [3] A. Bodek, M. Breidenbach, D. L. Dubin, J. E. Elias, J. I. Friedman, H. W. Kendall, J. S. Poucher, E. M. Riordan, M. R. Sogard, D. H. Coward, and D. J. Sherden. Experimental studies of the neutron and proton electromagnetic structure functions. *Phys. Rev. D*, 20(7):1471–1552, Oct 1979.
- [4] G. F. Chapline, M. H. Johnson, E. Teller, and M. S. Weiss. Highly excited nuclear matter. *Phys. Rev. D*, 8(12):4302–4308, Dec 1973.
- [5] Edward V. Shuryak. *The QCD Vacuum, Hadrons, and Superdense Matter*. World Scientific Publishing Company, 5 Toh Tuck Link, Singapore 596224, second edition, 2010.
- [6] David J. Gross and Frank Wilczek. Ultraviolet behavior of non-abelian gauge theories. *Phys. Rev. Lett.*, 30:1343–1346, Jun 1973.
- [7] Kenneth G. Wilson. Confinement of quarks. *Phys. Rev. D*, 10:2445–2459, Oct 1974.
- [8] G. Baym. RHIC: From dreams to beams in two decades. *Nuclear Physics A*, 698(1-4):xxiii – xxxii, 2002.
- [9] Tapan Nayak. Search for the QCD critical point at RHIC: First experience with Au-Au collisions at 9.2 GeV. <http://www.bnl.gov/rhic/news/040808/story3.asp>. Accessed: 2013-11-19.
- [10] Edward V. Shuryak. Quantum chromodynamics and the theory of superdense matter. *Physics Reports*, 61(2):71 – 158, 1980.
- [11] Zoltan Fodor and Sandor D. Katz. Critical point of QCD at finite  $t$  and  $\mu$ , lattice results for physical quark masses. *Journal of High Energy Physics*, 2004(04):050, 2004.
- [12] S. K. Charagi and S. K. Gupta. Coulomb-modified Glauber model description of heavy-ion reaction cross sections. *Phys. Rev. C*, 41(4):1610–1618, Apr 1990.
- [13] H. Satz. *Phys. Reports*, 88:349, 1982.
- [14] K. Adcox et al. (PHENIX Collaboration). Formation of dense partonic matter in relativistic nucleus-nucleus collisions at RHIC: Experimental evaluation by the phenix collaboration. *Nuclear Physics A*, 757(1-2):184 – 283, 2005.
- [15] J. Adams et al. (STAR Collaboration). Experimental and theoretical challenges in the search for the quark gluon plasma: The STAR Collaboration’s critical assessment of the evidence from RHIC collisions. *Nucl. Phys. A*, 757:102, 2005.
- [16] B.B. Back et al. (PHOBOS Collaboration). The PHOBOS perspective on discoveries at RHIC. *Nuclear Physics A*, 757(12):28 – 101, 2005. [jce:title;First Three Years of Operation of RHIC;ce:title;.](#)

- [17] I. Arsene et al. (BRAHMS Collaboration). Quarkgluon plasma and color glass condensate at RHIC? the perspective from the BRAHMS experiment. *Nuclear Physics A*, 757(12):1 – 27, 2005. `arXiv:nucl-ex/0509013`.
- [18] Berndt Mller. Hadronic signals of deconfinement at RHIC. *Nuclear Physics A*, 750(1):84 – 97, 2005.
- [19] S. S. Adler et al. (PHENIX Collaboration). Elliptic flow of identified hadrons in  $au + au$  collisions at  $\sqrt{s_{NN}} = 200$  *gev*. *Phys. Rev. Lett.*, 91(18):182301, Oct 2003.
- [20] Miklos Gyulassy and Larry McLerran. New forms of QCD matter discovered at RHIC. *Nuclear Physics A*, 750(1):30 – 63, 2005.
- [21] Miklos Gyulassy and Michael Plmer. Jet quenching in dense matter. *Physics Letters B*, 243(4):432 – 438, 1990.
- [22] Wojciech Florkowski. *Phenomonology of Ultra-Relativistic Heavy-Ion Collisions*. World Scientific Publishing Company, 5 Toh Tuck Link, Singapore 596224, 2004.
- [23] S. S. Adler et al. (PHENIX Collaboration). Absence of suppression in particle production at large transverse momentum in  $\sqrt{s_{NN}} = 200$  GeV d + Au. *Phys. Rev. Lett.*, 91:072303, 2003.
- [24] Dmitri Kharzeev, Yuri V. Kovchegov, and Kirill Tuchin. Cronin effect and high- $p_T$  suppression in pa collisions. *Phys. Rev. D*, 68(9):094013, Nov 2003.
- [25] S. Chatrchyan et al. (CMS Collaboration). Multiplicity and transverse momentum dependence of two- and four-particle correlations in pPb and PbPb collisions. *Physics Letters B*, 724(45):213 – 240, 2013.
- [26] G. Aad et al. (ATLAS Collaboration). Observation of associated near-side and away-side long-range correlations in  $\sqrt{s_{NN}}=5.02$  TeV proton-lead collisions with the ATLAS detector. *Phys. Rev. Lett.*, 110:182302, May 2013.
- [27] B. Abelev et al. (ALICE Collaboration). Long-range angular correlations on the near and away side in pPb collisions at  $\sqrt{S_{NN}} = 5.02$  TeV. *Physics Letters B*, 719(13):29 – 41, 2013.
- [28] S. S. Adler et al. (PHENIX Collaboration). Detailed study of high- $p_T$  neutral pion suppression and azimuthal anisotropy in Au + Au collisions at  $\sqrt{s_{NN}} = 200$  GeV. *Phys. Rev. C*, 76(3):034904, Sep 2007.
- [29] S. S. Adler et al. (PHENIX Collaboration). Identified charged particle spectra and yields in Au + Au collisions at  $\sqrt{s_{NN}} = 200$  GeV. *Phys. Rev. C*, 69:034909, 2004.
- [30] S. Chatrchyan et al. (CMS Collaboration). Measurement of the elliptic anisotropy of charged particles produced in PbPb collisions at  $\sqrt{s_{NN}} = 2.76$  TeV. *Phys. Rev. C*, 87:014902, Jan 2013.
- [31] K. Aamodt et al. (ALICE Collaboration). Elliptic flow of charged particles in Pb-Pb collisions at  $\sqrt{s_{NN}} = 2.76$  TeV. *Phys. Rev. Lett.*, 105(25):252302, Dec 2010.
- [32] G. Aad and others (ATLAS Collaboration). Measurement of the pseudorapidity and transverse momentum dependence of the elliptic flow of charged particles in lead-lead collisions at  $\sqrt{s_{NN}} = 2.76$  TeV with the ATLAS detector. *Phys. Lett. B*, 707:330, 2012.

- [33] G. Aad et al. (ATLAS Collaboration). Observation of a centrality-dependent dijet asymmetry in lead-lead collisions at  $\sqrt{s_{NN}} = 2.76$  TeV with the ATLAS detector at the LHC. *Phys. Rev. Lett.*, 105:252303, Dec 2010.
- [34] S. Chatrchyan et al. (CMS Collaboration). Observation and studies of jet quenching in PbPb collisions at  $\sqrt{s_{NN}} = 2.76$  TeV. *Phys. Rev. C*, 84:024906, Aug 2011.
- [35] B. Hippolyte. Bulk matter physics and its future at the large hadron collider. *The European Physical Journal C*, 62(1):237–242, 2009.
- [36] A. M. Poskanzer and S. A. Voloshin. Methods for analyzing anisotropic flow in relativistic nuclear collisions. *Phys. Rev. C*, 58(3):1671–1678, Sep 1998.
- [37] Peter F. Kolb and Ulrich W. Heinz. *Quark Gluon Plasma*. Singapore: World Scientific, 2004.
- [38] J. Y. Ollitrault. Anisotropy as a signature of transverse collective flow. *Phys. Rev. D*, 46:229, 1992.
- [39] Lszl P. Csernai. *Introduction to Relativistic Heavy Ion Collisions*. Jonh Wiley and Sons Ltd., Chichester, England, 2008.
- [40] J. D. Bjorken. Highly relativistic nucleus-nucleus collisions: The central rapidity region. *Phys. Rev. D*, 27(1):140–151, Jan 1983.
- [41] P. Huovinen and P.V. Ruuskanen. Hydrodynamic models for heavy ion collisions. *Annual Review of Nuclear and Particle Science*, 56(1):163–206, 2006.
- [42] Jean-Yves Ollitrault. Relativistic hydrodynamics for heavy-ion collisions. *European Journal of Physics*, 29(2):275, 2008.
- [43] Peter F. Kolb and Ulrich W. Heinz. Hydrodynamic description of ultrarelativistic heavy-ion collisions. *eprint at arXiv:nucl-th/0305084v2 [nucl-th]*, 2003.
- [44] F. Karsch. The phase transition to the quark gluon plasma: Recent results from lattice calculations. *Nuclear Physics A*, 590(12):367 – 381, 1995.
- [45] Helmut Satz. The quark-gluon plasma a short introduction. *Nuclear Physics A*, 862863(0):4 – 12, 2011. `|ce:title|The Sixth International Conference on Physics and Astrophysics of Quark Gluon Plasma (ICPAQGP-2010)|/ce:title| |xocs:full-name|The Sixth International Conference on Physics and Astrophysics of Quark Gluon Plasma (ICPAQGP-2010)|/xocs:full-name|.`
- [46] Xin-Nian Wang. Why the observed jet quenching at RHIC is due to parton energy loss. *Physics Letters B*, 579(3-4):299 – 308, 2004.
- [47] Steffen A. Bass, Charles Gale, Abhijit Majumder, Chiho Nonaka, Guang-You Qin, Thorsten Renk, and Jörg Ruppert. Systematic comparison of jet energy-loss schemes in a realistic hydrodynamic medium. *Phys. Rev. C*, 79:024901, Feb 2009.
- [48] A. Adare et al. (PHENIX Collaboration). Azimuthal anisotropy of  $\pi^0$  production in Au + Au collisions at  $\sqrt{s_{NN}} = 200$  GeV: Path-length dependence of jet quenching and the role of initial geometry. *Phys. Rev. Lett.*, 105:142301, Sep 2010.

- [49] J. Adams et al. (STAR Collaboration). Particle-type dependence of azimuthal anisotropy and nuclear modification of particle production in Au + Au collisions at  $\sqrt{s_{NN}} = 200$  GeV. *Phys. Rev. Lett.*, 92:052302, Feb 2004.
- [50] Michael L. Miller, Klaus Reygers, Stephen J. Sanders, and Peter Steinberg. Glauber modeling in high-energy nuclear collisions. *Annual Review of Nuclear and Particle Science*, 57(1):205–243, 2007.
- [51] K. Adcox et al. (PHENIX Collaboration). Single identified hadron spectra from  $\sqrt{s_{NN}} = 130$  GeV Au + Au collisions. *Phys. Rev. C*, 69:024904, 2004.
- [52] S. S. Adler et al. (PHENIX Collaboration). Production of  $\phi$  mesons at midrapidity in  $\sqrt{s_{NN}} = 200$  GeV Au + Au collisions at relativistic energies. *Phys. Rev. C*, 72:014903, 2005.
- [53] S. Afanasiev et al. (PHENIX Collaboration). Elliptic flow for  $\phi$  mesons and (anti)deuterons in Au + Au collisions at  $\sqrt{s_{NN}} = 200$  GeV. *Phys. Rev. Lett.*, 99:052301, Jul 2007.
- [54] A. Adare et al. (PHENIX Collaboration). Scaling properties of azimuthal anisotropy in Au+Au and Cu + Cu collisions at  $\sqrt{s_{NN}} = 200$  GeV. *Phys. Rev. Lett.*, 98:162301, 2007.
- [55] S. S. Adler et al. (PHENIX Collaboration). Nuclear effects on hadron production in d+Au collisions at  $\sqrt{s_{NN}} = 200$  GeV revealed by comparison with  $p+p$  data. *Phys. Rev. C*, 74:024904, Aug 2006.
- [56] R. J. Fries, B. Müller, C. Nonaka, and S. A. Bass. Hadron production in heavy ion collisions: Fragmentation and recombination from a dense parton phase. *Phys. Rev. C*, 68:044902, Oct 2003.
- [57] Lie-Wen Chen and Che Ming Ko. Partonic effects on anisotropic flows at rhic. *Journal of Physics G: Nuclear and Particle Physics*, 31(4):S49, 2005.
- [58] V. Greco, C. M. Ko, and P. Lévai. Partonic coalescence in relativistic heavy ion collisions. *Phys. Rev. C*, 68:034904, Sep 2003.
- [59] Rudolph C. Hwa and C. B. Yang. Recombination of shower partons in fragmentation processes. *Phys. Rev. C*, 70:024904, Aug 2004.
- [60] R. J. Fries, B. Müller, C. Nonaka, and S. A. Bass. Hadronization in heavy-ion collisions: Recombination and fragmentation of partons. *Phys. Rev. Lett.*, 90(20):202303, May 2003.
- [61] Charles B. Chiu, Rudolph C. Hwa, and C. B. Yang. Azimuthal anisotropy: ridges, recombination and breaking of quark number scaling. *Phys. Rev. C*, 78:044903, 2008.
- [62] S. Chatrchyan et al. (CMS Collaboration). Measurement of the azimuthal anisotropy of neutral pions in Pb-Pb collisions at  $\sqrt{s_{NN}}=2.76$  TeV. *Phys. Rev. Lett.*, 110:042301, Jan 2013.
- [63] S. Chatrchyan et al. (CMS Collaboration). The CMS experiment at the CERN LHC. *JINST*, 03:S08004, 2008.
- [64] G L Bayatian et al. (CMS Collaboration). *CMS Physics Technical Design Report Volume I: Detector Performance and Software*, 2006.
- [65] L. Evans. *LHC Design Report - The LHC Machine - Introduction*, May 2004.

- [66] S. Chatrchyan et al. (CMS Collaboration). Dependence on pseudorapidity and on centrality of charged hadron production in PbPb collisions at  $\sqrt{s_{NN}} = 2.76$  TeV. *JHEP*, 08:141, 2011.
- [67] A. Adare et al. (PHENIX Collaboration). Measurement of neutral mesons in  $p + p$  collisions at  $\sqrt{s} = 200$  GeV and scaling properties of hadron production. *Phys. Rev. D*, 83:052004, Mar 2011.
- [68] I.P. Lokhtin, L.V. Malinina, S.V. Petrushanko, A.M. Snigirev, I. Arsene, et al. Recent developments on HYDJET/PYQUEN event generators and novel jet quenching observables at LHC. *PoS, HIGH-PTLHC08:002*, 2008.
- [69] Xin-Nian Wang and Miklos Gyulassy. hijing: A monte carlo model for multiple jet production in pp, pA, and AA collisions. *Phys. Rev. D*, 44:3501–3516, Dec 1991.
- [70] T. Sjöstrand and S. Mrenna and P. Skands. PYTHIA 6.4 physics and manual. *JHEP*, 05:026, 2006.
- [71] G. Aad et al. (ATLAS Collaboration). Long-range angular correlations of  $\pi$ , K and p in pPb collisions at  $\sqrt{s_{NN}} = 5.02$  TeV. *Physics Letters B*, 726(13):164 – 177, 2013.
- [72] Ulrich Heinz and Raimond Snellings. Collective flow and viscosity in relativistic heavy-ion collisions. *Annual Review of Nuclear and Particle Science*, 63(1):123–151, 2013.
- [73] Ranbir Singh, Lokesh Kumar, Pawan Kumar Netrakanti, and Bedangadas Mohanty. Selected Experimental Results from Heavy Ion Collisions at LHC. *eprint at arXiv:nucl-ex/1304.2969 [nucl-ex]*, 2013.
- [74] Anton Wiranata, Volker Koch, Madappa Prakash, and Xin Nian Wang. Shear viscosity of hadrons with K-matrix cross sections. *eprint at arXiv:hep-ph/1307.4681 [hep-ph]*, 2013.
- [75] Barbara Betz and Miklos Gyulassy. Azimuthal Jet Tomography of Quark Gluon Plasmas at RHIC and LHC. *eprint at arXiv:nucl-th/1305.6458 [nucl-th]*, 2013.
- [76] B. Abelev et al. (ALICE Collaboration). Centrality dependence of  $\pi$ ,  $k$ , and  $p$  production in pb-pb collisions at  $\sqrt{s_{NN}} = 2.76$  tev. *Phys. Rev. C*, 88:044910, Oct 2013.
- [77] B. Abelev et al. (ALICE Collaboration). Anisotropic flow of charged hadrons, pions and (anti-)protons measured at high transverse momentum in PbPb collisions at  $\sqrt{s_{NN}}$  TeV. *Physics Letters B*, 719(13):18 – 28, 2013.
- [78] W A Horowitz and M Gyulassy. Quenching and tomography from the rhic to the lhc. *Journal of Physics G: Nuclear and Particle Physics*, 38(12):124114, 2011.
- [79] B. Abelev et al. (ALICE Collaboration). Neutral pion and meson production in protonproton collisions at and  $\sqrt{s} = 0.9$  TeV and  $\sqrt{s} = 7$  TeV. *Physics Letters B*, 717(13):162 – 172, 2012.
- [80] G L Bayatyan et al. (CMS Collaboration). *CMS computing: Technical Design Report*, 2005.